In-vivo dynamic 3D phase-contrast microscopy : a novel tool to investigate the mechanisms of ventilator induced lung injury

Luca Fardin

To cite this version:

Luca Fardin. In-vivo dynamic 3D phase-contrast microscopy : a novel tool to investigate the mechanisms of ventilator induced lung injury. Pulmonology and respiratory tract. Université Grenoble Alpes, 2019. English. NNT : 2019GREAS037 . tel-02899311

HAL Id: tel-02899311
https://theses.hal.science/tel-02899311

Submitted on 15 Jul 2020

Communauté
UNIVERSITÉ Grenoble Alpes

THÈSE

Pour obtenir le grade de

DOCTEUR DE LA COMMUNAUTÉ UNIVERSITÉ GRENOBLE ALPES

Spécialité : **BIS – Biotechnologie, instrumentation, signal et imagerie pour la biologie, la médecine et l’environnement**

Arrêté ministériel : 25 mai 2016

Présentée par

Luca FARDIN

Thèse dirigée par **Sam BAYAT**, Professeur des Universités-Praticien Hospitalier, Communauté Université Grenoble Alpes et
codirigée par **Alberto BRAVIN**

préparée au sein du **Laboratoire European Synchrotron Radiation Facility**
dans **l'École Doctorale Ingénierie pour la Santé la Cognition et l’Environnement**

Microscopie 3D dynamique in-vivo en contraste de phase: un nouvel outil pour étudier les lésions pulmonaires induites par la ventilation mécanique

In-vivo dynamic 3D phase-contrast microscopy: a novel tool to investigate the mechanisms of ventilator induced lung injury

Thèse soutenue publiquement le **18 décembre 2019,**
devant le jury composé de :

Monsieur, Jean-Luc COLL
DIRECTEUR DE RECHERCHE, INSERM DELEGATION ALPES, Président
Monsieur, Claude GUERIN
PROFESSEUR DES UNIV - PRATICIEN HOSP., UNIVERSITE DE LYON, Rapporteur
Monsieur, Alessandro OLIVO
PROFESSEUR, UNIVERSITE COLLEGE DE LONDRES, Rapporteur
Madame, Anne, BONNIN
DOCTEUR EN SCIENCES, INSTITUT PAUL SCHERRER, Examinateur
Monsieur, Christian DULLIN
PROFESSEUR ASSOCIE, UNIVERSITE GEORG-AUGUST DE GOTTINGEN, Examinateur
Monsieur, Sam BAYAT
PROFESSEUR DES UNIV - PRATICIEN HOSP., CHU GRENOBLE ALPES, Directeur de thèse
Monsieur, Alberto BRAVIN
DOCTEUR EN SCIENCES, ESRF GRENOBLE, Co-directeur de thèse

To my Father

RESUME

La ventilation mécanique expose les poumons à des contraintes mécaniques pouvant causer ou aggraver des lésions chez les patients présentant une insuffisance respiratoire aiguë; ce phénomène est appelé *Ventilator Induced Lung Injury* (VILI). Les mécanismes exacts par lesquels le VILI est initié et entretenu au niveau acinaire restent inconnus : les hypothèses principales se basent sur une distension excessive des tissus (volotraumatisme) et une réouverture cyclique des régions collabées (atélectrauma). Le lien entre la contrainte mécanique sur le tissu alvéolaire, et la réponse inflammatoire à un stade précoce de la lésion, n'est toujours pas connu. Le manque de techniques fournissant des informations *in-vivo* à l'échelle alvéolaire sur la manière dont la ventilation mécanique déforme le parenchyme pulmonaire, constitue un verrou technologique pour la recherche. Les progrès récents de la microscopie 3D au rayons X en contraste de phase, obtenus dans des installations de rayonnement synchrotron, ont montré la possibilité d'imager des poumons *in-vivo* à l'échelle des voies respiratoires terminales et des alvéoles. Cependant, aucune des techniques disponibles ne permet de reconstruire complètement les déformations complexes du parenchyme pulmonaire induites par les contractions cardiaques et la ventilation mécanique. Pour surmonter cette limitation, un protocole d'acquisition d'imagerie tomodensitométrique, basé sur la synchronisation du ventilateur mécanique et de l'activité cardiaque, a été développé. Cela nous a permis de reconstruire le mouvement du parenchyme pulmonaire avec une taille de voxel de 20 µm ce qui s'est avéré suffisant pour visualiser les voies respiratoires terminales mais pas la structure alvéolaire. Ce protocole a été appliqué à un modèle de VILI chez le lapin. L'atélectrauma a ainsi été quantifié pendant le cycle respiratoire. Nous avons pu mettre en évidence une hétérogénéité des pressions d'ouverture et de fermeture des espaces aériens à la fois au sein d'un même poumon, et entre les animaux. L'analyse histologique mené en aveugle par un anatomopathologiste, a montré une corrélation spatiale entre l'atélectrauma et les lésions alvéolaires ($p = 0,007$). Par ailleurs, une corrélation spatiale entre atélectrauma et infiltration cellulaire a également été observée ($p = 0,04$). La technique d'acquisition d'images a été améliorée afin d'obtenir une taille de voxel de 6 µm, ce qui a permis de visualiser les structures alvéolaires. Bien que cette résolution spatiale soit encore limitée pour l'étude des parois alvéolaires minces (10 µm), il s'agit, à notre connaissance, de la résolution spatiale la plus élevée obtenue à ce jour en microscopie 3D dynamique *in-vivo*. Cette technique permettra d'étudier la déformation du

parenchyme pulmonaire et constitue une étape importante vers l’étude *in-vivo* du VILI à l’échelle alvéolaire.

ABSTRACT

Mechanical ventilation exposes the lung to mechanical stresses that can exacerbate or induce injury in patients with respiratory failure, a condition known as Ventilator-Induced Lung Injury (VILI). The exact mechanisms through which VILI is initiated and entertained at the acinar level remain elusive: the main hypotheses include excessive stretch of the tissues (volutrauma) and cyclic re-opening of closed regions (atelectrauma). The link between the mechanical stress induced on the alveolar tissue and the inflammatory response at an early stage of the injury is still not understood. Currently, the lack of techniques providing information *in-vivo* and at the alveolar scale on how the mechanical ventilation deforms the lung parenchyma, represents an obstacle for research in the field. Recent advances in phase-contrast 3D microscopy, obtained in synchrotron radiation facilities, have shown the possibility to image the lungs *in-vivo*, resolving terminal airways and alveoli. However, none of the available techniques allow to fully reconstruct the complex deformations of the lung parenchyma induced simultaneously by cardiac contractions and mechanical ventilation. To overcome this limitation, a computed tomography imaging acquisition protocol, based on the synchronization between the mechanical ventilation and the cardiac activity, was developed. This technique allowed to resolve and reconstruct the lung parenchymal motion with an effective voxel size of 20 µm, sufficient to visualize terminal airways but not the alveolar structure. The technique was applied to a rabbit model of VILI, in which atelectrauma was quantified within a tidal breath. The data revealed a significant heterogeneity in the opening and closing pressures of the airspaces both within and in between animals. Subsequent histological analysis showed a spatial correlation between atelectrauma and alveolar damage, assessed through qualitative evaluation performed by a pathologist blinded to the presence of atelectrauma (p=0.007). Also, spatial correlation between atelectrauma and cellular infiltration evidenced (p=0.04). This imaging technique was further refined to obtain an effective voxel size of 6 µm, which allowed to visualize the alveolar structure. While this spatial resolution is still limited for studying the thin alveolar walls (~10 µm), to the best of our knowledge it is the highest spatial resolution obtained so far in *in-vivo* dynamic 3D microscopy. This technique will allow to study the lung parenchyma deformation and represents an important step towards the *in-vivo* study of VILI at the alveolar scale.

ACKNOWLEDGMENTS

I would like to express my gratitude to my supervisors Prof. Sam Bayat and Dr. Alberto Bravin for the support and encouragement they gave me during the three years of this project. Without their guidance this PhD wouldn’t have been achievable.

I would like to acknowledge the funding institutions, in particular the European Synchrotron Radiation Facility, the Swedish Research Council and the Swedish heart and lung foundation.

My special thanks go to Prof. Anders Larsson and to the Uppsala University for their financial support. Professor Larsson’s experience and enthusiasm was the heart of the Lung Imaging collaboration in which this Thesis was carried out. I would like to thank the Hedenstierna Laboratory, in particular Prof. Goran Hedenstierna, Prof. Gaetano Perchiazzi, Dr. Jose-Luis Cercos-Pita for the useful discussions during our collaboration meetings. I am also grateful to Ms Katja Andersson whose technical assistance made these meetings possible.

I would like to offer my special thanks to Dr. Ludovic Broche, whose valuable work set the basis for this PhD project and who supervised me during the first year of the Thesis.

I would like to express my very great appreciation to all the colleagues at the European Synchrotron Radiation Facility, in particular at the ID17 beamline. I am particularly grateful to Dr. Alberto Mittone for his encouragement and support in every aspect of this work, from data acquisition to data reconstruction. I would like to thank also the ID17 beamline staff for their support during the experiments: the beamline responsible Dr. Michael Krisch, Dr. Herwig Requardt, Benjamin Restaut and Alexandra Demory. I am also grateful to Anthony Mauro, Roberto Arturo Homs Regojo and to the staff of the biomedical facility Loic De Saint Jean and Charlene Caloud. A special thought goes finally to the memory of Dr. Elke Brauer-Krisch.

I wish to acknowledge the help and support provided by the Strobe INSERM Laboratory in particular by Dr. Emmanuel Brun whose knowledge in imaging and image analysis was a precious

input during the Thesis. My thanks are extended to the staff of the Grenoble University Hospital: assistance provided by Olivier Stephanov was greatly appreciated.

This work was performed in the framework of a wide collaboration. I would like to thank the staff of the Tomcat beamline, in particular Dr. Goran Lovric, Dr. Christian Schlepuetz, and Dr. Elena Borisova for sharing their knowledge in dynamic lung imaging and the scientists from the Lund University Prof. Rajmund Mokso and Prof. Lars Olsson.

I would also like to thank my mother and my sister: I would have never started nor completed a PhD program without their constant support and their sacrifices.

A special thanks goes finally to all my friends in Grenoble and in Italy who were at my side during the last three challenging years.

TABLE OF CONTENTS

LIST OF AND ABBREVIATIONS AND SYMBOLS

Abbreviation	**Meaning**	**Introduced in**
ARDS	Acute Respiratory Distress Syndrome	Section 1.2.1
BFGS	Broyden-Fletcher-Goldfarb-Shanno	Section 2.5.1
CG	Conjugate Gradient	Section 2.5.1
CGLS	Conjugate Gradient Line Search	Section 4.3.2.1
CT	Computed Tomography	Section 2.2
ECG	Electrocardiogram	Section 2.3.1
EH1,2	Experimental Hutch 1 or 2	Section 3.2.1
ESRF	European Synchrotron Radiation Facility	Section 3
FBP	Filtered Back Projection	Section 2.2.2
FFD	Free-Form Deformation	Section 2.5.1
FRC	Functional Residual Capacity	Section 1.1.2
FTIR	Fourier Transform Infrared Spectroscopy	Section 4.6.7
GD	Gradient Descent	Section 2.5.1
ICU	Intensive Care Unit	Section 1.2.1
IL-6	Interleukin-6	Section 1.2.2
IL-8	Interleukin-8	Section 1.2.2
L-BFGS	Low Memory Broyden-Fletcher-Goldfarb-Shanno	Section 2.5.1
LINAC	Linear Accelerator	Section 3.1
LS	Line Search	Section 2.5.1
MRI	Magnetic Resonance Imaging	Section 2.1
MRT	Microbeam Radiation Therapy	Section 3.2
OH1,2	Optics Hutch	Section 3.2.1
PBI	Propagation Based Phase Contrast Imaging	Section 2.2.3
PEEP	Positive End Expiratory Pressure	Section 1.2.2
PET	Positron Emission Tomography	Section 2.1
PNT	Pneumotachometer	Section 3.3.4

QN	Quasi Newton	Section 2.5.1
RAGE	Receptor for Advanced Glycation End products	Section 1.2.2
RF	Radiofrequency (cavity)	Section 3.1
sCMOS	scientific Complementary Metal–Oxide–Semiconductor	Section 3.2.2
SLS	Swiss Light Source	Section 2.4.2
TIE	Transport of Intensity Equation	Section 2.2.3
VILI	Ventilator-Induced Lung Injury	Section 1.2.2
V_T	Tidal Volume	Section 1.1.2

Symbol	**Quantity**	**Introduced in**
$\boldsymbol{\nabla}$	Nabla Operator	Section 2.5.1
∇^2	Laplacian Operator	Section 2.2.1
$\mu(x,y,z)$	Linear Attenuation Coefficient	Section 2.2.1
a_f	Aerated fraction	Section 4.3.3.2
B	Magnetic field	Section 3.1
c	Speed of light in vacuum	Section 3.1
d	Sample to Detector Distance	Section 2.2.3
E	Energy of a Monochromatic Plane Wave	Section 2.2.3
E_c	Cost Function (Image Registration)	Section 2.5.1
E_e	Electron energy	Section 3.1
E_{rs}	Elastance Respiratory System	Section 1.1.2
f	Spatial Frequency (Phase Contrast)	Section 2.2.3
$F(u,v)$	Fourier Transform Linear Attenuation Coefficient	Section 2.2.2
F_{IO2}	Fraction of Inspired Oxygen	Section 1.1.3
$F_{R,D}$	Recruitment/derecruitment fraction	Section 4.3.3.2
$\mathbf{g}(\mathbf{x})$	Transformation (Image Registration)	Section 2.5.1
$\mathcal{H}$	Hessian	Section 2.5.1

$I(x,y,z)$	Plane Wave Intensity	Section 2.2.1
I_e	Electron Current Storage Ring	Section 3.1
$I_{m,r}$	Moving/Reference Volume (Image Registration)	Section 2.5.1
J	Jacobian Matrix	Section 2.5.3
k_θ,k	Wave Vector (Plane Wave)	Section 2.2.1, 2.2.2
L	Source to Sample Distance (Phase Contrast)	Section 2.2.3
L_a	Arc length in magnetic dipole	Section 3.1
$\mathcal{M}$	Similarity Metrics (Image Registration)	Section 2.5.1
$n(x,y,z)$	Refractive Index	Section 2.2.1
$p(x,y),p_\theta(t)$	Parallel Projection (Tomography)	Section 2.2.2
Pa_{CO2}	Partial Pressure of CO_2 in arterial blood	Section 4.2.4
P_{alv}	Alveolar Pressure	Section 1.1.2
Pa_{O2}	Arterial Partial Pressure of Oxygen	Section 1.1.3
P_{atm}	Atmospheric Pressure	Section 1.1.2
P_{CO2}	Partial Pressure of Carbon Dioxide	Section 1.1.3
P_{mus}	Pressure Applied by Chest Muscles	Section 1.1.2
P_{O2}	Partial Pressure of Oxygen	Section 1.1.3
P_{pl}	Pleural Pressure	Section 1.1.2
P_{res}	Resistive Pressure	Section 1.1.2
P_{rs}	Elastic Recoil of Lung and Chest (Pressure)	Section 1.1.2
P_{tp}	Transpulmonary Pressure	Section 1.1.2
P_{TRACH}	Tracheal Pressure	Section 3.3.4
P_{vent}	Pressure Applied by Mechanical Ventilator	Section 1.1.2
$\dot{Q}$	Lung Perfusion	Section 1.1.3
$\mathcal{R}$	Regularization Term (Image Registration)	Section 2.5.1
R_{aw}	Airway Resistance	Section 1.1.2
s	Size of X-ray source	Section 2.2.3
$S_\theta(w)$	Fourier Transform Parallel Projection	Section 2.2.2
$\dot{V}$	Gas Flow / Ventilation	Section 1.1.2, 1.1.3

$\dot{V}/\dot{Q}$	Ventilation Perfusion Ratio	Section 1.1.3
$\beta(x,y,z)$	Absorption Index	Section 2.2.1
$\beta_{i,n}$	B-Spline of order n applied to node i	Section 2.5.2
β_r	Particle speed/speed of light in vacuum	Section 3.1
γ	Lorentz factor	Section 3.1
$\delta(x,y,z)$	Refractive Index Decrement	Section 2.2.1
δ_D	Dirac Delta	Section 2.2.2
$\delta x,y,z$	Mesh Spacing B-Spline	Section 2.5.2
$\Delta\phi$	Phase Shift (Plane Wave)	Section 2.2.1
ε	Cost Function Regularization Weight	Section 2.5.1
λ	Wavelength (electromagnetic radiation)	Section 2.2.3
ρ_e	Electron Density	Section 2.2.3
$\Psi(x,y,z)$	Plane Wave perturbed by Scatterers	Section 2.2.1

INTRODUCTION

Acute Respiratory Distress Syndrome (ARDS) [1] is a clinical disorder characterized by severe lung inflammation, hypoxemia, diffuse alveolar damage and infiltration [2]. It represents about 10% [3] of the cases in intensive care units (ICU), with a mortality rate between 35% and 45% [4].

Mechanical ventilation is invariably required in patients affected by ARDS. Despite its vital role in improving oxygenation, mechanical ventilation can damage the lung by exacerbating the preexisting lung injury, a condition known as Ventilator-Induced Lung Injury (VILI) [5]. The inflammation triggered in the lungs by the mechanical ventilation spreads to different organs, eventually leading to multi-organ failure and death.

The preclinical and clinical research in this field aims at identifying an appropriate ventilation strategy, which could provide life support in ARDS patients while minimizing the progression of the injury, with the objective of decreasing mortality. A deep understanding of the mechanisms leading to VILI is therefore of fundamental importance.

It is generally agreed that mechanical ventilation is detrimental in both healthy and injured lungs, due to the mechanical stresses and strains applied to the tissues [6]. The sources of strain are multiple. Overdistension, occurring when the lung is ventilated with high regional tidal volumes, induces mechanical injury through exaggerated lung tissue stretch. The injurious effects of mechanical ventilation at high tidal volumes were demonstrated by a decrease in the mortality of ARDS patients when protocols foreseeing lower tidal volumes were applied [7].

Ventilation at low tidal volumes exposes in turn the lungs to terminal airways and alveolar collapse. Cyclic collapse and reopening of lung units at every tidal breath, called *atelectrauma*, is associated to high stresses normal to the epithelial surface of the airways as they reopen or as the high-surface-tension liquid filling them is displaced. It causes epithelial cell damage and necrosis [8], [9].

Although the role of excessive stress and strain to the lung tissue by positive-pressure ventilation is well established, it is still not understood how VILI is initiated and entertained at the alveolar level. Specifically, the mechanistic link between the mechanical stresses induced to the lung tissue through atelectrauma and the early stage inflammatory response is not understood. **An introduction to lung physiology, to the injury that mechanical ventilation can induce in healthy and ARDS patients, as well as the open questions regarding the pathogenesis of VILI will be the subject of Chapter 1.**

One of the main experimental limitations in the study of these open questions on VILI is the absence of an *in-vivo* technique allowing for a direct observation of the dynamics of the lung parenchyma at the level of terminal airways and alveoli during mechanical ventilation. The main results, showing that this technological limitation may be soon overcome, were achieved so far in the field synchrotron radiation dynamic phase-contrast 3D microscopy [10], [11]. The experimental challenge in developing an *in-vivo* lung imaging technique is represented by the complex motion of the lung parenchyma, which must be synchronized with the acquisition and which is induced by the heart activity and by the ventilation, two sources of motion which influence each other [12] and are, however, asynchronous.

The first result was obtained by Dubsky et al., who developed an acquisition protocol capable of studying local tissue expansion during mechanical ventilation in an small animal model with an effective pixel size (20 µm) sufficient to visualize terminal airways but not alveoli [10]: the acquisition was not synchronized with the heartbeat causing motion artefacts, and a degradation in spatial resolution, around the heart. Lovric et al. on the other hand developed a technique with sufficient spatial resolution (3 µm pixel size) to observe alveoli and alveolar walls in a mouse model [13], using a constant airway pressure, preserving the information on the structure of the lung parenchyma, but loosing of information on its dynamics.

The only application of synchrotron radiation phase-contrast 3D microscopy to an animal model of VILI was described by Broche et al. [14]. This work, which represented the state of the art in my laboratory at the beginning of this Thesis, allowed to establish the mechanical interdependence between lung units which make atelectrauma a highly dynamic and time-dependent phenomenon.

The lung was imaged at constant airway pressure with a pixel size of 40 µm: this technique had therefore enough spatial resolution to study terminal airways, but only in static lung conditions.

In-vivo microscopy techniques, existing at the beginning of this Thesis, were characterized therefore by sufficient spatial resolution to image the lung parenchyma at the level of terminal airways and alveoli; however:

- if the resolution was sufficient to visualize the individual alveoli, the lung motion couldn't be studied;
- the lung parenchymal motion couldn't be fully resolved when both the heartbeat and the mechanical ventilation originated the parenchymal deformation;
- the lung parenchymal motion was never studied in a VILI model.

An introduction to dynamic phase-contrast 3D microscopy, a review on its state of the art and the limitations in the field at the beginning of this Thesis work will be the topic of Chapter 2.

The aim of this Thesis was therefore to develop an *in-vivo* acquisition protocol for dynamic 3D microscopy capable of resolving the motion of the lung parenchyma induced by the combined action of the heart motion and mechanical ventilation, in a VILI animal model, with a spatial resolution sufficient to visualize terminal airways and if possible alveoli.

This goal was achieved by using a detector pixel size of 20 µm, sufficient to visualize terminal airways but not alveoli. Applied to a VILI model, the acquisition protocol developed allowed to visualize and quantify atelectrauma in an initial stage of the injury and to study its regional relationship with lung inflammation. To my best knowledge this is the first time that VILI is studied in dynamic conditions at such a high spatial resolution in an animal model. **Synchrotron radiation facilities, where these techniques were developed, and the specific case of the biomedical beamline at the European Synchrotron Radiation Facility (ESRF, Grenoble, France), where this Thesis was carried out, will be described in Chapter 3. The acquisition protocol, the strategy developed for data analysis and the results of this study will be presented in Chapter 4**.

The acquisition protocol developed was further optimized at the end of this Thesis work, by decreasing the effective pixel size from 20 µm to 6 µm. This resolution allowed to visualize *in-vivo* the motion of the lung parenchyma at the alveolar scale, possibly opening the way to an investigation of an early stage animal model of VILI at this resolution. **The optimization of the acquisition protocol toward an effective pixel size of 6 µm and its limits will be the topic of Chapter 5.**

1 VENTILATOR-INDUCED LUNG INJURY

In this Chapter, the rationale for this Thesis work will be presented. The first section contains a short introduction on lung physiology, with a concise description of the lung structure and of gas exchange processes. These concepts will be useful to present the problematics of mechanical ventilation in both healthy and injured lungs, focusing especially on Acute Respiratory Distress Syndrome (ARDS). Mechanical ventilation in injured lungs will lead to the concept of Ventilator-induced Lung Injury (VILI), one of the main obstacles to a decrease in mortality in ARDS patients. The open questions on VILI, concerning how it is initiated and sustained, will then justify the need for *in-vivo* high-resolution imaging techniques and will lead to the next chapter, where the choice of synchrotron radiation dynamic computed tomography as the main investigative tool will be discussed.

1.1 LUNG PHYSIOLOGY

The lung is the organ where the gas exchange occurs. Oxygen is transferred from the air into the blood and the carbon dioxide produced by the cellular metabolism is removed from the organism. In this section, the structure of the lung will be shortly reviewed; it will be followed by the description of ventilation, which is the mechanism through which the air is inspired, and of the gas exchange.

1.1.1 Lung structure

The lungs are the main organs of the respiratory system. They are enclosed in the thoracic cavity in a region delimited by the diaphragm, the mediastinum and the rib cage. There are two lungs, left and right: the left lung is smaller, due to the presence of the heart. The two lungs are divided by the mediastinum, which contains the heart and major vessels, the trachea, the esophagus and the thymus gland. The human lungs are divided into five *lobes*, three for the right lung and two for the left lung, and are surrounded by the two pulmonary pleurae: the internal visceral pleura, in contact with the lung and the external parietal pleura, connected to the thoracic cavity, the diaphragm, and the mediastinal surface. In between the two pleurae there is the pleural fluid, which assures adhesion between lung, thoracic cage and diaphragm. The pleural fluid also reduces friction during inflation and deflation: the lobes can slide on each other and on the thoracic cavity.

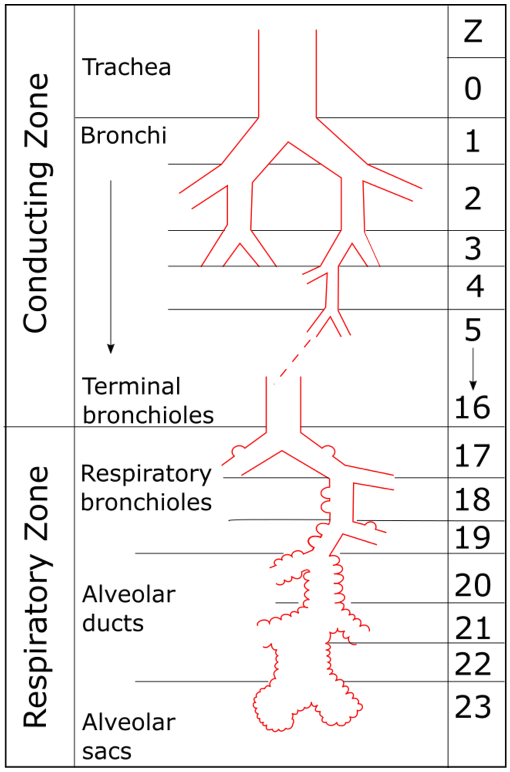

Figure 1-1 Model of the bronchial tree from the trachea to the alveolar sacs. On average 23 generations (Z) are present, corresponding to consecutive airway bifurcations. They are divided into a conducting zone, where no gas exchange occurs and a respiratory zone, where the airways are lined with alveoli. The region subtended by a terminal bronchiole is called acinus. (Modified from [15]*).*

The lungs are ventilated through the lower respiratory tract, which originates at the trachea. The trachea, in humans, is a tube with a diameter of approximately 15 mm, sustained by C-shaped cartilaginous rings. The two free extremities of these rings are connected by the trachealis muscles, which can induce a contraction of the trachea, regulating the airflow. The trachea divides into the two main bronchi, which enter respectively the left and right lung. Each main bronchus further divides into the lobar bronchi: in humans they are three for the main right bronchus, which create the three lobes of the right lung, and two for the main left bronchus, from which the two lobes of the left lung originate. The lobar bronchi divide into the segmental and sub-segmental bronchi. At each bifurcation of the bronchi corresponds an *airway generation* as shown in Figure 1-1. There are on average 23 generations in a human lung: the structure and diameter of the airways varies going down in the generations, following a fractal model [16], [17]. The first 16 generations do not take part in the gas exchange and are therefore called *conducting airways*; they constitute the *anatomic dead space*. From the seventh generation on, bronchi divide into airways called *bronchioles*. The change in generations reflects a change in structure: the cartilaginous rings found in bronchi, which provide support to the airway, become progressively irregular plates, conferring higher flexibility during inflation and deflation [18]. At the level of the bronchioles, cartilaginous structures disappear, and the airways remain surrounded by smooth muscles, which allow for a constriction or dilatation, to regulate the airflow. The last generation of bronchioles of the conducting airways is called *terminal bronchioles*. The terminal bronchioles divide into *respiratory bronchioles*, which contain the first *alveoli*, the region where the gas exchange occurs. Respiratory bronchioles further branch in several generations of alveolar ducts, completely lined by alveoli, which subtend the most distal part of the *airway-tree*: the *alveolar sacs*. The region subtended by a terminal bronchus is referred to as *acinus* [19]; the acini make up the *respiratory zone*.

The alveoli are the smallest unit of the lungs where the gas exchange occurs. They are lined with capillaries, with a diameter of approximately 7 to 10 µm [20], large enough for the passage of one red blood cell at the time. The interface between air and blood, called *blood-gas barrier*, is only 0.5 µm thick and it consists of the alveolar epithelial cells, the capillary endothelial cells, and an extracellular matrix containing collagen and elastin fibers, giving support and elasticity to the structure. There are two main types of epithelial cells, i.e. type I and type II. The cells type I are the most abundant ones and create the blood gas barrier; cells type II are more compact and are involved in the production of the surfactant, necessary for the stability of the lung. Alveoli have in fact, in first approximation, the shape of a hollow sphere with a diameter of 200 µm in humans [21]. Their inner surface is lined with fluid, which would make them collapse due to the high surface tension. The surfactant produced by the type II cells reduces the surface tension, preventing the structure to collapse and reducing the work needed for the inflation.

The alveoli in a human lung are approximately 500 million [21]; estimates of the internal aerated surface vary in the literature between 25 and 150 m^2 [22], [23], with a dependence on the lung volume. The surface area of the aerated region, the approximate spherical shape of the alveoli, which allows to maximize the ratio between the surface and the volume, and the thin alveolar walls constitute an optimized architecture to favor gas diffusion across the blood-gas barrier. The fractal structure of the airways assures a mostly homogeneous and efficient ventilation at minimized energetic cost [24].

The lung structure described in this section refers to humans. However, in the course of the Thesis work, rat and rabbit animal models were used. Even if the main notions can be applied, it is useful to stress that there are differences between animal models. Among the main differences between primates and rodents we can find, for example, the branching structure, dichotomous for the firsts and monopodial for the latter, but also the number of lobes and the cellular composition of the tracheobronchial tree [25]. Due to this (and other morphological differences) the results obtained in this work cannot be directly extrapolated to humans; they can nevertheless provide useful information on lung mechanics and function, as shown by the numerous insights provided by rat and rabbit animal models in the study of ventilator-induced lung injury [26].

1.1.2 Ventilation

In normal conditions breathing involves the diaphragm and the intercostal muscles. Inspiration is an active process, during which the diaphragm, a dome-shaped muscle at the basis of the thoracic cavity, contracts moving downward; this movement is transferred to the lungs through the pulmonary pleurae, causing their dilatation. At the same time, the external intercostal muscles contract, moving the ribs upward and forward, thus increasing the volume of the thoracic cavity. This dilatation creates a gradient in pressure along the airways, drawing air into the lungs. The expiration is instead mainly a passive process caused by the elastic recoil of the thoracic cavity and of the lung tissue itself, which compresses and expels the air.

During normal respiration approximately 500 ml of air is inspired and expired by humans [20]. This volume is called *tidal volume* (V_T) as visible in Figure 1-2. The volume of air remaining in the lung at the end of normal expiration is called *functional residual capacity* (FRC). Other volumes important for clinical applications and during mechanical ventilation are: the vital capacity, defined as the volume exhaled following maximal inspiration and maximal expiration and the residual volume, defined as the volume of air remaining in the lung after maximal expiration.

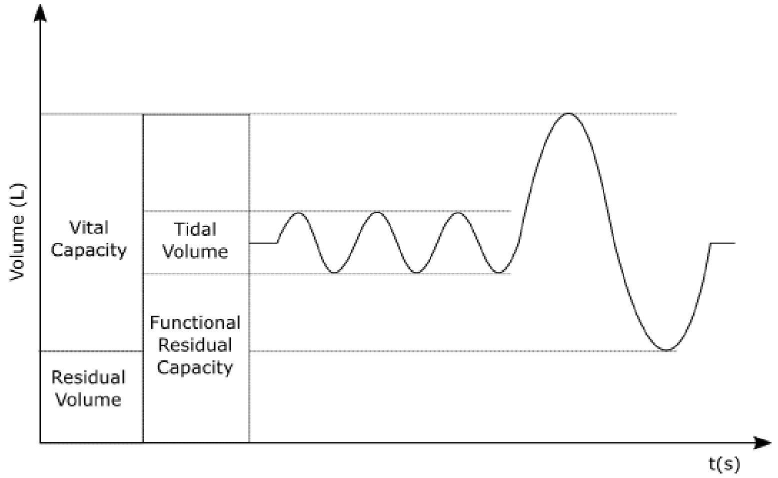

Figure 1-2 Scheme representing the lung volumes of interest. The graph represents the volume of air in the lungs during normal inspiration and expiration and following maximal inspiration and expiration.

To better understand the mechanics of ventilation, the pressure-volume relation has to be established. At the end of expiration, with the glottis open, the pressure inside the alveoli (*alveolar pressure*, P_{alv}) is equal to the atmospheric pressure (P_{atm}), since no flow of air is present. The pressure surrounding the lung is the pressure inside the pleural space, called *pleural pressure* (P_{pl}). Their difference, called *transpulmonary pressure* (P_{tp}) [27], is the one responsible for the lung inflation and the airflow into the airways. The presence of a positive FRC results from a subatmospheric P_{pl} at the end of expiration, which keeps the lung partially inflated, thanks to a positive transpulmonary pressure. A subatmospheric P_{pl}, or negative if P_{atm} is considered equal to zero, is due to the elastic recoil of the chest wall, which tends to expand, balanced by the elastic recoil of the lungs, which tend to contract. At the beginning of normal inspiration, the action of the diaphragm and of the intercostal muscles will cause a drop in P_{pl} and therefore an increase in P_{tp}, driving lung inflation. It is possible to underline now one of the principal differences between spontaneous breathing and mechanical ventilation: during mechanical ventilation, the increase in the transpulmonary pressure is not induced by a decrease in the pleural pressure, but by an increase in that of the airway, and therefore in the alveolar pressure. A second difference concerns the hemodynamics, which is influenced by the alveolar pressure: the same transpulmonary pressure can be obtained in fact with an alveolar infra-atmospheric pressure, in the case of spontaneous ventilation and with an alveolar supra-atmospheric pressure when positive pressure mechanical ventilation is applied.

The equation of motion during mechanical ventilation can be described following a simplified version of the model proposed by Rohrer [28]–[30]:

$$P_{vent} + P_{mus} = P_{rs} + P_{res} \tag{1-1}$$

Where P_{vent} is the pressure imposed by the mechanical ventilator, P_{mus} the pressure possibly applied by the muscles of the chest, P_{rs} the elastic recoil of lungs and chest wall and P_{res} the -*resistive pressure* dissipated within the airways due to gas flow ($\dot{V}$). P_{rs} and P_{res} apply above the end expiratory alveolar pressure. This means that the sum of the external applied forces will have to win the resistance to chest-lung inflation and to airflow through the airways. P_{rs} and P_{res} can be rewritten as:

$$P_{res} = R_{aw}\dot{V} = K_1 \cdot \dot{V} + K_2 \cdot \dot{V}^2 \tag{1-2}$$

and

$$P_{rs} = E_{rs} \cdot \Delta V \tag{1-3}$$

Equation 1-2 states that the respiratory resistance (R_{aw}) depends on a constant (K_1) and a flow-dependent term ($K_2 \cdot \dot{V}$); different formulations, based for example on the Blasius equation, can be found in literature [31]. In Equation 1-3 instead, E_{rs} is the *elastance* of the respiratory system and ΔV the variation in volume from resting conditions, usually FRC. Its reciprocal is called *compliance* and measures the variation of volume for a given variation in pressure. Compliance can be *static* or *dynamic*, depending on whether it is measured in absence or presence of airflow. Its value contains information on the elastic properties of both the lungs and the chest wall. In fact, the elastance of the respiratory system E_{rs} is the sum of the elastances of the lung and of the chest wall. If we plot the volume of the lung as a function of pressure, we obtain the pressure-volume (PV) curve of the respiratory system as depicted in Figure 1-3. The compliance will be defined as the slope of the curve. It is a function of the lung volume: notice that the PV curve is characterized by a hysteresis cycle, therefore, at a given pressure, the lung volume and compliance will differ during deflation than during inflation. Usually the human lung has a high compliance, with reduced work needed for inflation, but its value can vary in injured conditions, with the collapse of lung units, by inactivation of the surfactant, following alveolar infiltration, or by the modification of the structure and organization of collagen and elastin fibers, as in the case of fibrosis [32].

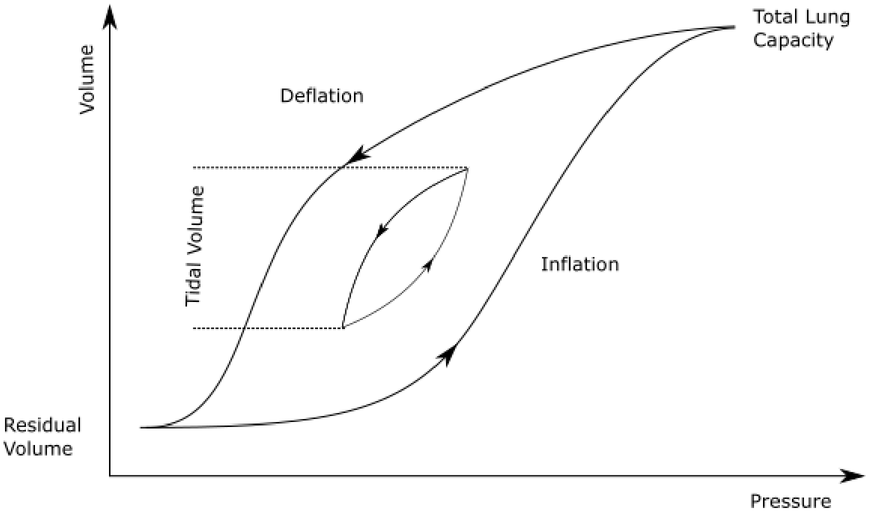

Figure 1-3 Pressure volume curve during normal and forced respiration. The lung compliance is defined as the slope of the curve. Note that the curve presents hysteresis, therefore the compliance and lung volume are different during inspiration and expiration at a given pressure.

1.1.3 Gas exchange

The variation in volume and pressure in the lungs during mechanical or spontaneous ventilation, establishes a pressure gradient in the airways and therefore an air flow. The volume of air inspired/expired per unit time is defined as ventilation ($\dot{V}$). Ventilation can be expressed as the product between V_T and the breathing frequency. The airways are divided into a conducting zone and a gas exchange zone: the tidal volume and the ventilation can be accordingly divided into dead space and dead space ventilation, for the conducting zone, and into alveolar space and alveolar ventilation, for the exchange zone. The alveolar ventilation provides the oxygen consumed by the metabolic activity and removes the CO_2 consequently produced, affecting the partial pressure of oxygen and carbon dioxide inside the alveoli.

The gas transport is dominated by convection in the upper airways, but due to the rapid increase in their cross-sectional surface area, the dominating process at the alveolar level is diffusion. Diffusion across the blood-air barrier is described by Fick's law [33]; applied to the lungs, it states that the transfer of a gas through the blood gas-barrier is proportional to the surface of the barrier, inversely proportional to its thickness and proportional to the difference in the partial pressures of the gas at the two sides of the barrier (acinus and capillary). The geometry of the blood-gas barrier previously discussed, concerning surface and thickness, allows for an efficient diffusion of oxygen and carbon dioxide: the partial pressure of the gases (P_{CO_2} and P_{O_2}) in the alveoli and in the blood can in fact be considered in equilibrium when the red blood cells are only at one third of their way along the capillaries surrounding the aerated region [20]. In injured conditions however, a thickening of the alveolar walls or a reduction in the ventilated surface area can impair diffusion, reducing the concentration of oxygen in the blood (*hypoxemia*) and increasing the concentration of carbon dioxide (*hypercapnia*).

A second factor affecting the gas exchange is the match between ventilation and perfusion ($\dot{Q}$), the latter defined as the blood flow inside the capillaries lining the alveoli. This match is quantified through the ventilation perfusion ($\dot{V}/\dot{Q}$) ratio. A reduced ventilation, associated to a normal blood flow (low $\dot{V}/\dot{Q}$), will for example produce a decrease in alveolar P_{O_2} (PA_{O_2}) and an increase in alveolar P_{CO_2}. Unlike P_{CO_2}, the value of alveolar P_{O_2} can be controlled during mechanical ventilation by acting not only on the ventilation but also on the fraction of inspired oxygen (F_{IO_2}), which measures the fraction of oxygen in the gas mixture inhaled by the patient. Hypoxia can be therefore reduced increasing ventilation or F_{IO_2}. One exception occurs when blood flows through collapsed lung units ($\dot{V}/\dot{Q} = 0$), a phenomenon known as *shunt*. These units are by definition non-aerated and are therefore not affected by variations in ventilation or oxygen fraction. This poorly oxygenated blood will mix with the one coming from normally oxygenated lung units, decreasing the global blood oxygen concentration.

1.2 ACUTE RESPIRATORY DISTRESS SYNDROME AND VENTILATOR-INDUCED LUNG INJURY

In the previous section lung morphology and ventilation were described in healthy subjects, with a focus on some mechanisms which could occur in injured conditions. In this section, the case of acute respiratory distress syndrome will be further analyzed, to introduce the ventilator-induced lung injury, the main subject of the Thesis.

1.2.1 Acute respiratory distress syndrome (ARDS)

Acute Respiratory Distress Syndrome (ARDS) is a clinical disorder, first described in 1967 [1]. It represents about 10% [3] of the cases in intensive care units (ICU), with a reported incidence varying from 1.5 to 79 cases per 100,000 population [34], [35]. The overall mortality rate is between 35% and 45% [4]. ARDS is characterized mainly by acute onset, hypoxemia and pulmonary infiltrates [36]. Although a recent definition of ARDS has been proposed, named the Berlin definition [2], a debate is still ongoing, due to the variability among patients, among health services in different countries and to the lack of a reliable diagnostic test [37]. In what follows we will define ARDS following four criteria, in agreement with Ranieri et al. [2]:

- Onset within one week of a known clinical insult
- Presence of chest opacities in Computed Tomography
- Edema not fully explained by cardiac failure or fluid overload (hypervolemia)

- Severe hypoxemia, measured from the ratio between Pa_{O_2} and F_{IO_2} at end expiratory pressure of at least 5 $\mathrm{cmH_2O}$

A value of $Pa_{O_2}/F_{IO_2} < 300(\text{mmHg})$ is defined as *mild* ARDS, a value of $Pa_{O_2}/F_{IO_2} < 200(\text{mmHg})$ as *moderate* ARDS and a value of $Pa_{O_2}/F_{IO_2} < 100(\text{mmHg})$ as *severe* ARDS [2]. Despite the ongoing debate on its precise definition and grading, ARDS is usually characterized by neutrophil infiltrates, increased concentration of inflammatory cytokines, increased microvascular permeability edema, alveolar flooding and surfactant inactivation by alveolar infiltrates. Surfactant inactivation and alveolar flooding will result in a widespread patchy *atelectasis*, defined as the collapse or closure of a lung unit. A lung unit which is isolated from ventilation is said to be *derecruited*. Atelectasis can reduce FRC down to 20-30% of the expected value: such a reduction in volume available for ventilation led to the concept of "*baby lung"* in ARDS patients [38]. A loss in aerated volume is, in an early stage, the main cause of reduced lung compliance in ARDS patients. In a more advanced phase, some patients may develop fibrosis, further reducing lung compliance and impairing blood oxygenation, due to a thickening of the blood-gas barrier. Mismatch between ventilation and perfusion ($\dot{\mathrm{V}}/\dot{\mathrm{Q}}$) and shunt are the main causes of hypoxia in ARDS patients. Hypoxia may then lead to pulmonary hypoxic vasoconstriction, increasing the pulmonary vascular resistance, and therefore to right heart failure, or *cor-pulmonale* [39]. A review of the complex heart-lung interactions, which is outside the scopes of this chapter, can be found in Pinsky [12]. Atelectasis, producing shunt, and a decreased lung compliance, will eventually lead to respiratory failure, which requires mechanical ventilation. Mechanical ventilation can in turn exacerbate the disorder, a condition known as Ventilator-induced Lung Injury (VILI), triggering inflammation which spreads to the whole body, causing organs failure and death [5].

1.2.2 Ventilator-induced lung injury (VILI)

Mechanical ventilation can be detrimental in both healthy and injured lungs, due to the high physical stresses and strains applied to the tissues [6]. Mechanical ventilation can initiate or worsen a preexisting injury, a condition described as *Ventilator-induced Lung Injury* (VILI). In the clinical setting, it occurs mainly in patients with ARDS, or patients with acute respiratory failure requiring mechanical ventilation, in whom the lung mechanical properties have already been impaired, as explained in the previous section. The goal of research in this field is to identify an appropriate ventilation strategy, which provides life support while minimizing the progression of the injury, in order to decrease mortality.

High mechanical strains on the lung tissue can be generated mainly by two mechanisms: *overdistension* or excessive stretch and cyclic opening and closing of lung units, defined as *atelectrauma*. The role of overdistension was the first one to be observed. It occurs at high V_T and leads to alveolar rupture and air leaks: this damage is called *volutrauma*. Alveolar rupture and tissue overdistension will lead to increased alveolar permeability, with the aforementioned inactivation of lung surfactant and reduction in FRC ("baby lung"). To be noticed that the "baby lung" increases the risk of volutrauma, since a given V_T is forced into a smaller inflatable lung, inducing a positive feedback which will accelerate VILI development. Evidence of lung overinflation injury, due to the redistribution of ventilation from atelectatic to non-atelectatic lung regions was found in rats by Tsushida et al. [40]. Overdistension is not necessarily related to high airway pressures imposed by the mechanical ventilator. If we consider Equation 1-1 we notice that overdistension could be present with low airway pressures and spontaneous respiratory efforts (positive P_{mus}, high P_{tp}) or absent with high airway pressure but chest strapping, limiting inflation. The evidence that high V_T and not necessarily high airway pressures were involved in injury was provided by Dreyfuss et al [41], and led to the concept of *volutrauma* as opposed to the previously adopted concept of *barotrauma*. This finding was further confirmed by a reduced mortality following the application of ventilation at low V_T (6ml/kg on average)[7].

Even if high tidal volumes are deleterious for the lungs, they have the advantage of reducing derecruited lung regions, thus improving oxygenation. Ventilation at low lung volumes, despite having improved the long-term survival, suffers from reduced lung stability and is prone to hypoxia and hypercapnia. At low V_T, associated in normal conditions to low alveolar pressures, lung units may collapse, due for example to inactivation of the surfactant. To every lung region a critical pressure can be associated, below which it will close. This notion has led to the application of a positive end expiratory pressure (PEEP) to reduce atelectasis at the end of expiration. The risk behind the collapse of lung units, is not only an increased atelectasis, but the cyclic opening and closing of these units during ventilation, the so called *atelectrauma*. Theoretical studies have shown that atelectrauma is associated to high stresses normal to the epithelial surface of the airways as they reopen or as the high-surface-tension liquid filling them is displaced, causing epithelial cell damage and necrosis [8], [9].

Three large trials were performed between 2004 and 2008 to investigate the effects of PEEP on mortality in ICU: ARDSNet Alveoli [42], LOVS [43] and Express [44]. They all failed in showing a difference in mortality when higher PEEP was applied with respect to lower PEEP. A subsequent meta-analysis showed a decrease in mortality with higher PEEP in the subset of patients with $Pa_{O_2}/F_{IO_2} < 200(\text{mmHg})$, associated to a lower survival in the subset of patients with $Pa_{O_2}/F_{IO_2} > 200(\text{mmHg})$ [45]. The risks of high PEEP in ARDS were underlined however by the ART trial which showed that an approach based on high PEEP to minimize atelectasis (maximal recruitment strategy) increased the mortality in patients with moderate and acute ARDS [46]. A strategy to determine the optimal PEEP value for each patient is still under investigation.

Atelectasis and overdistension are not separate concepts. As explained, overdistension and increased alveolar-capillary barrier permeability edema can induce atelectasis and alveolar flooding respectively, and a reduced volume of aerated lung can produce overdistension in healthy lung regions, which will receive most of the tidal volume. Another connection between the two is the concept of *stress raisers*, or *stress concentrators* [47]. Due to the mechanical interdependence of lung units, healthy tissue adjacent to atelectatic regions, will be subject to higher stretches during inflation. These regions will therefore be more subject to mechanical failure. Lung units interdependence is at the basis of complex interactions which make atelectrauma a highly dynamic and time-dependent phenomenon [14]. It follows that ARDS will favor VILI development, due to the presence of atelectasis, increased permeability edema, overdistension, which initiate or worsen the injury.

From a histological point of view, VILI is characterized by damages in the endothelial and epithelial surfaces [6] and by the presence of hyaline membranes. An increase in the concentration of inflammatory cytokines such as interleukin-6 (IL-6) and interleukin-8 (IL-8) [5] and of RAGE (Receptor for Advanced Glycation End products) [48] together with the recruitment of neutrophil and pulmonary macrophages is also observed. The inflammation originated in the lungs will spread to different organs, leading to multi-organ failure and death: this process is called *biotrauma*.

Despite the knowledge accumulated in the field of ARDS and VILI, the effort to decrease morbidity and mortality due to VILI is ongoing. The main strategy in intensive care units consists in ventilation with low V_T, use of PEEP and a maximal pressure limited to 30 cmH_2O [7]. A further intervention, which was shown to decrease mortality in patients with severe ARDS, is mechanical ventilation in prone position: it is thought to improve the ventilation-perfusion ratio and to improve regional lung mechanics and ventilation [49]. Although the role of excessive stress and strain to the lung tissue by positive-pressure ventilation is well established, it is still not understood how VILI is initiated and entertained at the alveolar level. Specifically, the mechanistic link between the mechanical stresses induced to the lung tissue through atelectrauma and the inflammatory response at an early stage is not understood. At the same time, there is still no direct observation of the effect of mechanical ventilation on alveoli and alveolar walls in *in-vivo* animal models. As reported in previous sections, the thickness of the alveolar walls (including the capillaries) is of the order of 10 µm: this imposes an upper limit on the spatial resolution required to visualize these structures, which should be ideally below 3 µm. The only technique capable of obtaining this resolution *in-vivo* has so far been synchrotron radiation computed tomography [13].

The next chapter will briefly review *in-vivo* lung imaging performed either with conventional sources or with synchrotron radiation. This description will permit to better identify the state of the art the beginning of the present work and the limitations hindering an increase in spatial resolution.

2 IN-VIVO LUNG IMAGING

2.1 THE IMPORTANCE OF *IN-VIVO* LUNG COMPUTED TOMOGRAPHY IN THE STUDY OF VILI

In Chapter 1, several open questions regarding VILI were presented. In particular, it is still unclear (i) how VILI is initiated and entertained at the alveolar level and (ii) what is the link between the mechanical stresses induced to the lung tissue during mechanical ventilation and the inflammatory response in an early stage of illness onset. One of the main experimental limitations in the study of these questions, is the absence of an *in-vivo* technique providing information on the lung parenchyma at the level of terminal airways and alveoli; in particular, on the regional response of the lung parenchyma following mechanical ventilation.

In clinics, the study of the lung mechanics in ARDS patients relies on the measurement of the static and dynamic lung compliance [30], the latter determined through the lung pressure-volume curve introduced in Chapter 1, or on the forced oscillation technique [50], which allows measuring the respiratory elastance (1/compliance) [51] (see Equation 1-3). A decrease in lung compliance is related to a decrease in FRC due to atelectasis and edema [52], as well as to changes in the mechanical properties of the lung tissue due to inflammation and high-permeability edema. Changes in lung compliance can be used to quantify opening and closing of lung units, by reproducing the time dependency of the compliance with computational models of the airway tree [53]. Variations in airway impedance were used by Suki et al. to study the recruitment of terminal airways: it was found that recruitment of the terminal airways is not continuous in time but is compatible with an avalanche process propagating down a branching structure once the critical pressure in the subtending airway is overcome [54]. Lung compliance and airway resistance are therefore important in the study of VILI, and approaches to personalize the mechanical ventilation based on the respiratory mechanics of the patient are under evaluation [30]. Despite the importance of respiratory mechanics in the clinical settings, these parameters provide information which is averaged over the whole chest-lung system. As a consequence, they do not provide direct information on the phenomena acting at the alveolar scale and they cannot be used to study the mechanistic link between overdistension and atelectrauma and the inflammatory response: the spatial distribution of VILI and mechanical stresses are in fact highly regional and heterogeneous.

Information on regional lung mechanics *in-vivo* can be provided mainly by four techniques: lung microscopy, magnetic resonance imaging (MRI), positron emission tomography (PET) and X-ray computed tomography (CT). Lung microscopy consists in opening the chest and acquiring a microphotography of the structures adjacent to the visceral pleura [55]. It has therefore two main limitations: it allows to visualize only the most external alveoli in contact with the lung pleura and requires opening the chest, thus modifying the transpulmonary pressure. MRI, PET and CT are instead 3D imaging techniques; they allow therefore to visualize every region of the lung parenchyma and they do not require to open the chest, preserving in this way the mechanical properties of the system under study. The main limitation of MRI has been so far the spatial resolution, on the order of a few hundred micrometers, which doesn't allow to visualize terminal airways and alveoli; the signal in MRI is moreover limited by the predominant fraction of air inside the lung volume. PET is a standard technique for functional lung imaging: it can be used to map regional lung inflammation in ARDS and VILI, regional ventilation and lung perfusion [56]. The spatial resolution is however limited to approximately 1 mm [57]. Recent developments in computed tomography with synchrotron radiation have shown instead the possibility of imaging the lungs *in-vivo*, in a mice animal model, using a pixel size of 3 µm [13]. This resolution is sufficient to visualize the alveoli and the alveolar septa as discussed in Section 1.2.2. Synchrotron radiation lung CT is therefore, presently, the only experimental technique capable of studying the mechanical behavior of the lung parenchyma under mechanical ventilation at the level of terminal airways and alveoli.

The aim of this chapter is therefore to: (i) briefly review the principles of computed tomography, focusing in particular on a technique used in synchrotron facilities, called *propagation-based phase contrast computed tomography* [58]; (ii) review the state of the art of *in-vivo* lung computed tomography and its limitations with regards to the challenges imposed by *in-vivo* imaging; (iii) introduce the main image analysis technique which can be used to address the open questions introduced in this paragraph, i.e. image registration.

2.2 COMPUTED TOMOGRAPHY IMAGING

X-ray computed tomography refers to the cross-sectional imaging of an object obtained illuminating it with X-rays from multiple directions. The importance of X-ray computed tomography, in what follows referred to as computed tomography or CT for simplicity, is that it is a low-invasive method which allows to view the morphology of an organ in three dimensions (3D), therefore avoiding the problem of superimposition of structures and the loss of information typical of projection techniques (2D), like x-ray radiography. In this section the physical and mathematical principles behind CT acquisition and reconstruction will be briefly reviewed; a more exhaustive description can be found for example in Kak et Slaney [59]. The basis of propagation-based phase-contrast CT and its importance in the imaging of soft tissues will be presented. A more rigorous and complete derivation of the physical laws governing X-ray interaction with matter and propagation based phase contrast imaging can be found in Paganin [60].

2.2.1 Signal formation: refractive index and projection approximation

Let's consider a monochromatic plane wave impinging on a sample and let its wave vector **k** be aligned with the z axis of a Cartesian coordinate system as in Figure 2-1. Let the sample be contained between the planes z=0 and z=z_0. The propagation of a monochromatic electromagnetic wave through a scattering field (the sample), can be described by the inhomogeneous Helmholtz equation [60]:

$$[\nabla^2 + k^2 n^2]\psi(x,y,z) = 0 \tag{2-1}$$

Where ∇^2 is the Laplacian operator, k the modulus of the wave vector of the electromagnetic wave and n the refractive index of the medium relative to the energy of the monochromatic plane wave. The complex refractive index, for X-rays, is close to unity and is usually expressed as:

$$n = 1 - \delta + i\beta \tag{2-2}$$

where i is the imaginary unit and $|\delta|, |\beta| \ll 1$. δ represents the refractive index decrement, which is related to the phase shifts of the electromagnetic wave in the matter and therefore, its deviation from the incident direction due to the scattering with the electrons of the medium [61]. β is the absorption index which is linked to the absorption of X-rays, mainly due to the photoelectric effect and Compton scattering.

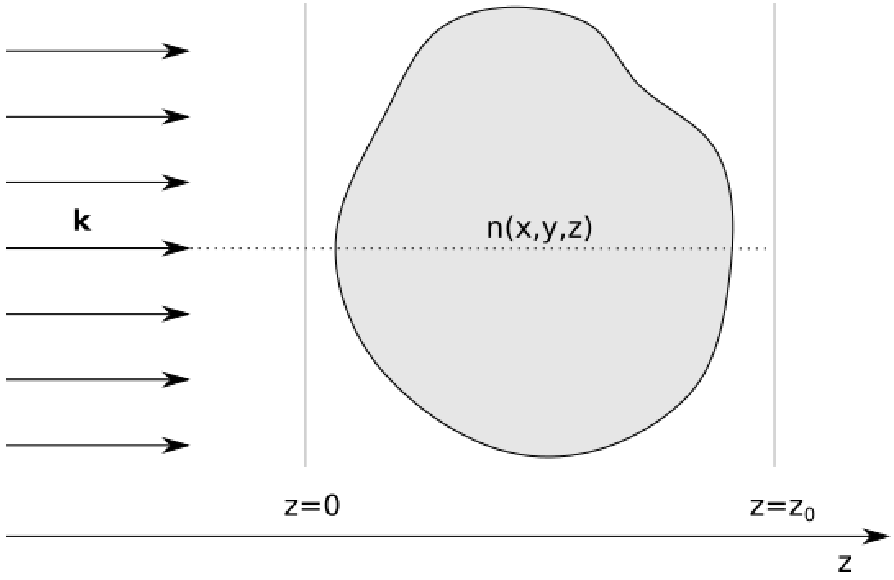

*Figure 2-1 Z-directed monochromatic plane wave with wave vector **k** incident on a scattering field contained in between the planes z=0 and z=z₀. The properties of the scattering field (sample) are characterized by the refractive index n. A solution for the electromagnetic wave at the exit surface is sought. The dotted line is the path an incident ray would take in the absence of the scatterers. Adapted from Paganin* [60].

With reference to the Figure 2-1, in order to study the propagation of the impinging plane wave through the sample, it is possible to solve the Helmholtz equation by expressing its solution $\psi(x, y, z)$ as a perturbed plane wave. A plane wave perturbed by the scattering field can be indicated by introducing a complex envelope $\tilde{\psi}(x, y, z)$ multiplying the unscattered wave e^{ikz}. Under the assumption that the sample interacts weakly with the X-rays, such that the ray paths can be considered negligibly perturbed with respect to those of the impinging plane wave (z directed dashed line in Figure 2-1), the solution at z=z$_0$ can be written as [60]:

$$\psi(x, y, z = z_0) = \tilde{\psi}(x, y, z = 0)e^{-ik\int_0^{z_0}[\delta(x,y,z)-i\beta(x,y,z)]dz} \qquad 2\text{-}3$$

This assumption is the so-called *projection approximation*. The refractive index decrement δ is responsible therefore for a phase shift:

$$\Delta\phi = -ik\int_0^{z_0}\delta(x, y, z)dz \qquad 2\text{-}4$$

but it doesn't affect the intensity $I(x,y,z)$ of the wave, which is proportional to the squared modulus $|\psi|^2$. The decrease in intensity is instead produced by the line integral of β along the direction of propagation of the wave:

$$ln\left[\frac{I(x,y,z=z_0)}{I(x,y,z=0)}\right] = -2k\int_0^{z_0}\beta(x,y,z)dz \qquad 2\text{-}5$$

This equation corresponds the Lambert-Beer law once the *linear attenuation coefficient* μ is expressed as

$$\mu = 2k\beta \qquad 2\text{-}6$$

2.2.2 Tomographic reconstruction: Fourier slice theorem and filtered back projection

When a conventional X-ray tomography is acquired, the detector is positioned just behind the sample, in the plane defined as $z = z_0$ in Figure 2-1. The fact that we are considering a plane wave as an input, allows to simplify the mathematical description of tomographic acquisition and reconstruction and is a condition which well approximates the X-ray beam in synchrotron radiation facilities, as will be explained in Chapter 3. The intensity measured by the detector in this geometry is proportional to the squared modulus of $\tilde{\psi}(z = z_0)$, defined in Equation 2-3. If the intensity of the impinging plane wave ($\tilde{\psi}(z = 0)$) is known, then the right hand side of Equation 2-5 can be computed: this quantity is known as *parallel projection* $p(x,y)$:

$$p(x,y) = \int_{-\infty}^{\infty}\mu(x,y,z)dz \qquad 2\text{-}7$$

Where we have assumed that $\mu(x,y,z) = 0$ everywhere outside the sample. For sake of simplicity let's consider a 2-D slice of the sample, with linear attenuation coefficient $\mu_0(x,z) = \mu(x,y = y_0,z)$. Under the assumptions of (i) impinging plane wave and (ii) projection approximation, a 2D sample can be considered without loss of generality, since no coupling is present in the (x,y) plane. For a generic plane wave, whose wave vector $\boldsymbol{k}_\theta$ forms an angle θ with respect to the z axis, a parallel projection can be written as:

$$p_\theta(t) = \int_{-\infty}^{\infty}\int_{-\infty}^{\infty}\mu(x,y)\delta_D(xcos(\theta) + ysin(\theta) - t)dxdy \qquad 2\text{-}8$$

Where δ_D is the Dirac delta function and the line integral is computed along the ray impinging on the detector at the coordinate t, as in Figure 2-2.

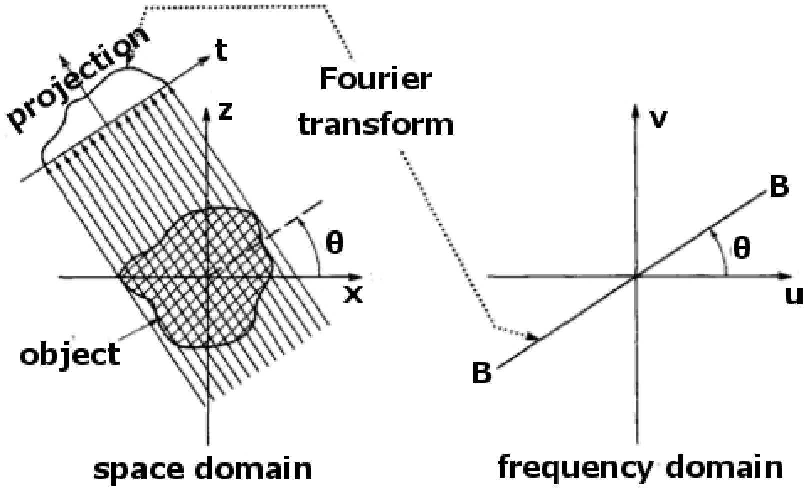

Figure 2-2 Schematic representation of a projection acquired illuminating the sample at an angle θ (space domain) and of the Fourier slice theorem, which establish a correspondence between the Fourier transform of a projection and the Fourier transform of the sample (frequency domain). Adapted from Kak et Slaney [59].

Tomographic reconstruction is a procedure which consists in recovering $\mu(x,y)$ from its parallel projections and is based on the *Fourier Slice Theorem.* Let's define the Fourier transform of $\mu(x,y)$ and of its parallel projections as:

$$F(u,v) = \int_{-\infty}^{\infty}\int_{-\infty}^{\infty} \mu(x,y)e^{-i2\pi(ux+vy)}dxdy \qquad 2\text{-}9$$

$$S_\theta(w) = \int_{-\infty}^{\infty} p_\theta(t)e^{-i2\pi wt}dt \qquad 2\text{-}10$$

If we express $F(u,v)$ in polar coordinates $(u,v) = (wcos(\theta), wsin(\theta))$ the Fourier Slice Theorem states that:

$$S_\theta(w) = F(w,\theta) \qquad 2\text{-}11$$

The Fourier transform of the parallel projection of the function $\mu(x, y)$ taken at an angle θ gives a slice at an angle θ of the 2D Fourier transform of $\mu(x, y)$.

By acquiring parallel projections at different angles, we are therefore sampling the Fourier transform of the linear attenuation coefficient in polar coordinates, as shown in Figure 2-2. The linear attenuation coefficient will then be recovered in cartesian coordinates by inverse Fourier transform. It is possible to show that:

$$\mu(x, y) = \int_0^{\pi} \left[\int_{-\infty}^{\infty} S_\theta(w)|w|e^{i2\pi w(x\cos\theta + y\sin\theta)} dw \right] d\theta \qquad \text{2-12}$$

Where |w| is the Jacobian of the transformation to polar coordinates. Equation 2-12 is the so-called Filtered Back Projection (FBP) algorithm. Each parallel projection is filtered in the Fourier space and back projected along the line $t = x\cos\theta + y\sin\theta$. Since in the back projection the same weight is given to all the parallel projections and that a limited number of parallel projections can be acquired, a uniform angular sampling is required.

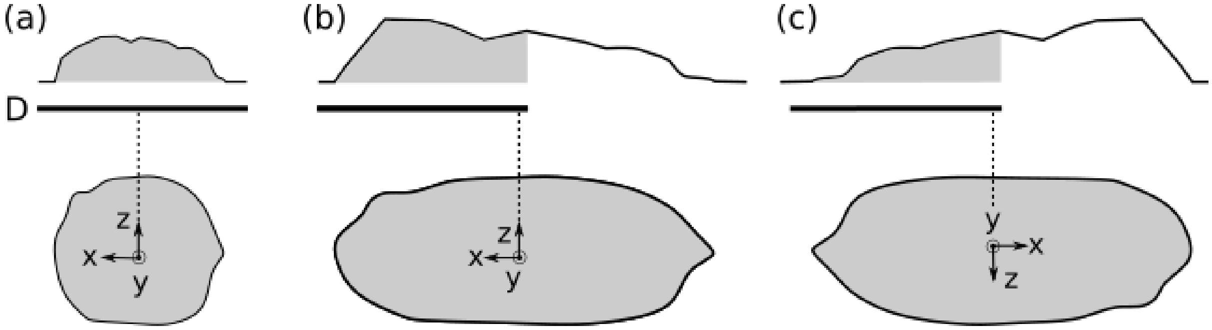

Figure 2-3 Scheme of tomographic acquisition with rotation of the sample around the y axis. (a) Conventional tomography: the parallel projection of the sample is completely covered by the field of view of the detector D and the axis of rotation is projected onto the center of the detector. (b-c) Half tomography acquisition: the field of view is virtually doubled projecting the rotation axis onto the edge of the detector: One half of the parallel projection is acquired at the angle α (b); the second half at $(\alpha + \pi)$ (c).

Figure 2-3 (a) represents the typical tomographic acquisition scheme in synchrotron facilities. The X-ray beam and the detector are fixed with respect to the laboratory, and the angular sampling is performed rotating the sample and the Cartesian coordinate system (x,y,z) around the $\hat{y}$ axis. The rotation axis is projected at the center of the detector. In presenting the FBP, it was tacitly assumed that the parallel projection was known for $t \in (-\infty, \infty)$. Since both the detector and the sample have finite extension, it is sufficient for the parallel projected sample to be fully contained in the field of view of the 1D detector. If the sample is larger than the field of view of the detector, as in Figure 2-3 (b-c), a property of the parallel projections can be utilized: it is equivalent, from the point of view of the obtained image, to illuminate the sample with a plane wave at α and at α+π. If the axis of rotation $\hat{y}$ is moved, such that its projection falls at one edge of the detector, and if the sample is narrower than two times the field of view of the detector, the part of the parallel projection falling outside the field of view at α (Figure 2-3 (b)), can be recorded at α+π (Figure 2-3 (c)). This geometry is called *half acquisition tomography.*

If the sample is larger than two times the field of view of the detector, it can't be fully reconstructed, since part of the information is missing. This particular case, referred to as *local tomography* or *region of interest tomography,* is common when high spatial resolutions, and therefore small fields of view, are required. The sample can be reconstructed in the circle centered on the axis of rotation and with diameter equal to the field of view of the detector, but the interaction of the X-rays with the regions outside this circle will cause artefacts in the reconstruction [62].

2.2.3 Propagation-based phase contrast imaging (PBI)

In Section 2.2.1 the equation of a plane wave propagating through a sample was computed at the exit surface of the sample. It was found that the refractive index decrement δ was responsible for a phase shift $\Delta\phi$, while the absorption index β for the intensity attenuation. In conventional tomography, in which the detector is placed at the exit surface of the sample, it is therefore possible to reconstruct only a map of the absorption index. This is a limiting factor in medical applications, since the tissues to be imaged are usually formed by low Z materials (Hydrogen, Carbon, Oxygen,..), weakly absorbing at the energies of interest (10 – 100 keV); the resulting contrast between tissues is therefore low. Utilizing a wave propagation model based on re-radiation from bound electrons in dielectric materials, it is possible to show that, far from discontinuities due to photoelectric absorption: (i) $\delta \propto \rho_e/E^2$ and (ii) $\beta \propto \rho_e/E^4$ [63], where ρ_e is the electron density and E the energy of the electromagnetic wave. Due to the different dependency on the energy, at the energy of interest for medical imaging, δ can be three orders of magnitude greater than β. A method sensitive to δ could therefore provide an increased contrast within soft tissues with respect to conventional tomography.

The class of techniques sensitive to the phase shift induced by the sample is called *Phase Contrast Techniques.* A complete review on the different strategies to convert the phase information in intensity modulation can be found in Bravin et al. [58]. Propagation-based phase contrast imaging (PBI) [64] is here described: due to the simple setup required and to the fast acquisition speed achievable, it is at the moment the only technique compatible with the constraints imposed by *in-vivo* lung imaging (Section 2.3).

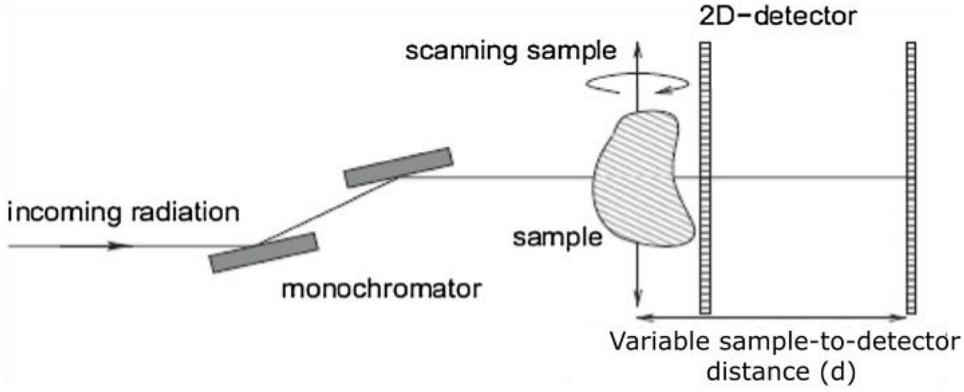

Figure 2-4 Scheme of propagation-based phase contrast imaging. Free space propagation of the perturbed wave front exiting the object creates interference fringes, which modulate the intensity recorded by the detector at the boundaries between different objects or tissues. By changing the propagation distance (d), it is possible to optimize the visibility of different spatial frequencies in the object. Image from Keyriläinen et al [65].

A scheme of the experimental setup for propagation-based phase contrast imaging is reported in Figure 2-4. In this technique the detector is not positioned at the exit surface of the sample, as in conventional tomography, but is moved along the direction of propagation of the beam. Free propagation of the perturbed plane wave exiting the sample (Equation 2-3) results in intensity variations caused by the phase shift, as can be derived using the Fresnel diffraction theory [66]. Based on the free propagation distance d, i.e. the distance between sample and detector, three regimes can be distinguished [64]: (i) $d \sim 0$ (absorption regime) described in the previous section;

(ii) $d \leq 1/\lambda f^2$ where λ is the wavelength of the monochromatic radiation considered and f is a spatial frequency of interest inside the sample (Fresnel or near-field regime); (iii) $d > 1/\lambda f^2$ (Fraunhofer regime). When the Fresnel regime is used, the intensity modulation caused by the propagation can be described by the Transport of Intensity Equation (TIE) [67] and is proportional to the transverse Laplacian of the phase shift Δϕ at the exit surface of the object (Equation 2-4). These intensity modulations are particularly strong at the edges between different tissues: this effect is called edge enhancement. The main requirement in phase contrast imaging is a sufficient *transverse spatial coherence* of the beam. The concept of coherence will be introduced in Chapter 3; in PBI the condition imposed is $\lambda L f/s > 1$ where L is the distance of the sample to the X-ray source of size s [58].

Considering Equation 2-4, it is possible to notice that the phase shift is the line integral, or parallel projection, of the refractive index decrement of the sample. Computing the phase shift at the exit surface at different angles, would therefore allow to reconstruct a map of the refractive index decrement, as seen in Section 2.2.2, yielding a higher contrast between soft tissues with respect to the absorption coefficient. Several algorithms have been proposed to retrieve the phase shift from one or multiple images acquired at different propagation distances; a review can be found in Burvall et al. [68]. Multiple distances are necessary to untangle the contribution of absorption and phase to the image intensity. In *in-vivo* imaging, however, projections acquired at different distances cannot be combined to retrieve the phase due to the motion of the sample in between acquisitions and single distance algorithms are therefore required. The single distance algorithm which is most used in medical applications was proposed by Paganin [69] and is based on the inversion of the Transport of Intensity Equation: it is therefore valid only in the Fresnel regime. In order to untangle phase and absorption, a constant ratio between δ and β is assumed.

2.3 *IN-VIVO* IMAGING AND DYNAMIC 3D LUNG MICROSCOPY

In Section 2.2.2 the mathematical foundations of computed tomography were presented. When introducing the acquisition of parallel projections at different angles and the following reconstruction with the FBP algorithm, we have tacitly assumed that the function to be recovered, $\mu(x, y, z)$ or $\delta(x, y, z)$ in the case of PBI, didn't have a time dependency. In other words, the sample to be imaged doesn't change in time. This condition is not met when performing *in-vivo* experiments. Let's consider the case of the lungs, the object of this Thesis work. The complex structure of the lung, described in Section 1.1.1, is continuously displaced by two main sources of motion: (i) breathing (spontaneous or through mechanical ventilation) and (ii) cardiovascular pulsations. When the time dependency of the sample is considered we fall in the domain of time-resolved or dynamic CT. When micrometric spatial resolution is required, we can introduce the term *dynamic 3D microscopy*. Two conditions must be satisfied in order to reconstruct a tomography free from motion artefacts. The first one is that the local motion of the sample during the acquisition time of a projection should be smaller than the pixel size. The second is that all the parallel projections should be acquired at time instants when the volume is in the same state $\bar{\mu}(x, y, z)$, up to differences smaller than the pixel size. The first condition implies that, for a given motion, the acquisition time per projection must decrease when increasing the spatial resolution. In the case of the lung motion in a mouse, it was for example found that an integration time of 3 ms was required to get a spatial resolution of 3 µm [70]. In order to maintain the same statistics on each pixel, which is correlated to the signal to noise ratio of the images, and, ultimately, to the detail visibility, a high X-ray flux is needed, which is available only in synchrotron facilities. The second condition requires a synchronization between the motion of the sample and the acquisition system. In ideal conditions, a perfectly periodic motion would be needed: a parallel projection is then acquired at the selected phase at every period.

2.3.1 Synchronization between a physiological motion and the tomographic acquisition

In order to synchronize a physiological motion, such as heart contraction and expansion, with the tomographic acquisition, a (set of) physiological signal describing the phase of the motion is required. In the example of the heartbeat, the time elapsed from the R wave in the electrocardiogram (ECG) signal is used to describe the phase of the heart contraction and expansion. The approaches found in the literature can be in general divided in two classes: *prospective* and *retrospective gating*.

In the prospective gating approach, the physiological signal (e.g the ECG) is recorded and analyzed during the tomographic acquisition; whenever the required phase is reached, a projection is acquired. The advantages of this approach are that (i) the sample is irradiated only during the phase of interest, thus reducing the probability of radiation damage; (ii) since the acquisition is synchronized with the motion, the time resolution is limited only by the acquisition time of the projection. The time resolution is here defined as the time interval associated to a single phase during the reconstruction.

In the retrospective gating approach instead, the physiological signal is recorded during the tomographic acquisition, but is analyzed *a-posteriori*. Projections are acquired at a constant frame rate, independently from the physiological motion. During the tomographic reconstruction, the physiological signal is analyzed to associate to each projection the phase of the motion at which it was acquired. With respect to the prospective gating several phases of the motion can be acquired during the same scan, providing a 4D dataset (3D + time), at the cost of a reduced time resolution. Since the acquisition is not synchronized with the motion, the time resolution is limited by the reciprocal of the frame rate plus the acquisition time of a projection.

2.3.2 *In-vivo* dynamic 3D lung microscopy: biological challenges

The first challenge to be faced when imaging biological samples *in-vivo*, is that the ideal condition of periodic motion is never achieved. In the lungs two sources of motion are present: cardiovascular contractions and breathing. Even if these two sources can influence each other, due to complex heart-lung interactions, they are in general asynchronized. Breathing can be controlled, both in amplitude and frequency, by means of mechanical ventilation and deep anesthesia; the heartbeat frequency is however determined by the instantaneous physiological condition of the living animal and is subject to strong variability. The image quality and resolution achieved by the different approaches to dynamic 3D lung microscopy depend on how the problem of the asynchrony between mechanical ventilation and heart motion and the problem of the heart rate variability are treated. A review on the state-of-the-art of dynamic 3D lung microscopy will be presented in Section 2.4.

A further biological challenge in *in-vivo* imaging, which must be considered when using X-rays, is given by the radiation damages induced on the tissues. A discussion of the relation between radiation dose and biological damage is out of the scope of this Thesis, however immediate effects of the radiation on the sample during a tomographic acquisition have been reported, for doses higher than 1 kGy [71].

2.4 STATE-OF-THE-ART OF *IN-VIVO* 3D LUNG MICROSCOPY

Time-resolved CT is commonly performed in clinics, with conventional tomographic scanners [72], and in small animal models, either with microfocus sources and in synchrotron radiation facilities [10], [13], [14], [73]–[75], covering therefore a wide spectrum of applications and of spatial resolutions (1 mm - 1 µm). A review on low-resolution clinical implementations of prospective and retrospective cardiac gated techniques can be found in Halliburton et al. [72]. In the following paragraphs I will focus on micro-CT and synchrotron radiation imaging, due to their capabilities in producing high spatial resolution images.

2.4.1 *In-vivo* 3D microscopy with microfocus sources

In the past years, *in-vivo* lung micro-CT techniques were developed in small animal models reaching a spatial resolution between 200 [73] µm and 50 µm [74]. Both prospective and retrospective gated approaches were applied, acting mainly on the ventilation and neglecting the cardiac motion, obtaining therefore motion artefacts around the heart.

A prospective gating approach was developed by Ford et al in a rat model, using a commercial micro-CT scanner [73]. The peculiarity of this technique was that it utilized free-breathing animals, therefore the ventilation was not controlled and non-periodic. A pressure chamber in contact with the chest of the animal was used to monitor lung inflation and deflation. A projection was acquired per breathing cycle, at a given delay from the beginning of the inspiration; heart motion was not considered. The maximum time resolution of the scan, given by the minimum acquisition time of a projection, was of 300 ms, for a total scan duration of 20 minutes, corresponding to a radiation dose of 190 mGy. A pixel size of 90 µm was used, with an estimated spatial resolution between 135 µm and 210 µm depending on the respiratory phase.

This technique was further developed, extending it to a retrospective gating approach [74] in a free-breathing mouse model and with a commercial micro-CT system. Gating was based on lung volume only. The same pressure chamber described in the previous approach was used to monitor the lung inflation, but projections were acquired continuously. For the reconstruction, projections were sorted selecting time intervals of minimum 50 ms around peak inspiration; added to an integration time of approximately 10 ms, a time resolution of 60 ms was achieved, associated to a spatial resolution of 150 µm and a scan time of 30s. The dose delivered to the sample during the whole scan was 170 mGy.

During the last year of this Thesis work, a micro-CT technique with a spatial resolution of approximately 50 µm was reported by Preissner et al. [75]. It was developed in a mouse model using a liquid-metal jet anode X-ray source. The animals were mechanically ventilated, and the acquisition system was synchronized with the mechanical ventilator. Projections were acquired at a constant frame rate, as in a retrospective gated approach; since the respiratory motion was controlled and perfectly periodic, and the acquisition synchronized with it (the frequency is a super-harmonic of the respiratory rate), the time resolution was given, as in a prospective gating approach, by the acquisition time of a projection. The total acquisition time, depending on the respiratory rate, was approximately 8 minutes with a time resolution of 20 ms and a dose of 30 mGy per CT reconstruction (550 mGy in total), achieving a spatial resolution of 50 µm (25 µm pixel size), estimated from the smallest structure visible in the reconstruction. The spatial resolution was however not homogeneous, since motion artefacts remained around the heart.

Even if space and time resolution were greatly improved by Preissner et al., techniques based on microfocus sources are still limited in flux and field of view: only small animals can be imaged, and the alveolar scale cannot be reached. Both limitations can be overcome using synchrotron radiation, as will be discussed in the next section.

2.4.2 *In-vivo* 3D microscopy in synchrotron radiation facilities

In synchrotron radiation facilities several lung imaging techniques were developed, among them: phase-contrast CT [76], 4D lung imaging [13], virtual histology of lung tissue [77], [78], K-edge subtraction imaging for lung perfusion [79] and speckle-based airflow measurements [80]. This variety of techniques is allowed by the high photon flux, meeting the combined need for high resolution and short integration time of *in-vivo* imaging, and by the small source size coupled to large source to sample distances, which provides the high spatial coherence required by phase contrast techniques such as PBI (Section 2.2.3). Lungs are particularly suited for phase contrast techniques: thanks to their large air volume, they are characterized by low X-ray absorption; the alveolar structure, made up by numerous air-tissue interfaces, generates multiple refraction which produces strong interference fringes when associated to free propagation, visible as speckles in projections [76]. If PBI is combined with the application of phase retrieval algorithms, images with a strongly increased contrast-to-noise ratio can be obtained. which inherit the potential for significant reduction in X-ray dose [81]. Despite all the applications developed using synchrotron radiation, we will focus in this section on propagation-based dynamic 3D microscopy, subject of this Thesis.

One of the first developments in the field of time resolved lung 3D microscopy in synchrotron facilities was carried out by Sera et al. [82] to visualize small airways and coronary arteries in mice and rats; this technique was developed at the Spring-8 synchrotron in Japan. It was based on prospective heart gating: short respiratory pauses (300 ms) were induced at the end of expiration; during the respiratory pause, the ECG was used to trigger the acquisition of a projection at a given delay from the R peak. This technique allowed to reconstruct one heart phase per scan at a constant pressure. A pixel size of 12 µm was used in the specific case of the mouse model, with an acquisition time per projection of 20 ms; the diameter of the smallest airway visible in the reconstruction was 125 µm. The scan duration (in mice) was 7.5 minutes and utilized a monochromatic beam of 20 keV; the total radiation dose of approximately 2 Gy.

A second approach was reported by Dubsky et al. and was also developed at Spring-8 [10], allowing to measure local tissue expansion and airflow in mice and newborn rabbits. This approach was based on a pure respiratory gating; the heart motion was neglected, causing motion artefacts in the ventral region. The image acquisition was synchronized with a custom-made mechanical ventilator, providing a stable and known periodic motion, along which up to 50 phases were selected, tuning the acquisition frequency to the appropriate super harmonic of the respiratory rate. A time resolution of 20 ms was achieved, associated to a pixel size of 20 µm. The animals were irradiated with a monochromatic beam of 24 keV, with total dose of 800 mGy.

This approach was further developed by Dubsky et al. to introduce cardiac gating and was applied to the study of the cardiac induced airflow in the lung in mice [83]. The acquisition was synchronized with the mechanical ventilation, as in the previous approach, but the projections were retrospectively divided in cardiac phases, based on the ECG. Due to the asynchrony of heart-beat and mechanical ventilation, the cardiac motion was studied only in projections acquired at the end of the expiration, when the lung motion was minimized. A pixel size of 15 µm was used. No information on the time resolution achieved and on the dose was given.

The only successful attempt to perform 3D microscopy at a spatial resolution lower than 10 µm was achieved up to this moment by Lovric et al. at the Swiss Light Source (SLS, Paul Scherrer Institute, Switzerland) in a rat model [13]. A pixel size of 1 µm and 3 µm was used, allowing to visualize alveoli and alveolar walls. This technique was based on a single respiratory pause (90 s - 140 s) and on prospective cardiac gating. The long respiratory pause caused however an irregular heart motion: in these conditions, a successful gating was obtained acquiring projections only at the end of the cardiac cycle, just before the following R wave, when the heart motion was minimized. Such a high spatial resolution was obtained coupled to a time resolution of 3 ms and at the cost of sacrifying dynamic information. The cardiogenic motion could in fact not be studied, and since a constant pressure was used, inflation could be investigated only acquiring consecutive scans at different lung pressure levels (quasi-static inflation). A monochromatic beam was used at an energy of 21 keV, yielding a total dose of 90 Gy.

The only lung imaging technique applied to VILI utilizing synchrotron radiation was reported by Broche et al. [14] in a rabbit model at the European Synchrotron Radiation Facility (France). Even if it was not based on respiratory or cardiac gating, this work was important for this Thesis because it was applied to an animal model of VILI. This technique was based on a short respiratory pause, during which a full CT was acquired with fast continuous rotation and without cardiac gating; the total acquisition time was 21 s. A pixel size of 45 µm was used, with monochromatic radiation of 65 keV. The advantage of this fast technique, compared to the slow gated ones, is the possibility to observe short term changes in the lungs. It allowed to visualize short-term opening and closing of lung units and to correlate it to the mechanical interdependence of neighboring acini.

2.5 STUDYING REGIONAL LUNG DEFORMATION IN DYNAMIC 3D LUNG MICROSCOPY: IMAGE REGISTRATION

In this section, image registration, a technique commonly used to analyze dynamic lung computed tomography will be briefly introduced. In the literature it was used to estimate lung parenchymal motion to improve radiotherapy treatments [84] and to estimate local ventilation [85]. For more information concerning the different facets and the complexity of medical image registration we make reference to [86], [87].

2.5.1 Image registration: general theory

Let us consider two volumes representing the same object at different time frames or the same volume acquired with different imaging modalities. We define image registration the process which allows to determine a spatial correspondence between homologous structures in the two volumes. In other words, it consists in finding a spatial transformation which maps coordinates in one volume, called the reference volume, to corresponding points in the second volume, called moving or test volume. If $I_r\ (\boldsymbol{x})\colon \Omega_r \subset \mathbb{R}^3 \to \mathbb{R}$ is the reference volume and $I_m\ (\boldsymbol{x})\colon \Omega_m \subset \mathbb{R}^3 \to \mathbb{R}$ the moving volume, the problem consists in finding a function $\mathbf{g}(\boldsymbol{x})\colon \Omega_\mathrm{m} \to \mathbb{R}^3$ such that $I_m\ (\mathbf{g}(\boldsymbol{x})) = I_r\ (\boldsymbol{x})$. According to the transformations, the registration can be (i) rigid, if it preserves the distance between points, (ii) affine if it maps parallel lines to parallel lines and (iii) non-rigid or elastic if it maps straight lines to curves. Image registration is a minimization problem characterized in general by three components:

1. Deformation model: imposing constraints on the class of transforms to be used;
2. Cost function: the function to be minimized expressing the distance or similarity between the two volumes;
3. Optimization strategy: the algorithm to be used for the minimization.

The choice of the deformation model is of fundamental importance, since it will determine a balance between computational effort, accuracy and level of details achievable. There are two main properties desired when estimating a transformation:

1. Inverse Consistency: denoting $\mathbf{g}_{AB}$ as the transformation mapping B onto A and $\mathbf{g}_{BA}$ the transformation mapping A onto B, in general $\mathbf{g}_{AB} \neq \mathbf{g}_{BA}^{-1}$. The inverse consistency requires that the forward and the backward transformations are the inverse of each other
2. Topology Preservation and Diffeomorphism: this property requires the transformation to be bijective[1] and the determinant of the Jacobian[2] to be greater than zero.

Two main classes of transformations can be identified [86]:

1. Based on physical models;

---

[1] A transformation is defined bijective if every point of the fixed image is paired with one and only one point of the moving image and *vice versa*

[2] The Jacobian is the matrix containing the first spatial derivatives of the transform **g**

2. Based on approximation and interpolation theory.

The first class contains deformations based on physical models and continuum mechanics, for example linear elasticity or viscous fluid flow. The former describes the moving volume as an elastic body and its deformation is governed by the Navier-Cauchy equation [88]. In this model the force driving the elastic deformation has two components: one proportional to the difference between the volumes, leading to the actual deformation, and an elastic recoil. The main limitation of this approach is that it is accurate only for small deformations. The latter instead describes the volume as a viscous fluid, with a deformation described by the Navier-Stokes equation [89]. This approach is valuable for large deformations, and can be limited to diffeomorphic transformations, but this is obtained at the cost of computational efficiency.

In the second class instead, no assumption is made on the physical properties of the volumes and the transformation is approximated by a linear combination of basis functions. A common choice in medical image registration is the use of cubic b-splines, since they have a compact support and allow to describe highly local deformations [90], [91]. The main advantage of the approach based on approximation and interpolation theory is that a low number of parameters is used to define the transformation, increasing the computational efficiency; this approach moreover provides smooth deformations. The main drawback is the fact that in general the topology is not preserved. This approach is also known as Free-Form Deformation (FFD).

As previously stated, the cost function is a metric which measures the similarity between the volumes and is the function which is minimized during the registration process. It usually consists of two terms:

$$E_c(\boldsymbol{\Theta}) = \mathcal{M}\left(I_m\left(\boldsymbol{g}(\boldsymbol{\Theta},\boldsymbol{x})\right), I_r\,(\boldsymbol{x})\right) + \epsilon\mathcal{R}(\boldsymbol{\Theta}) \qquad \text{2-13}$$

Where $\boldsymbol{\Theta}$ is a vector of parameters defining the transformation $\mathbf{g}$, $\mathcal{M}$ is a similarity metrics describing how well the volumes are aligned and $\mathcal{R}$ is a regularization term, acting on the transformation to avoid negative or singular Jacobian. ϵ is a weight, which allows to tune the effect of the regularization term: it allows to reduce folding or excessive deformations but can prevent the optimal solution to be found if its relative contribution is too high. A common choice for the similarity metrics $\mathcal{M}$, if the volumes are acquired in the same modality and therefore the same voxel attributes are expected, is the cross-correlation or the sum of square difference of the volumes; the mutual information is used instead for inter-modality registration [92]. These metrics can be calculated on all the voxels or on a random sampling in order to find a balance between accuracy and computational time. Other approaches to quantify the difference between the volumes are based on the distance between landmarks or known surfaces but rely on a good definition of the landmarks or on a good segmentation and often do not allow to estimate the transformation with high spatial accuracy in all the volume.

The last main component to be chosen in image registration is the optimization algorithm. Usually continuous methods are used. In these methods the minimization of the cost function is performed with a generic update rule of the form:

$$\boldsymbol{\Theta}_{i+1} = \boldsymbol{\Theta}_i + \alpha_i \boldsymbol{d}_i(\boldsymbol{\Theta}_i) \tag{2-14}$$

Where $\boldsymbol{\Theta}$ is the vector of parameters defining the transformation, i the step number, $\boldsymbol{d}$ a search direction and α a weight defining the length of the step along the search direction. Several algorithms can be used to define the search direction, which can be based on the first order derivatives of the cost function with respect to the parameter vector, the Jacobian, or on the second order derivatives, the Hessian. To the first class belong the Gradient Descent (GD) [93] and the Conjugate Gradient (CG) methods [94]. To the second class the Quasi-Newton (QN) methods, in which the search direction is based on the inverse of the Hessian ($\mathcal{H}$) as:

$$\boldsymbol{d\Theta} = -\mathcal{H}^{-1} \cdot \boldsymbol{\nabla} E_c(\boldsymbol{\Theta}) \tag{2-15}$$

The QN methods are based on an approximate estimate of the Hessian. Among all, the Broyden-Fletcher-Goldfarb-Shanno (BFGS) and its variant Low Memory Broyden-Fletcher-Goldfarb-Shanno (L-BFGS) [95] in which the Hessian is not computed, but the product between the inverse Hessian and the gradient of the cost function is estimated with a recursive relation using the estimates of the gradient and of the search direction of the previous m steps (m≃20). Several approaches can be adopted to estimate the size of the step α as well, going from constant values, to a constant decrease at every step and to exact or inexact Line Search (LS) approaches. The latter approach tries to minimize the function along the search direction exactly or up to a user-defined approximation. Once more, criteria can be defined in the choice of the step length in order to avoid excessive deformations or negative and singular Jacobian.

Image registration is therefore a challenging task, in which all the above components can be optimized, and strategies can be adopted to simplify the optimization avoiding local minima.

2.5.2 Elastic image registration based on B-spline transformations

A common approach found in the literature for lung image registration is based on 3-D and 4-D B-spline approximations [96], [97]. B splines of order n are piecewise polynomials of the same order. The points where the polynomials meet are called knots: B-splines are C^{n-1} continuous at the knots. Given a set of knots $\{x_i\}$ in $\mathbb{R}$, the B-spline of order 0 applied to x_i is defined as:

$$\beta_{i,0} = \begin{cases} 1 & if\ x_i < x < x_{i+1} \\ 0 & otherwise \end{cases} \qquad 2\text{-}16$$

B-splines of order n are given by n self-convolutions of β_0 and extend over n+2 knots. Polynomials defining a third order B-spline (all expressed in the interval [0,1)) are the following:

$$\begin{aligned} \beta_{0,3} &= \frac{(1-x)^3}{6} \\ \beta_{1,3} &= \frac{3x^3-6x^2+4}{6} \\ \beta_{2,3} &= \frac{-3x^3+3x^2+3x+1}{6} \\ \beta_{3,3} &= \frac{x^3}{6} \end{aligned} \qquad 2\text{-}17$$

When applied to image registration they are used to approximate the transformation **g**. A uniform mesh is defined over the volume, with spacing $\delta_x, \delta_y, \delta_z$. The transformation function is defined through the tensor product of the aforementioned 1D B-splines as:

$$\boldsymbol{g}(\boldsymbol{x},\boldsymbol{\Theta}) = \boldsymbol{x} + \sum_{l=0}^{3}\sum_{m=0}^{3}\sum_{n=0}^{3} \beta_{l,3}(u)\beta_{m,3}(v)\beta_{n,3}(w)\boldsymbol{\Theta}_{i+l,j+m,k+n} \qquad 2\text{-}18$$

Where $i = \lfloor x/\delta_x \rfloor - 1,\ j = \lfloor y/\delta_y \rfloor - 1,\ k = \lfloor z/\delta_z \rfloor - 1$ and $u = x/\delta_x - \lfloor x/\delta_x \rfloor,\ v = y/\delta_y - \lfloor y/\delta_y \rfloor,\ w = z/\delta_z - \lfloor z/\delta_z \rfloor$. $\boldsymbol{\Theta}_{i,j,k}$ is a vector which parametrizes the displacement at the knot (i,j,k). According to this definition, each point will act on the neighboring ones with a weight given by a cubic B-spline centered on it. When the parameters are equal to zero the identity transformation is obtained. 4-D B-splines are used as well in the literature in 4D registration techniques, in which all the time frames of a dynamic CT are registered simultaneously towards their time average. It allows to obtain smooth deformation fields as a function of time. An example of 4D registration technique can be found in Zhao et al. [97].

The size of the grid in a B-spline approach determines the level of resolution of the estimated transformation: a coarse grid doesn't allow to describe local deformations, but a fine grid is more sensitive to noise. The number of parameters $\boldsymbol{\Theta}_{i,j,k}$ to be estimated goes moreover as 3 times the number of knots, reaching a value of 3000 with a simple 10×10×10 grid. In order to minimize the cost function in this high dimensional space avoiding local minima, one strategy consists in a multiresolution approach. A first coarse grid is applied to a resampled image, to find the largest displacements. After that procedure, the resampling is reduced and the grid refined to describe the smallest deformations. More details about the multiresolution approach can be found in Kybic et al. [98].

2.5.3 Results of the elastic image registration procedure

A topic which is under debate in the literature is how to evaluate the quality of the registration. One possibility is to find landmarks and to study their distance when the transformation is applied; a second possibility is to segment structures of interest and to study how well they overlap. A simpler approach consists in a visual and therefore subjective evaluation of the result. In this case, the difference between the reference volume and the transformed test volume, referred to as *moved* volume, can be computed voxel by voxel and checked. A second approach, alternative to the voxel by voxel difference, is to compute a checkerboard image: bringing forward the comparison with a checkerboard, the image is divided into cases: the cases contain alternately pixels from the reference image and pixels from the moved image. If the registration converges to the optimum, no discontinuities should be visible moving from one case to the other.

The transformation estimated through the image registration procedure can be used to estimate two quantities: the *displacement vector field* and the *Jacobian* (J). The displacement vector field describes how each voxel moved from the reference to the test volume; it is retrieved from the transformation (e.g. Equation 2-18) once the identity is subtracted. The spatial derivative of the displacement field is the *strain tensor* and is related to the elastic properties of the material. The Jacobian instead represents the local expansion or contraction. A value lower than one corresponds to a contraction between the test and the moving object; a value greater than one to an expansion; values lower or equal to zero represent singularities and folding and should be avoided.

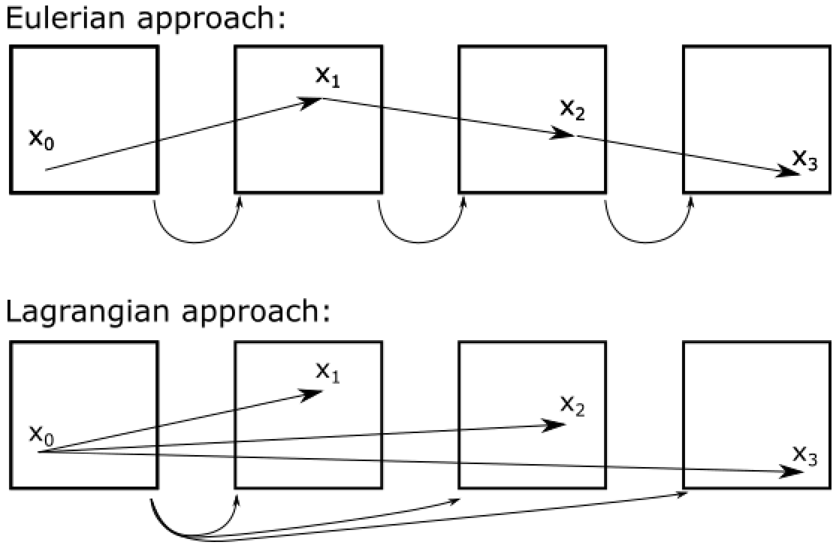

Figure 2-5 Representation of the Eulerian and Lagrangian approaches in image registration. In the Eulerian approach consecutive frames are compared; in the Lagrangian approach all the volumes are registered against a fixed reference frame.

In a dynamic CT, the displacement vector field and the Jacobian can be retrieved comparing two consecutive time frames or comparing each time frame with a fixed one, as in Figure 2-5. The first approach (Eulerian approach, following the fluid mechanics convention [89]), allows to compute local displacement and expansion at every phase; the second approach to follow in time the displacement and the expansion of a specific region of interest (Lagrangian approach). While the displacement between consecutive time frames is usually small, it can be large when comparing instants distant in time: this can lead to a wrong estimate of the transformation. A solution for the Lagrangian approach would be to concatenate the consecutive transformations of the Eulerian approach: a suitable regularization term would be required to smooth the transition between different phases; a second solution relies in registering all the volumes at the same time, using a 4D B-spline to estimate a smooth transformation in the time variable as discussed before.

3 EXPERIMENTAL SETUP

This Chapter describes the fundaments of synchrotron radiation, of the instrumentation and of the facilities built to generate and exploit it. The description will focus on the specific case of the European Synchrotron Radiation Facility (ESRF) and of the biomedical beamline (ID17), where all the experiments were performed. An overview of the tomographic setup available at the beamline, in particular for *in-vivo* applications, will be given.

3.1 INTRODUCTION TO SYNCHROTRON RADIATION

Synchrotron radiation is the electromagnetic radiation emitted by relativistic charged particles when accelerated; it was first observed in 1947 at the 70 MeV General Electric electron synchrotron [99]. Although initially seen as pure energy loss in particle accelerators, its unique characteristics in terms of broad spectrum, brightness, polarization and coherence lead to the construction of dedicated facilities utilized for research in numerous fields, from solid state physics to biology and medicine. Since the late 60's, with the construction of the first generation of dedicated synchrotron radiation machines, the technical advancements and the increase of intensity of produced radiation has been identified with three generations of machines.

A third-generation synchrotron radiation facility consists in general of three sections: an electron source and linear accelerator (*LINAC*), a *booster* and a *storage ring*. Electrons are emitted by an electron gun, typically a hot filament (cathode), via thermoionic emission. They are accelerated in the LINAC until they reach an energy of the order of 100-200 MeV and then injected in a booster. The booster is a multi-segment particle accelerator, properly defined as synchrotron, where the electrons are accelerated until they reach the maximal energy at which the facility operates, typically between 1.5 and 8 GeV. From the booster the electrons are injected into the storage ring, in which the electrons are kept on a stable closed orbit using a periodic sequence of magnets, called the *magnetic lattice*. The first component of the magnetic lattice is a magnetic dipole. It accelerates the electrons radially, bending the electron beam and forcing it into a closed orbit. Electrons with different positions inside the beam will however follow different circular orbits: in order to focus the beam, quadrupoles and sextupoles are placed in straight sections in between dipoles. Quadrupoles focus in one of the two directions orthogonal to the direction of propagation of the beam, and defocus in the other. For this reason, a sequence of quadrupoles with alternating polarities is needed to achieve a global focusing action. Sextupoles are used to correct for chromatic aberrations produced by quadrupoles.

Synchrotron radiation is produced when the electrons are accelerated in a magnetic field. In a storage ring there are three sources of synchrotron radiation: bending magnets, wigglers and undulators. Bending magnets are the aforementioned magnetic dipoles. Electrons are accelerated radially by the Lorentz force, typically in the horizontal plane, and emit radiation. Using the relativistic Lorentz transform it is possible to show that the radiation is emitted in a small cone, tangential to the circular trajectory of the electron beam. The aperture of the cone is of the order of $2/\gamma$ where γ is the relativistic parameter $\gamma = 1/\sqrt{(1-\beta_r^2)}$ and β_r the ratio between the speed of the electron and the speed of light in vacuum: c. γ is related to the energy E_e of the electron by the well-known relation $E_e = m_e \gamma c^2$ where m_e is the mass of the electron. Since the electron beam emits radiation along the whole arc of circumference described, the radiation beam will have the size $2/\gamma$ only in the vertical direction (orthogonal to the plane of the orbit); in the horizontal direction its size will be larger and dependent on the length of the arc described. A beam produced by a bending magnet is commonly described as *fan beam* or *laminar beam*. The power P emitted by an electron beam accelerated along an arc of circumference is proportional to the magnetic field of the dipole (B), to the electron energy (E_e), to the length of the arc (L_a) and to the electron current inside the storage ring (I_e):

$$P \propto E_e^2 \cdot B^2 \cdot L_a \cdot I_e \qquad 3\text{-}1$$

We define critical energy E_c of the radiation emitted by a dipole, the energy which divides the power spectrum in two identical parts. Wigglers and undulators are instead multipoles. They consist of 2N magnets with alternating polarity. Electrons, in their periodic magnetic field, wiggle, completing 2N oscillations in alternating directions. In the case of wigglers, the oscillations are wider than the aperture of the radiation cone: as a result, the radiation cones produced by the oscillations will be summed incoherently and the properties of the radiation will be similar to the one of a bending magnet. Instead, in undulators, the radiation emitted by one set of magnets will interfere with that emitted by the following ones, thus producing a narrow beam, with a characteristic spectrum consisting of a fundamental energy and on a series of higher harmonics.

In the storage ring the energy of the electron decreases at each revolution due to the emission of electromagnetic radiation. To compensate for this loss a set of radiofrequency RF cavities is used, which are accelerators based on an oscillating electric field. Emission of radiation and interactions between electrons in a single bunch will cause moreover a continuous loss of electrons from the beam and a decrease in the storage ring current. For this reason, electrons are periodically injected in the storage ring. At the ESRF the top-up injection mode was progressively introduced during the three years covered by this Thesis. In the top-up mode the injection is performed every 20 minutes resulting in a nearly constant beam current, which is a very important factor during long acquisitions.

3.1.1 Properties of synchrotron radiation important in *in-vivo* ct imaging

In Section 2.4.2 the importance of synchrotron radiation in *in-vivo* lung imaging was introduced. Here the main peculiarities of synchrotron radiation with respect to conventional X-ray sources, relevant in the case of *in-vivo* computed tomography, will be reviewed.

- **Brightness**: It is defined as the number of photons emitted per unit time in a spectral bandwidth $\Delta\lambda/\lambda = 0.1\%$, normalized to the source size and divergence, where λ is the wavelength of the radiation. It is a function of the photon energy. The high brightness of synchrotron radiation allows for fast image acquisitions at small pixel sizes, necessary for high spatial and time resolution. It is typically more than ten orders of magnitude larger than the peak brightness of an X-ray source (the value depends on the specific characteristics of the source). The brightness, coupled with the broad energy spectrum of bending magnets and wigglers, allows to extract intense monochromatic beams thanks to crystal systems.
- **Spatial (Transverse) Coherence:** A complete description of coherence is out of the scope of this Thesis, and can be found in specialized books [60]. The spatial coherence length is defined as $L_T = \lambda L/2s$ where L is the source to sample distance and s is the source size. It describes the length, perpendicular to the direction of propagation of the wave, after which the phase of the wave has changed of π. Coherence is usually linked to the ability of the

wave to produce interference fringes. In *in-vivo* CT imaging it is important when propagation-based phase contrast imaging is used, which was described in Chapter 2.

- **Divergence**: As previously described, the radiation is naturally collimated into a cone of aperture $2\gamma^{-1}$ in undulators, and this value is typically increased by one order of magnitude in the horizontal direction in wigglers and bending magnets. The laminar shape of the beam and the collimation are important in the geometry of CT acquisition. The small source size and the long propagation distances available in tomography beamlines, allow to consider the X-ray beam as a parallel beam. The collimation of the beam, when used together with a laminar detector, contributes moreover to the scattering rejection from images.

Another property of SR radiation, which is up to now not used *in-vivo* CT imaging is the **polarization** of the beam. SR radiation is linearly polarized along the orbit plane.

3.2 THE EUROPEAN SYNCHROTRON RADIATION FACILITY (ESRF) AND THE ID17 BEAMLINE

The European Synchrotron Radiation Facility (ESRF) is a third-generation synchrotron facility located in Grenoble (France). It started its operation in 1994, built from the collaboration of 11 countries, to reach in 2014 the number of 21 European and extra-European funding state members. Before the shutdown, started in December 2018 as part of the Extreme Brilliant Source project, it had 44 beamlines active along an 844 meters long storage ring. It operated at an electron energy of 6 GeV, reached in a 300 meters long booster.

ID17 is the biomedical beamline and is one of the few long beamlines of the ESRF, reaching a maximum source-to-detector distance of approximately 160 m. It is adapted to perform experiments covering a wide variety of applications in the biomedical field. Among the principal applications we find the preclinical investigation of radiation therapy with micro-beams (MRT) [100], neuroimaging [101], lung imaging [14], [102], and imaging of cartilage [103]. A general description of the beamline can be found in Elleaume et al. [104]; in the following the most relevant components will be reviewed.

3.2.1 ID17: X-ray source and general structure

The ID17 source consists of two multipole wigglers, with adjustable vertical gap between magnets. The first is a 21-pole wiggler (W150), with a period of 15 cm, and a maximum magnetic field of 1.6 T corresponding to a maximum critical energy of $E_c = 38$ keV. A second wiggler (W125) is used to increase the flux during the most demanding experiments. It is a 22-pole wiggler with a period of 12.5 cm and a maximum magnetic field of 1.8 T. For general imaging purposes, only the first wiggler is used at gap 60 mm corresponding to a magnetic field of 0.6 T and a critical energy of 15 keV [105]; in this conditions the source size, defined as the full width half maximum of the Gaussian profile of the electron beam, is $132 \times 24\ \mu\text{m}^2$ (H×V) [105]. When higher fluxes are required, especially when going towards higher resolutions, lower gaps are used. The magnetic field follows a trend which can be approximated by:

$$B = 2.78e^{-0.025g} + 0.84e^{-0.075g} - 0.09e^{-0.08g} - 0.48e^{-0.16g}$$

which was determined experimentally; here g is the gap in millimeters.

The beamline consists of two optics hutches (denominated OH1 and OH2, respectively) and of two experimental stations located in their respective hutches (EH1 and EH2), as shown in Figure 3-1. The first station is inside the experimental hall of the synchrotron facility. It is used for applications requiring a high flux, in particular the preclinical study for micro-beam radiation therapy and imaging experiments with pink beam [106]. The second station is in a satellite building, connected to the experimental hall by a 100 m long tube, held under ultra-high vacuum ($\sim 10^{-6}$ Pa). It is used when larger fields of view or higher spatial coherence are required; it is used moreover by the largest part of imaging experiments, since, just upstream to the experimental station, different monochromators can be used to select the most suitable energy for the experiments, as it will be explained later on in this section. The two experimental stations are in series and can't be used simultaneously: a tube under vacuum is in fact installed in the first experimental hutch, when the second one is used, so that the radiation propagates in vacuum from the source to the second optics hutch in the satellite building.

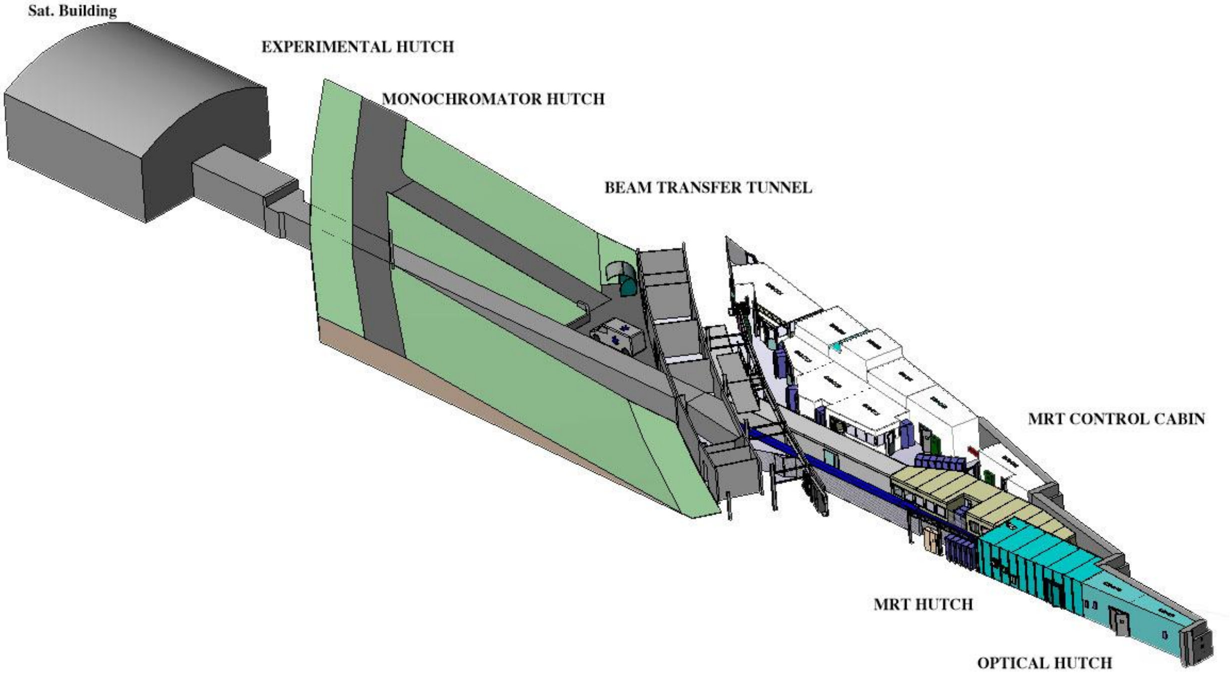

Figure 3-1 Schematic representation of the ID17 beamline at the ESRF. The main components are: the optical hutch (OH1), the MRT hutch (EH1), the monochromator hutch (OH2) and the experimental hutch (EH2). From (www.esrf.eu).

Together with the second experimental station, the satellite building hosts an animal facility, essential for biomedical applications; this laboratory is made to house animals, utilized in biomedical research and includes a surgery room where the samples are prepared for the imaging and radiotherapy experiments.

	Thickness (mm)	
	OH1	**OH2**
C	1.15	4.0, 0.8
Al	0.54, 0.71, 1.24	0.5, 1.0, 2.0
Cu	0.35, 0.69, 1.04	1.0

Table 3-1 List of main movable attenuators available at the ID17 beamline, used during imaging in OH1 and OH2 respectively. A more exhaustive list can be found in Mittone et al. [106].

3.2.2 ID17: technical description of the first experimental station (pink beam imaging)

The first part of the beamline is composed by an optics hutch and an experimental hutch. The optics hutch hosts the primary slits, used to define the size of the beam and two sets of water-cooled attenuators. Different movable attenuators are available, which allow to modulate the intensity and effective energy of the pink beam. With pink beam we refer to the polychromatic beam filtered by the attenuators and the beryllium windows, separating different vacuum sections and/or vacuum from air. There are four beryllium windows before the sample position, adding up to a total thickness of 2.3 mm. A list of the movable attenuators is available in Table 3-1; a complete list, including also the fixed attenuators can be found in Requardt et al. [107]. An example of spectrum obtained with different combinations of the attenuators is reported in Figure 3-2.

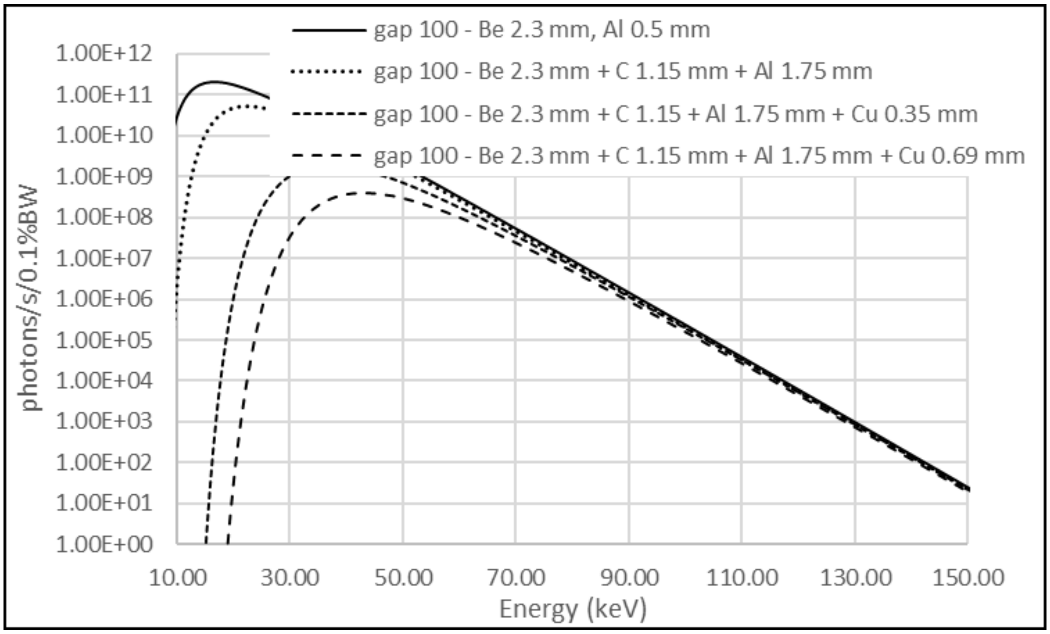

Figure 3-2 Spectrum emitted by the first wiggler (W150) at 100 mm opening gap modulated by different combinations of absorbers. The spectral flux is here defined as the number of photons at the sample position per unit time and surface in a spectral bandwidth $\Delta\lambda/\lambda = 0.1\%$. *Image taken from Mittone et al.* [106].

The first experimental hutch starts at about 30 m from the source [104]. It was built to host instrumentation for the Microbeam Radiation Therapy experiments, as described in detail in

Bräuer-Krisch et al. [100], Martinez-Rovira et al. [108] and references herein. During the three years covered by the project, the hutch was upgraded with the installation of a multiscale pink beam imaging setup [106]. It consists in two sCMOS (scientific Complementary metal–oxide–semiconductor) PCO edge 5.5 cameras, coupled with indirect conversion optics, with lenses that can be alternatively switched, giving an effective pixel size of 3.5, 1.4 and 0.7 µm. A more detailed description of the detectors will be given in Section 3.3.1 and can be found in previous papers [106], [109]. In the experiments described in Chapter 5, we used the effective pixel sizes of 0.7 µm and 3.5 µm. An automatic procedure was implemented to switch from the lower to the higher resolution, with the possibility to select a region of interest from the low-resolution scan.

3.2.3 ID17: technical description of the second experimental station (monochromatic imaging)

The second optics hutch, or monochromator hutch, is the first hutch of the satellite building. It contains a second set of filters (Table 3-1) and the secondary slits, to respectively tune the intensity and size of the white beam impinging on the monochromators. There are four monochromators available, all installed in vacuum chambers: (i) a double bent-Laue Si(111) monochromator, (ii) a double multilayer crystal, (iii) a double Si(111) flat crystal used in Bragg geometry and (iv) a single bent-Laue Si(111) monochromator.

The monochromator used in all the tomographic experiments is the double bent-Laue crystal [104], [110]. It is a fixed-exit monochromator: the outgoing beam is parallel to the incoming one with a vertical offset of 40 mm for any energy chosen in the working range of the instrument. It consists of two Si(111) cylindrically bent asymmetric crystals, with an asymmetry angle of 15º and a thickness of 1 mm. The advantages of a bent crystal in Laue geometry (with respect to the more standard Bragg geometry) for this energy range are multiple (see Figure 3-3): a) the width of the reflectivity curve can be tuned acting on the radius of curvature, thus increasing the flux available at the sample position and also improving the stability of the beam; b) the length of the crystals are much reduced (edge-on geometry instead of a grazing geometry). The monochromator can produce a stable monochromatic beam in the range 25 keV – 150 keV, with a bandwidth of 0.1% [110] and a maximum size of 150 mm $\times$ 10 mm.

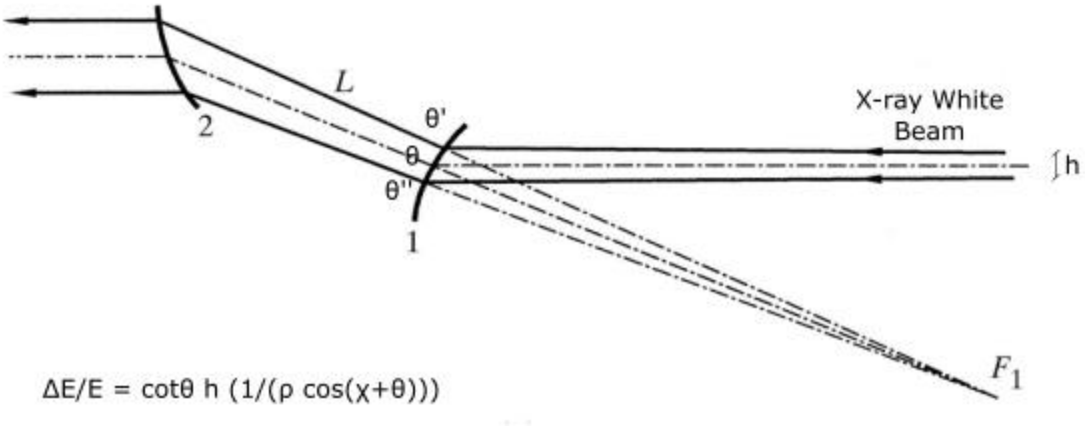

Figure 3-3 Scheme of a fixed exit double bent Laue monochromator. The white beam impinges on the first crystal (1); due to the curvature, the diffraction angle θ changes along the beam height h, producing a widening of the reflectivity curve and a vertical energy gradient $\Delta E/E$. The width of the reflectivity curve can be tuned acting on the radius of curvature. Adapted from Suortti et al. [111].

The optics hutch contains a high load rotation stage, used for tomographic experiments, and a system of beam shutters which can stop the irradiation in the second experimental hutch, avoiding unnecessary exposure of biological samples and of the cameras.

The second experimental hutch is placed at 150 m from the source and is the hutch where most of the tomographic experiments are performed. The setup used in *in-vivo* tomography will be described in the following paragraph and is the same used in the first experimental hutch.

3.3 *IN-VIVO* TOMOGRAPHY SETUP

3.3.1 Detector system

For *in-vivo* imaging, the most stringent requirement is to acquire the projections fast, in order to neglect motion during the detector integration time. Two fast PCO Edge 5.5 cameras, differing only for their cooling system, are available for this purpose at the beamline. One of the two is air cooled, the second one is water cooled and is operated at 5° C. They have a 2560 × 2180 sCMOS image sensor (Fairchild Semiconductor, Sunnyvale, California, US), with a physical pixel size of 6.5 µm, corresponding to an active area of (16.6 × 14.2) mm^2. They are characterized by a 16 bit dynamic range and can be operated in three modalities:

- Global Shutter: in this modality all the pixels are exposed simultaneously. Every time an image is acquired all the pixels are reset and one image is automatically stored (dark image) for noise subtraction. This modality is characterized by a high signal to noise ratio but a reduced frame rate, which is one half of the maximum.
- Rolling Shutter: in this modality the pixel reset and start are performed row by row. This means that different rows are exposed during different time intervals, starting from the outside towards the center. This is the fastest imaging modality but can introduce distortions in the image for moving objects. The time shift between rows is 10 µs, which results in a maximum delay negligible for our study, as will be discussed in the next chapters. This modality is the one used in all the experiments, due to the fast frame rate achieved.
- Global Reset: in this modality the start of the exposure is sent simultaneously to all pixels, but the stop is carried out row by row. The exposure time differs therefore from the outside to the center. This modality was not used.

The maximum frame rate in rolling shutter mode is 100 fps at full frame rate. To increase it, a reduction of the field of view has to be performed. A value of 800 fps can be reached for example with a field of view of 2560 × 256 pixels. The camera is connected to the ESRF central storage server through a 10 Gb network. It is important to underline that the maximum frame rate achievable depends on the speed of the camera as well as on the speed with which data are transferred and saved on the ESRF server.

3.3.2 Optics and scintillators

The detectors are coupled to a system of scintillators and optical lenses. Several scintillators are used at ID17: the material and thickness are chosen as the best compromise between detection efficiency and spatial resolution. Among them, the powder phosphors screens were used for the experiments reported in this Thesis work: Ce:YAG (YAG), $Tb:Gd_2O_2S$ (Gadox) and Ce:LuAG (LUAG) [109]. Different systems of lenses are used in the two experimental hutches: the effective pixel size used in this work are 3.5 µm and 0.7 µm with the pink beam imaging setup (EH1); 3.1 µm, 6.2 µm, 11 µm and 22.3 µm with the monochromatic setup (EH2). The effective pixel size on the image depends on the experimental setup and on the distance between sample and detector, due to the divergence of the beam, and it will be specified for every experiment.

3.3.3 Translation and rotation stages

For tomographic acquisitions two setups are available. One tomographic setup is mounted in the second optics hutch, after the monochromators, and is fixed. It is a high load rotation stage, referred to as *paleostage*, with maximum speed of rotation of 6 rpm and an angular precision of 0.02º [112].

The second setup is instead moved between the first and the second experimental hutch, depending on the application required. It is based on a tower of motors, whose specifications can be found in Mittone et al. [106] and which are shown in Figure 3-4:

- Horizontal and vertical translation: to position the sample in the laminar beam.
- Tilt axis: to align the plane of rotation and the camera.
- Rotation: an air bearing rotary stage RT150s from Lab Motion System. Maximum speed 200 rpm, angular accuracy: 0.002º.
- Precise horizontal translation: for the fine positioning the sample inside the field of view.

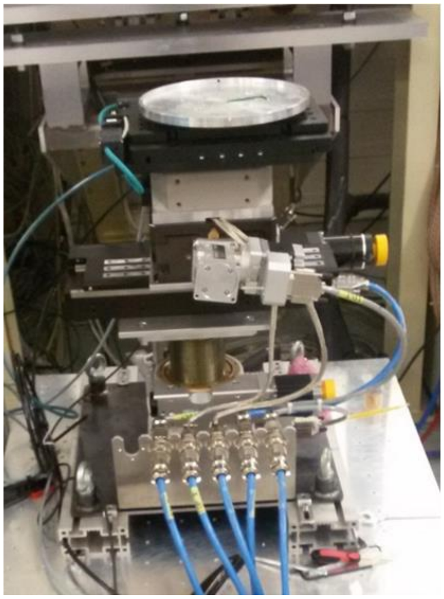

Figure 3-4 Movable tomography setup at ID17. It consists (bottom to top) of a vertical and a horizontal stage for sample positioning, a tilt axis, an air bearing rotary stage and a precise horizontal translation for fine alignment. Adapted from Mittone et al. [106].

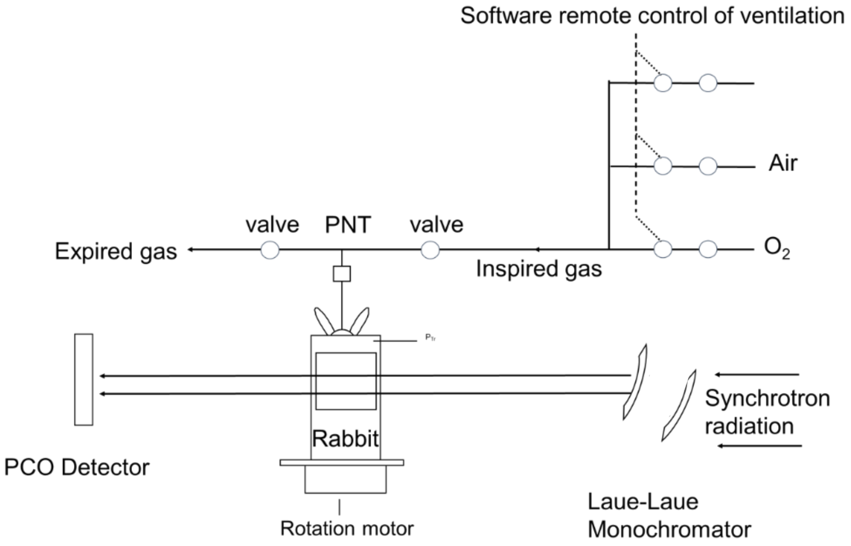

Figure 3-5 Scheme of the experimental setup for a conventional in-vivo lung imaging experiment. The animal is immobilized in a plastic holder and placed on the rotation stage. In this figure the custom-made mechanical ventilator available at ID17 is shown. It consists of (i) an inspiratory branch connected to oxygen and air bottles, which allow to control the flow and the fraction of inspired oxygen, and (ii) of an expiratory branch. Inspiration and expiration are remotely controlled through electromagnetic valves. Airflow is measured using a pneumotachometer (PNT).

3.3.4 Physiological instrumentation

Before *in-vivo* imaging experiments, animals were prepared in the animal facility, located in the ID17 premises (Section 3.2.1). Surgery and animal preparation will be discussed in detail in specific sections in Chapter 4 and 5. For *in-vivo* lung imaging the surgery typically consisted in a tracheostomy with the insertion of a catheter in the trachea, which allowed to connect the animal to a mechanical ventilation system. In our experiments we used either a commercial or a custom-made mechanical ventilator. The commercial one was a Flexivent (SCIREQ, Montreal, Canada) used for small animal models, in particular rats. For bigger animal models, such as rabbits, a custom made ventilator was used instead [79], [113] (see Figure 3-5). It consisted in a T-tube with an inspiratory and expiratory branch, connected to the catheter inserted in the trachea of the animal. The inspiratory branch was supplied by air and oxygen bottles, to control the fraction of inspired oxygen F_{IO_2} (see Section 1.1.3). The expiratory branch was connected to a column of water or to an adjustable positive pressure valve, to adjust the PEEP. The ventilator was remotely controlled, allowing to set the inspiratory and expiratory time, and gas flow. This was obtained by acting on an electromagnetic valve, placed on the expiratory branch: the valve was closed during inspiration and opened during expiration. The gas flow in the inspiratory branch, measured using a pneumotachometer (PNT) had to be adjusted manually. Therefore, no intervention was possible during imaging. The ECG signal, arterial pressure, airway pressure at the trachea (tracheal pressure, P_{TRACH}) and flow at the trachea were recorded using a Powerlab 16/35 data acquisition device (DAQ, Adinstruments, Dunedin, New Zealand) coupled with a Bio Amp and Bridge Amps modules (Adinstruments, Dunedin, New Zealand). The signals were sampled at 10 kHz. The experimental setup, in particular at the level of the ventilator, was optimized at every experiment, if non-standard respiratory maneuvers were to be tested. The most relevant variations of this description, when used, will be reported in the respective chapter.

4 IN-VIVO 3D MICROSCOPY: A STUDY OF ATELECTRAUMA IN AN EARLY STAGE OF VILI

4.1 INTRODUCTION

In Chapter 1 the injurious effects of positive pressure mechanical ventilation, due to excessive stress on the lung tissue, and the concept of Ventilator Induced Lung Injury were introduced. The main sources of mechanical stress, i.e. overdistension and atelectrauma, were discussed. Although the role of excessive stress and strain to the lung by positive-pressure ventilation is well established, the link between the mechanical stresses induced to the lung tissue through atelectrauma and the inflammatory response at an early stage of VILI is not understood.

In Chapter 2 an overview of *in-vivo* phase-contrast 3D lung microscopy techniques was given. These techniques, based on the assumption of repetitive, ideally periodic, lung tissue motion, were successfully applied to the study of dynamic phenomena, such as airflow, cardiogenic lung tissue motion, and local tissue expansion, at high resolution (20 µm) in an *in-vivo* small animal model. The dynamic and periodic nature of the atelectrauma, which is the repetitive opening and closing of lung units at every breath (see Section 1.2.2), suggests *in-vivo* 3D microscopy as the appropriate investigative tool.

The main experimental limitation of the existing *in-vivo* microscopy techniques is that the motion of the lung parenchyma, induced by the heart and by the mechanical ventilator (Section 2.3.2), cannot be fully resolved: only one of the two sources of parenchymal motion is gated. When the heartbeat is gated, the mechanical ventilation is stopped to obtain a constant pressure; when the ventilation is gated, the acquisition is not synchronized with the heart, inducing motion artefacts in the ventral region. To study atelectrauma in dynamic conditions at high resolution, a new imaging protocol must therefore be developed.

For this purpose, two image acquisition protocols were designed in the present study. In a preliminary phase the cardiac motion was isolated, inducing a respiratory pause, or apnea; once this first protocol was established, mechanical ventilation was reintroduced. These two protocols were capable of resolving respectively the cardiogenic motion and the cardiogenic motion combined with the mechanical ventilation, with a pixel size of 20 µm. They were applied *in-vivo* to an adult rabbit model of VILI. The first protocol allowed to quantify the cardiogenic motion of the lung parenchyma in healthy conditions and in the VILI model. The second protocol allowed to visualize and quantify atelectrauma, in an initial stage of VILI and to study its regional relationship to lung inflammation through histological analysis. Atelectrauma was measured dynamically during the breathing cycle and not comparing respiratory pauses during inspiration and expiration, the latter being the most diffused approach in the literature. To my knowledge this is the first time that VILI is studied in dynamic conditions at such a high resolution in an animal model.

4.2 METHODS

4.2.1 *In-vivo* dynamic 3D lung microscopy: two novel acquisition protocols

The two acquisition protocols proposed in this work belong to the class of the retrospective gated techniques introduced in Section 2.3.1. Retrospective gating allows to acquire several phases of the motion under study during a single scan; it is therefore the most suited technique to study the lung parenchymal dynamics.

There are two main requirements in retrospective gating: (i) the motion under study must be periodic; (ii) there is a physiological signal (α) from which the phase of the periodic motion can be extrapolated. The complexity of the lung motion was introduced in section 2.3.2. The two acquisition protocols proposed in this study, during apnea and mechanical ventilation, differ for the solutions adopted to meet the two aforementioned requirements; these solutions will be the subjects of the next paragraphs (4.2.1.1 and 4.2.1.2). Once the lung parenchymal motion was periodic, and the physiological signal describing it was defined, the acquisition logic represented in Figure 4-1 was adopted.

A complete CT was acquired during a single slow rotation of the sample, covering an angular range of 2π. This value was associated to the half acquisition technique described in Section 2.2.2, which allows to almost double the field of view of the camera for large samples. If the motion is periodic, the number of projections θ acquired per phase ϕ is equal to the number of periods covered by the rotation. The duration of the scan was determined therefore by the period of the motion and by the number of projections required for the CT reconstruction. The number of projections was a compromise between the desired image quality and the dose delivered to the sample. Projections were acquired at a fixed frame rate, which, together with the integration time, determines the maximum time resolution of the scan (Section 2.3.1).

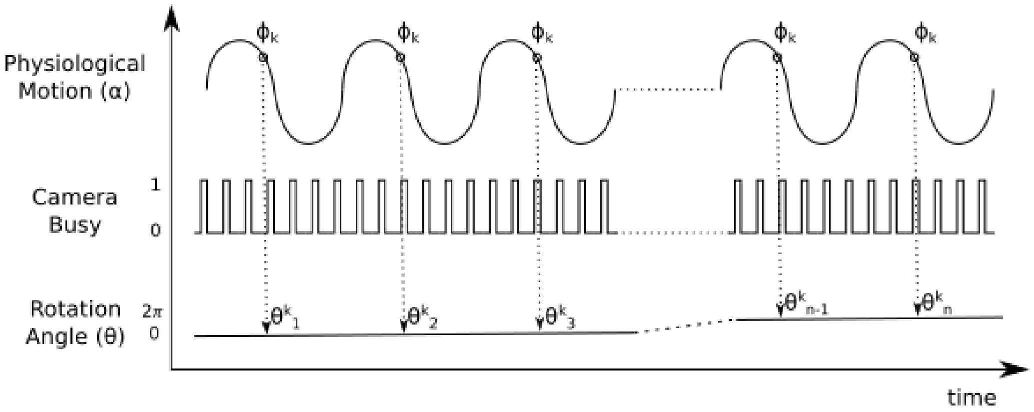

Figure 4-1 General acquisition protocol for the retrospective gated approaches proposed, in the case of a periodic lung parenchymal motion described by a variable α (e.g. ECG or tracheal pressure). n periods of the motion are acquired during a single slow 2π rotation, while the camera acquires at a constant frame rate. A generic phase of the motion ϕ_k is acquired at n different angles in the range (0, 2π), with a time resolution given by the reciprocal of the frame rate plus the acquisition time of a single projection.

If high time resolution is required, a short integration time has to be selected: a short integration time and a small number of projections lead to a decrease in the signal to noise ratio and to under-sampling artefacts.

4.2.1.1 Acquisition protocol during a respiratory pause

As previously stated, the goal of the project was to develop a technique capable of resolving the combined motion of the lung parenchyma induced by the heart and the mechanical ventilator. Due to complexity of the motion, as a preliminary step, it was decided to remove the contribution of the mechanical ventilation, inducing a respiratory pause and therefore a constant airway pressure, during imaging. If a simple breath hold is induced however, stable hemodynamic conditions cannot be assured, and the condition on periodic lung parenchymal motion cannot be met. A breath hold produces in fact a decrease in the alveolar P_{O_2}, causing an initial acceleration of the heart, to compensate for the loss of oxygen, followed by a deceleration. At the same time oxygen absorption by the blood reduces the alveolar pressure, leading to a slow collapse of lung units. To reduce these instabilities, the apneic oxygenation method was used. Apneic oxygenation consists in maintaining a high flow of pure oxygen at the trachea. Oxygen diffuses into the alveoli, balancing the reduction in alveolar P_{O_2} and keeping stable hemodynamic conditions for several minutes. Despite the oxygenation however CO_2 is not removed from the lungs and its partial pressure in the blood increases.

Figure 4-2 represents the specific acquisition scheme in apnea. The physiological signal acquired to describe the phase of the heart motion is the ECG, even if other signals could be related to the heart activity, for example the arterial pressure. The phase of the motion is here defined as the absolute delay from the R peak, as in previous works [13], [82], [83]. It is important to underline that the imaging acquisition does not start immediately after the beginning of the breath hold, but an empirical delay of approximately 30 s is allowed, to let the lung stabilize after the transitional phase from ventilation to apnea. By acquiring a fast sequence of projections at a fixed rotation angle, lung instabilities were in fact observed in the rabbit model at the beginning of apnea even a few seconds after the required pressure was reached.

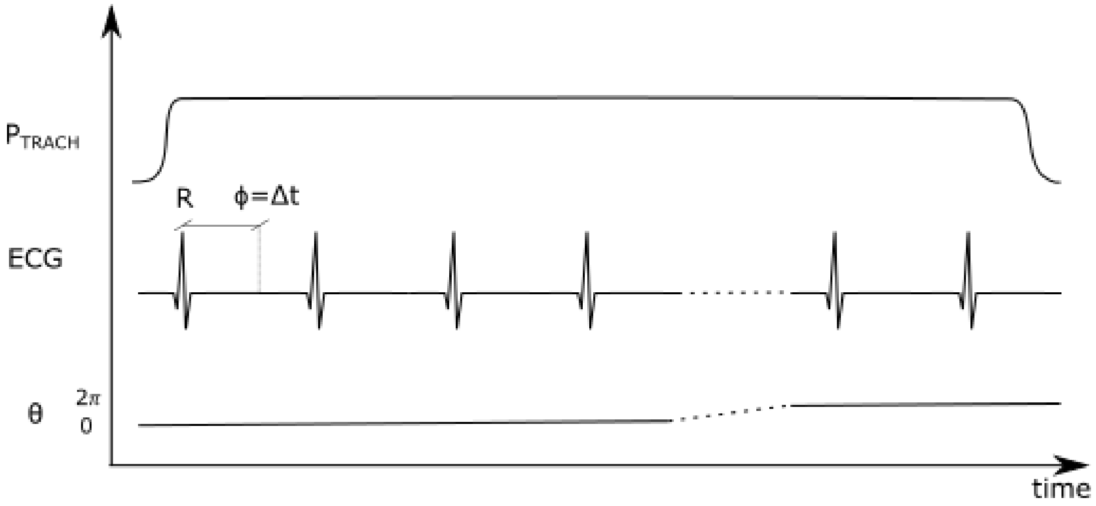

Figure 4-2 Scheme of the dynamic CT in apnea. Several cardiac cycles are acquired over a single 2π rotation (θ). The R peak of the ECG is used as a reference to identify the phase of the periodic motion. The phase (ϕ) can be defined as the delay from the R peak.

4.2.1.2 Acquisition protocol during mechanical ventilation

Once the imaging protocol based on the respiratory pause was established and successfully tested, mechanical ventilation was reintroduced. Mechanical ventilation can be described using the airway pressure as a physiological signal represented in this work by the tracheal pressure. As previously stated, the acquisition scheme is based on obtaining the best approximation of a periodic motion of the lung parenchyma. In this situation there are two sources of motion, which influence each other, but are not synchronized: heart and mechanical ventilator. In order to synchronize them the scheme represented in Figure 4-3 was adopted.

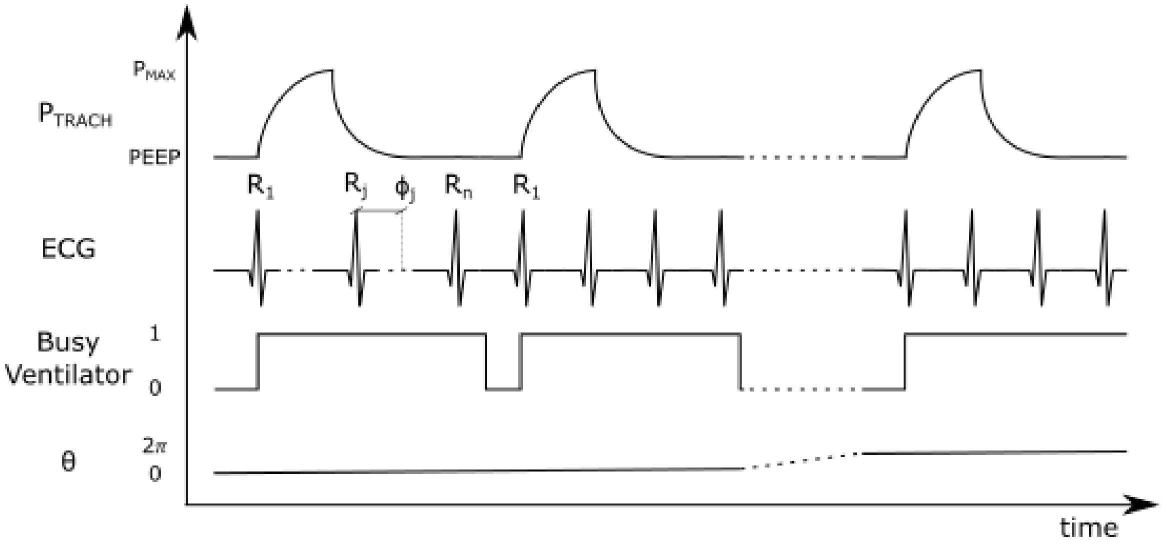

Figure 4-3 Scheme of the dynamic CT with mechanical ventilation. A respiratory cycle is triggered by the R peak of the ECG. A busy signal is immediately raised (0 to 1), with user defined duration. When the busy signal is on (1) triggers are not accepted: only one R peak out of n (user defined) can trigger therefore the ventilator, assuring sufficient inspiratory-expiratory time. Several periods of the combined periodic motion are acquired over a single 2π rotation (θ). The R peak of the ECG is used as a reference to identify the phase of the periodic motion. The phase (ϕ_j) can be defined as the delay from the j-th R peak of the respiratory cycle.

The synchronization between heartbeat and mechanical ventilation was obtained triggering every inspiratory-expiratory cycle with the ECG, in particular when the R peak was detected. The period of the heart, in the rabbit model used in this study, is however usually too short to obtain a sufficient ventilation. A common respiratory rate in rabbits is of approximately 30 breaths per minute (bpm), compared to a heart rate of 180 beats per minute, implying that there will be five or six heart beats per respiratory cycle. In our simple implementation, a busy signal of the ventilator is raised as soon as the inspiration begins. When the busy signal is on, no triggers are accepted. The duration of the busy signal must be chosen carefully: it must be long enough to assure a sufficient expiratory time, or a pressure build up will occur, due to incomplete expiration. As soon as the busy signal is lowered a polling on the ECG signal begins, and the new respiratory cycle is started when the next R peak is detected. If the heart rate is stable, the motion of the lung parenchyma will be approximately periodic, and its phase will be fully determined by the ECG through two parameters, as shown in Figure 4-3: the distance from the j-th R peak ($\Phi_j = \Delta t_j$) and the j index itself, denoting which of the n heart pulsations included in the respiratory cycle is considered. As in the previous case, a full rotation was performed during N periods of the combined periodic motion, where N is the required number of projections per CT.

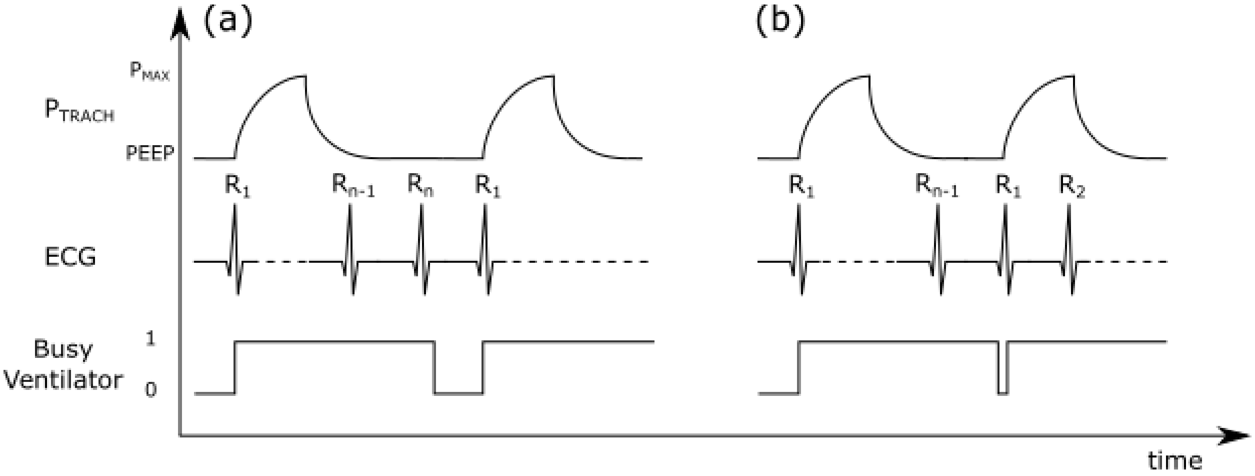

Figure 4-4 Instability associated to a variable ECG period in the dynamic CT scan, when the duration of the busy signal is a multiple of the ECG period. In (a) the n-th R wave occurs just before the end of the busy signal. In (b) it occurs just after, triggering a new ventilator cycle and becoming R_1. A small variation in the heart frequency can cause an oscillation from (a) to (b), varying the expiratory time, the number of heart cycles per respiratory cycle, and possibly the PEEP level.

The main instability related to this scheme is that the duration of the heart cycle could in general vary in time. Let’s consider the situation represented in Figure 4-4, where the duration of the busy signal of the ventilator is approximately a multiple of the ECG period. If the heart rate decreases, an R wave occurring just before the falling edge of the busy signal could start occurring after it, triggering the next respiratory cycle. This situation would have two consequences: (i) the number of heart cycles per ventilatory cycle would change; (ii) the expiratory time would vary of approximately one heart period, possibly modifying the PEEP level. If this situation occurs the scan must be discarded. To reduce instabilities, the synchronization between the ventilator and the heart is started a couple of minutes before the acquisition, to let the heart rate stabilize; just before the acquisition, the duration of the busy signal is optimized, not to be a multiple of the heart rate. In general, the heartbeat will be more stable than in the case of the apneic oxygenation, since sufficient ventilation is provided for the whole duration of the scan. The period of the combined motion of the lung parenchyma will be however longer than in the case of a pure cardiogenic motion, producing a significant increase in the radiation dose delivered to the sample.

The two imaging protocols described in this section were applied to a rabbit model of VILI, in order to study the lung mechanics in injured conditions and to visualize the atelectrauma at high resolution (20 µm). In the next sections the implementation of the two acquisition protocols, of the phase detection for the retrospective gating, as well as the injury model will be presented.

4.2.2 Experimental setup and dosimetry

The two imaging protocols were developed, tested and applied to VILI in the second experimental hutch EH2, in the satellite building of ID17 (Section 3.2.1 and 3.2.3). The movable tomographic setup described in Section 3.3.3 (Figure 3-4) was utilized, setting a sample to detector distance to approximately 1.5 m. The PCO camera was coupled with a 50 µm thick Gadox scintillator and optics giving a measured effective pixel size of approximately 22.6 µm. The camera was operated in rolling shutter mode and the field of view was reduced to 2560 × 200 pixels (57.9 × 4.5 mm^2) to achieve high frame rates. When the experiment was performed, the saving procedure in the ESRF central storage server was still not optimized, and the maximum frame rate achievable was limited to 130 fps. Higher frame rates would have led to an error in saving the projections and to an incomplete tomographic acquisition. The CT was acquired using a monochromatic beam set at 52 keV using the double Laue monochromator (Section 3.2.3 and Figure 3-3).

The entrance dose delivered to the animal was estimated using a Semiflex tube ionization chamber TW31010 (PTW, Freiburg, Germany) in-air associated to a UNIDOS Webline TW10022 electrometer (PTW, Freiburg, Germany). Camera and Electrometer were calibrated and certified by PTW-Freiburg. Due to the laminar beam, the ionization chamber was not fully irradiated during the measurement. A scanning technique was developed at the beamline to take this irradiation geometry into account; details can be found in Prezado et al. [114]. During the scan the two wigglers, W150 and W125, were set to a gap of 52 mm and 40 mm, respectively. The electron current in the ring was 200 mA. In these conditions, with a 7.5 mm high beam, the entrance dose rate was 113 $\mathrm{mGy} \cdot \mathrm{s}^{-1}$.

The experimental setup, concerning the rabbit handling and ventilation, is the one described in Chapter 3, Section 3.3.4. The custom-made mechanical ventilator, shown in Figure 3-5 was utilized for baseline ventilation. The implementation of the apneic oxygenation and of the synchronization with the heartbeat required a modification of the mechanical ventilator during imaging. The implementation of the two protocols and the modifications required will be the topic of the next section. The Powerlab system introduced in Section 3.3.4 was used to measure arterial pressure, ECG, airway pressure at the trachea and airflow at the trachea. Airway pressure and airflow were measured in the inspiratory branch at the level of the T tube connecting the mechanical ventilator to the catheter in the trachea of the animal (see Section 3.3.4 and 4.2.4 for more details concerning the animal preparation).

4.2.3 Implementation of the apneic oxygenation and synchronization of the mechanical ventilator with the heartbeat

In this section the implementation of the apneic oxygenation, for the imaging protocol in apnea, and of the synchronization between the mechanical ventilation and the ECG will be described.

To implement the apneic oxygenation, a specific ventilation circuit was designed, which is shown in Figure 4-5. It consisted in an inspiratory branch, directly connected to an oxygen gas bottle, and an expiratory branch ending with a resistance. The circuit was manually switched from mechanical ventilation to apneic oxygenation priori to imaging. Unlike the setup for baseline ventilation (Figure 3-5), no electromagnetic valves were present during imaging, therefore a constant flow of pure oxygen was maintained at the trachea. The constant oxygen flow inflated the lungs inducing, at equilibrium, a constant pressure, measured at the trachea. By modifying the resistance in the expiratory branch, it was possible to modify the airflow in the ventilation circuit and therefore the tracheal pressure.

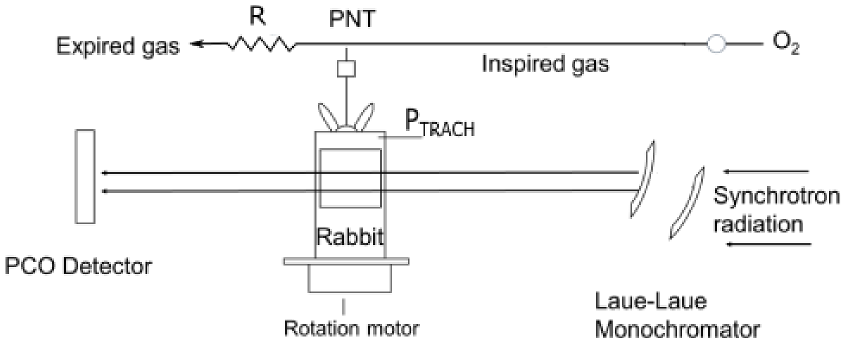

Figure 4-5 Scheme of the experimental setup for the apneic oxygenation (see Figure 3-5 for reference). A constant flux of pure oxygen is maintained at the trachea. No valve is present in the expiratory branch, which ends with a resistance R. By changing the value of the resistance, it is possible to modify the flux of oxygen at the trachea and the value of the constant pressure induced in the lungs.

To implement the synchronization between the ECG and the heartbeat, which was presented in Figure 4-3, the default respiratory circuit (Section 3.3.4) was utilized. The main difference consisted in the fact that the electromagnetic valves were controlled using the software Labchart (ADInstruments, Dunedin, New Zealand), as shown in Figure 4-6. Labchart is the software which allows to drive the Powerlab (ADInstruments, Dunedin, New Zealand) from a PC. Labchart allowed to monitor the ECG, detecting R waves based on a threshold on the ECG signal. When an R wave was detected a square wave was generated, with user defined duration and duty cycle. The square wave was transmitted via a TTL signal generated by the Powerlab to the electromagnetic valve in the expiratory branch, controlling its status (closed-opened) and therefore the inspiration/expiration time. The ECG polling was disabled for the whole duration of the square wave, concept equivalent to the busy signal of the mechanical ventilator described in Section 4.2.1.2.

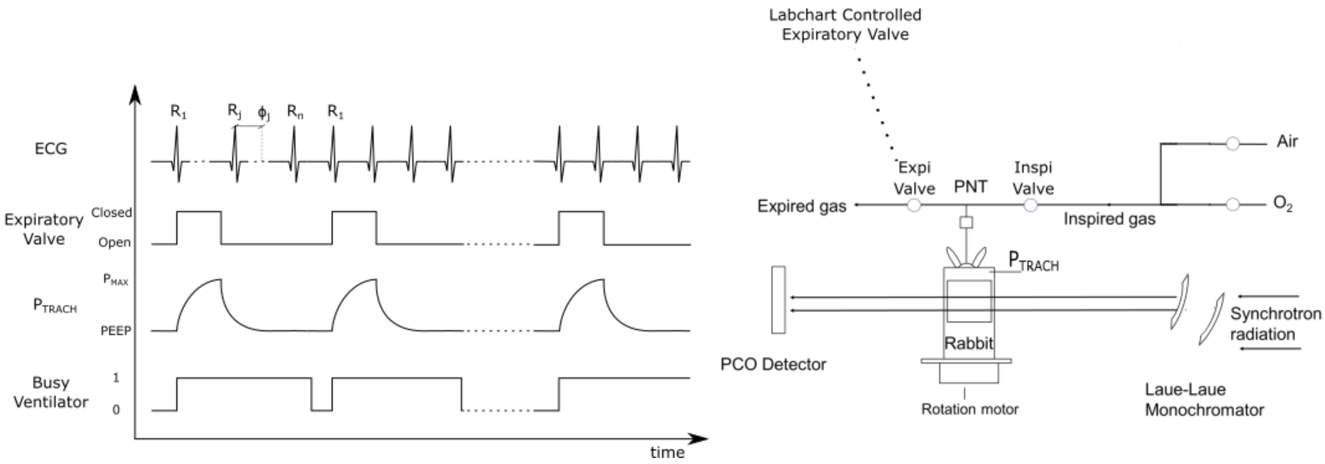

Figure 4-6 Synchronization of the mechanical ventilation with the heartbeat. The software Labchart is used to monitor the ECG. When an R wave is detected a square wave (TTL signal) is generated, with duration and duty cycle determined by the user and sent to the expiratory valve. A logical value of 1 closes the expiratory valve, determining lung inflation; the value 0 opens the expiratory valve. The polling on the ECG is disabled for the whole duration of the square wave, concept represented as the Busy of the mechanical ventilator. The sample is continuously irradiated during the scan. Associated to an injury model, this acquisition scheme allows to study the atelectrauma dynamically during a whole breathing cycle.

4.2.4 Animal preparation and injury model

The rabbits utilized in this study were anesthetized in the surgical room of the animal facility by intramuscular injection of Ketamine (10 to 15 mg/kg) (Ketamine 1000, Virbac, France) and Xylazine (3 to 6 mg/kg) (Paxman, Virbach, France). Surgery consisted in tracheostomy with the insertion of a 3.5-F plastic catheter in the trachea (Portex, Smiths Medical, Minneapolis, Minnesota, USA). A 24-G catheter (Venflon, BD, Franklin Lakes, New Jersey, USA) was placed on the central ear artery, to monitor blood pressure. After surgery the animal was immobilized in a custom-made plastic holder, for imaging, and taken to the experimental hutch. The anesthesia was maintained during the whole duration of the experiment with IV injection of Ketamine (80 mg/kg/h) (Ketamine 1000, Virbac, France) and Xylazine (8 mg/kg/h) (Paxman, Virbach, France). Atracurium (0.6mg/kg/h), a muscle relaxant, was administered IV to avoid motion and suppress spontaneous breathing. The physiological parameters monitored in the experimental hutch were ECG, tracheal pressure, arterial pressure and blood gas. The principal parameters studied with blood gas analysis were pH, Pa_{CO_2} (partial pressure of CO_2 in arterial blood), Pa_{O_2}, HCO_3. They were considered normal in the interval: 7.35 < pH < 7.50; 35 mmHg < Pa_{CO_2} < 45 mmHg; 18 < HCO_3^- < 28 mmol/L; $Pa_{O_2}/F_{I_{O_2}} > 300$ mmHg.

In the experimental hutch the rabbit was connected to the custom-made mechanical ventilator, through the plastic catheter. Mechanical ventilation was always performed with the animal in upright position. At baseline the animals were ventilated with a protective ventilation strategy, characterized by a tidal volume V_T = 5-6 ml/kg, $F_{I_{O_2}} = 0.5$ and a PEEP = 5 cmH_2O. pH and Pa_{CO_2} were used to adjust the minute ventilation and therefore the respiratory rate (Section 1.1.3).

The injury model consisted in surfactant depletion by whole lung lavage followed by injurious ventilation characterized by $F_{I_{O_2}} = 100\%$, PEEP=0 cmH_2O and a P_{MAX}=30 cmH_2O, inducing atelectrauma and overdistension (Section 1.2.2). The lavage was performed with the animal lying in supine position: 4 lavages were performed in series with 40 mL of saline solution. Mechanical ventilation was performed in pressure-controlled mode, obtaining a variable V_T, depending on the lung compliance. The development of the injury was monitored at regular intervals of 30 minutes, through chest tomography and blood gas analysis. For the blood gas test PEEP was temporarily set to 5cmH_2O. The injurious ventilation was stopped when the $Pa_{O_2}/F_{I_{O_2}}$ ratio was below 200 mmHg, which corresponds to moderate-acute lung injury according to the Berlin definition [2].

After injury a protective ventilation strategy was adopted; it was characterized by a V_T = 5-6 ml/kg, $F_{I_{O_2}} = 100\%$ and a PEEP = 5 cmH_2O. The respiratory rate was adjusted based on the values of pH and P_{aCO_2}.

At the end of the experiment the animal was euthanized by barbiturate overdose (IV injection of pentobarbital sodium 220 mg/kg).

4.2.5 Imaging protocol

The study was performed on five male New Zealand White Rabbits (Wt: 2.71±0.15 kg), hereafter denoted as Rabbit 1-5. An additional rabbit (Wt: 2.96 kg) was imaged as control and didn’t undergo injurious ventilation: it will be referred to as Control.

A first dynamic CT with apneic oxygenation was acquired at baseline at a constant pressure of 5 cmH_2O, to study the cardiogenic motion in healthy conditions. The exposure time for a single projection, which will be called *integration time*, was set to 3 ms, as a compromise between signal to noise ratio and time resolution; the delay between two exposures was set to 4 ms: the time interval between the start of the exposure of consecutive projections was therefore of 7 ms, corresponding to a time resolution of 10 ms (see Section 2.3.1) and a frame rate of 135 fps. This frame rate corresponded to the maximum frame rate achievable as previously stated (Section 4.2.2). The speed of rotation of the stage was set to obtain approximately 1000 periods of the heartbeat. An average heart cycle of 300-350 ms in the anesthetized rabbit determined a total scan duration of approximately 5 minutes, corresponding to 34,200 projections and an entrance dose (air kerma) of 30 Gy. This value was computed multiplying the dose rate previously reported (Section 4.2.2) by the duration of the scan. Due to the high frame rates, the X-ray shutters of the beamline could not be used and the animal was irradiated for the whole duration of the scan.

After the baseline scan, the injury was induced. The choice of not acquiring a dynamic scan with ventilation before injury was due to the high dose delivered: the short-term effect of the radiation dose on the lungs and on the development of the injury was a priori unknown.

When the criteria to stop injurious ventilation were met, a first dynamic CT with ventilation was acquired. Due to the ECG triggering and to the fact that the tomographic acquisition was performed after injury, the settings of the mechanical ventilator were slightly differing for each animal. The PEEP was set to 5 cmH2O and F_{IO_2} to 100; the respiratory rate was between 30 and 40 breaths per minute, the inspiratory/expiratory ratio 1:2 and the driving pressure (P_{MAX}-PEEP) between 15 and 25 cmH_2O. The ventilator settings for baseline ventilation, injury induction, imaging and protective ventilation after injury are summarized in Table 4-1. The integration time was set to 3 ms and the delay between two exposures to 8 ms, giving a time interval between the start of the exposure of consecutive projections of 11 ms, corresponding to a frame rate of 90 fps and to a time resolution of 14 ms. The speed of rotation of the stage was set to obtain approximately 1000 respiratory cycles; the aforementioned respiratory rate determined a total scan duration of approximately 30 minutes, with 147,500 projections acquired and an entrance dose (air kerma) of 200 Gy. The long duration of the scan was the reason why the frame rate was reduced with respect to the scan in apnea: the maximum frame rate couldn't always be maintained for 30 minutes, leading to an error in the data transfer to the ESRF server.

After the dynamic scan with ventilation, a bolus of 10 ml of iodine (Iomeron 400, Bracco Imaging France) was administered and a second scan in apnea was performed. The settings of this scan were equal to the settings used for the scan at baseline. The iodine was injected to distinguish edema from atelectasis: they are in fact characterized by a similar density and contrast in the CT.

The protocol was modified for rabbit 5: iodine was administered during the lavage, in order to better visualize the extension of the edema already in the dynamic scan with mechanical ventilation.

The total duration of the protocol could vary, depending on the time required by the injurious ventilation, but, on average, it was 8 hours from anesthesia induction.

	PEEP(cmH_2O)	**P_{max}(cmH_2O)**	**V_T($ml \cdot kg^{-1}$)**	F_{IO_2}
Baseline	5	15	6	50
Injurious ventilation	0	30	9-16	100
After Injury	5	20-25	6	100
Imaging	5	20-30	6	100

Table 4-1 Ventilator settings utilized during the experimental protocol: (i) at baseline, (ii) during injury induction, (iii) in protective ventilation after injury and (iv) during imaging with mechanical ventilation synchronized with the heartbeat. In protective ventilation after injury P_{MAX} depends on the lung compliance of the rabbit.

4.2.6 Lung fixation and histology

At the end of the imaging protocol, the heart and lungs were removed *en-bloc* and fixed by instillation of Formaldehyde 4% through the tracheal cannula at a hydrostatic pressure of 20 cmH_2O. The extraction began approximately 4 hours after the beginning of the injurious ventilation, 30 minutes after the euthanasia. The fixed samples were sliced axially and embedded in paraffin. Lung tissue sections (3 µm) were prepared on glass slides and stained with hematoxylin, eosin and saffron (HES). The slides were scanned under light microscopy at x10 magnification using a LEICA Aperio AT2 microscope.

4.2.7 Implementation of the phase selection for the retrospective gating and image reconstruction

As previously explained (Section 4.2.1.1 and 4.2.1.2), the retrospective triggering techniques described in this Chapter are based on the analysis of the ECG signal recorded during the acquisition; in particular the phase of the lung parenchymal motion was determined using the delay from the R peak. In the scan with apneic oxygenation the phase is simply given by the delay from the R wave; in the scan with mechanical ventilation an index *j* specifying which heartbeat along the respiratory cycle is considered, must be added (see Figure 4-3). The choice of the R wave was simply due to the fact that, in normal conditions, it is easily identifiable. The R peak is an electrical signal corresponding to the depolarization of the ventricles and it is followed by the contraction of the ventricular muscles. The delay introduced by the detection system was unknown a priori, however it introduces only a constant offset in the phase, not affecting the image reconstruction.

4.2.7.1 Automatic identification of the QRS complexes

The R peak, or more precisely the QRS complex, was identified using a Matlab script (version 2017a, www.mathworks.com), based on the approach described in [115]. This approach utilizes the Stationary Wavelet Transform of the ECG signal and the ‘Sym4’ wavelet. The Sym4 wavelet was chosen due to the similarity to the QRS complex. A band-pass filter was applied to the wavelet decomposition of the ECG, keeping the scales corresponding to the expected width of the QRS complex, experimentally found to be in the range 30 ms-60 ms for the anesthetized rabbits. The inverse wavelet transform was applied to the filtered signal and a peak finder was applied to the modulus squared of the result; the peaks were considered as the position of the QRS complex. Figure 4-7 (a) represents an example of ECG signal recorded during the experiment and Figure 4-7 (b) the modulus squared of the ECG reconstructed after the band-pass filtering. The identified positions of the QRS complexes are highlighted with red circles in the figure. It is important to notice that these positions do not correspond exactly to the maxima of the R waves. Translating the detection to the maximum would lead in first approximation to a constant offset. In order to estimate this offset, the Matlab peak finder function was applied to the unfiltered ECG for one sample. The distribution of the differences between the QRS positions found with the two methods, gave an estimate of the offset (mean value ± standard deviation) of ($9 \text{ ms} \pm 1 \text{ ms}$). The standard deviation of 1 ms is small compared to the time resolution of the scans (10 ms for the scan in apnea and 14 ms for the scan with ventilation, see Section 4.2.5) and can be neglected. A simple peak finder could have been applied in the specific case of this study to detect the QRS complexes but fails when the signal to noise ratio of the ECG is low, application for which the wavelet approach was implemented.

Once the QRS complexes were identified, a feedback on the detection was obtained computing the time interval between consecutive complexes, corresponding to the duration of the heartbeats. If a complex had been wrongly identified, we would have seen a spike followed by a dip in the heartbeat duration (or vice-versa), or a sudden variation from the mean trend. When such structures were seen during the reconstruction, the ECG signal was checked visually, and the window of the band pass filter in the wavelet domain adjusted to remove the wrong identifications.

4.2.7.2 Implementation of the image reconstruction

In order to sort the projections based on the phase of the parenchymal motion, the following procedure was adopted. We remind that the maximum time resolution of the scan is the inverse of the frame rate T plus the integration time (T=14 ms with ventilation, 10 ms in apnea). For this reason, given a specific delay $\overline{\Delta t}$ (from the j-th QRS complex of the respiratory cycle in the case of the mechanical ventilation), all the projections whose acquisition started in the interval: $\overline{\Delta t} - \frac{T}{2} \leq \Delta t < \overline{\Delta t} + \frac{T}{2}$ from the (j-th) QRS complex were used for the reconstruction of the corresponding phase: $\phi = (\overline{\Delta t}, j)$.

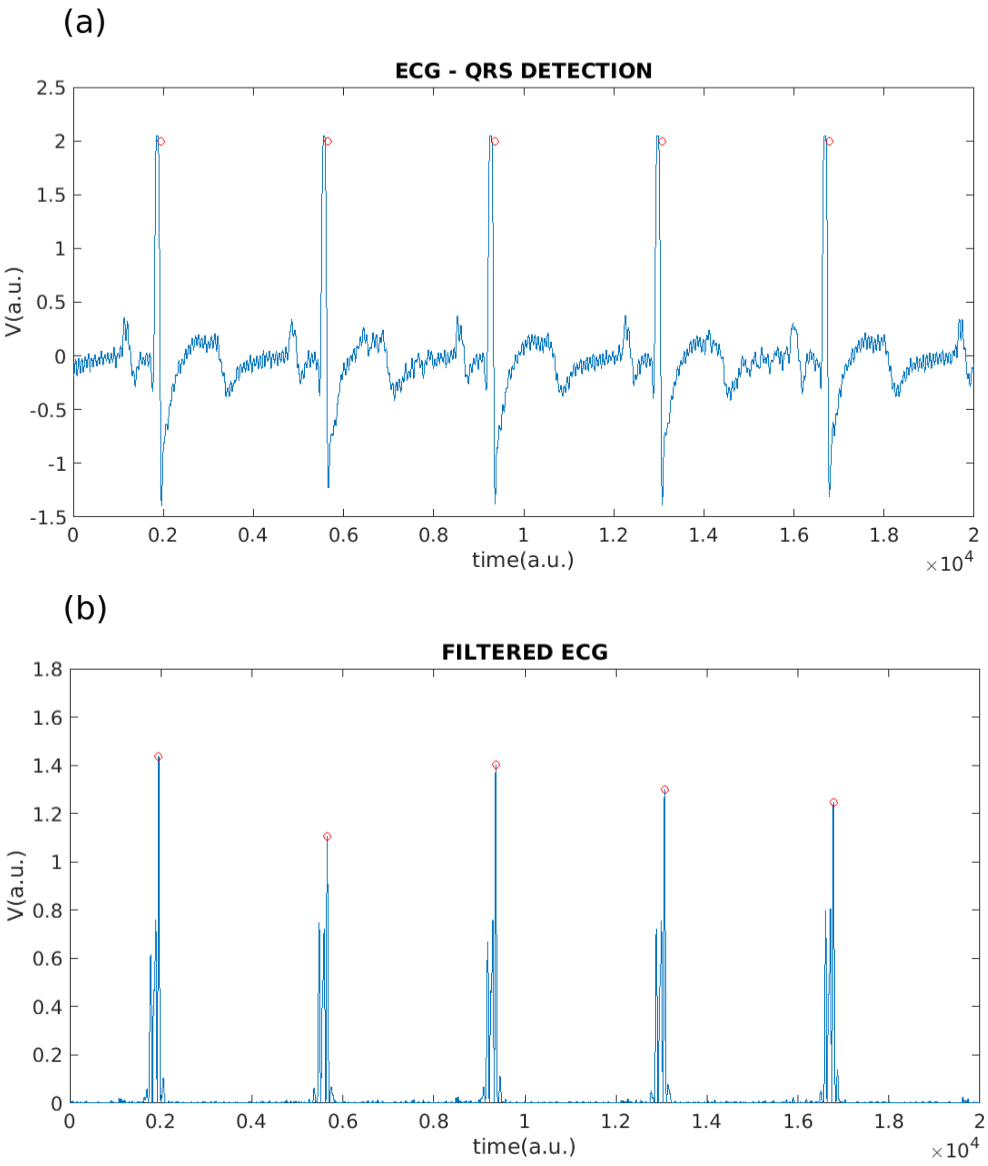

Figure 4-7 (a): Example of ECG signal acquired during the experiment and (b) filtered and saturated ECG signal. The QRS complex detected by the Matlab peak finder are represented with red circles.

Once the projections were selected, X-ray phase retrieval and tomographic reconstruction were performed using the software PyHST2 [116] available on the ESRF computing cluster. The phase retrieval was based on the Paganin's algorithm [69] (Section 2.2.3) and the reconstruction on the filtered back projection (Section 2.2.2). Since the ECG signal is not perfectly periodic, the projections were not equally spaced. The angle associated to each projection was computed knowing the speed of the rotation and the time elapsed since the beginning of the acquisition.

For the scan in apnea one phase every 25 ms was reconstructed along the 300-350 ms heart cycle: this choice was made due to the large amount of data to be analyzed; this time step could have been reduced down to 10 ms, according to the time resolution of the scan.

For the scan with mechanical ventilation 10 to 15 frames were reconstructed, chosen to have a temporal distance of approximately 150 ms in between two of them. Since the reconstruction is based on the ECG analysis, the phases corresponding to the QRS complex of each heart cycle were reconstructed, together with the phases at 150 ms. The duration of the heart cycle is of approximately 300-350 ms, after which the new QRS complex starts, therefore the frames are almost monospaced. If the heart cycle was longer than 375 ms, then a third phase was reconstructed per heart period, positioned at 300 ms from the QRS complex. A higher time resolution is achievable and, according to the frame rate, one phase could be reconstructed in ideal conditions every 14 ms. The choice of having one image every 150 ms was a compromise between the time resolution and time available for the analysis.

4.3 DYNAMIC 3D MICROSCOPY: IMAGE ANALYSIS

The dynamic CTs acquired and reconstructed following the strategy discussed in the previous sections were used to study the dynamics of the lung parenchyma. The technique based on the apneic oxygenation was used to describe quantitatively the cardiogenic lung tissue motion; the dynamic CT with mechanical ventilation associated to the VILI model, to study and quantify the atelectrauma dynamically during the respiratory cycle. In this section the image analysis techniques utilized to study the cardiogenic motion and to quantify the atelectrauma will be presented. These techniques were based on elastic image registration, introduced in Section 2.5. It should be noted that our datasets introduce some challenges with respect to the ones found in the literature, which are mainly acquired with clinical scanners:

1. The first challenge is the reduced field of view in the vertical direction (4.5 mm). The size of the volume is not isotropic and the lungs are only partially imaged; some lung regions move in and out of the field of view during the motion.
2. The resolution is higher compared to the datasets found in the literature, therefore the deformations are larger (relative to the pixel size).

3. Lungs are imaged in injured conditions. Units may open and close during the ventilation (atelectrauma), therefore the one to one correspondence between the volumes is lost.

A robust image registration protocol had therefore to be identified and implemented. In this Thesis existing libraries for elastic image registration were used for the implementation, mainly ITK (Insight Segmentation and Registration Toolkit) and Simple Elastix [117], [118]. Developing a new and optimized image registration library was not the main goal of the work.

4.3.1 Image preprocessing

Image pre-processing was focused on image denoising. Even if propagation based phase contrast imaging coupled to the Paganin’s filter was shown to improve the signal to noise ratio by up to two orders of magnitude with respect to conventional CT for a given dose delivered to the sample [81], the low integration time and the small number of projections required the application of a further denoising algorithm. Anisotropic diffusion was chosen, due its edge-preserving properties [119]. The algorithm implemented in the library Simple ITK (Insight Segmentation and Registration Toolkit, https://itk.org) was used, which is based on the original work by Perona and Malik [119].

The volumes were moreover rescaled by a factor of two to reduce the computational times. The rescale was not expected to reduce the spatial resolution achievable with our detection system, found to be approximately 3 times lower than the pixel size for the 3 µm and 6 µm optics [109].

4.3.2 Quantification of the cardiogenic motion using elastic image registration

The quantitative study of the cardiogenic motion of the lung parenchyma was based on elastic image registration. By comparing two phases of the motion along the cardiac cycle, image registration allows to estimate the local displacement (displacement vector field) and the local expansion or contraction (Jacobian of the transformation) of the lung parenchyma (see Section 2.5.3). The displacement vector field and the Jacobian were computed in this work using the Lagrangian approach, to estimate the maximum displacement and the maximum expansion (strain) of lung units induced by the heartbeat. The reference volume was chosen as the one acquired on the QRS complex, i.e. in diastolic phase.

Several image registration protocols were tested during this work to find an approach stable enough to be sample-independent, due to the high number of datasets to be analyzed. The first protocol applied was based on the library ITK. This approach was chosen because already in use inside my laboratory. It was originally developed to realign lung CT slices acquired following the technique described by Broche et al. [14], described in Section 2.4.2. The peculiarity of the dynamic scan with apneic oxygenation, with respect to the approach by Broche, is that the pixel size is smaller (20 µm vs 40 µm) and that the cardiac gating is introduced; the image registration protocol must be able therefore to describe the cardiac-induced deformations which are highly localized in the ventral region around the heart. To check the convergence and evaluate the result of the image registration procedure, the qualitative and visual approach of the checkerboard image was used (Section 2.5.3)

4.3.2.1 First image registration approach: conjugate gradient optimizer with ITK library

This first method was based on a B-spline transformation; as a cost function the sum of the square difference between the reference and the moving volume was chosen. The cost function was minimized using the Conjugate Gradient Line Search (CGLS) optimizer. The B-Spline was defined on a grid which was set considering an isotropic spacing of 1.6 mm. It is important to remind that the reference and the moving volumes were rebinned by a factor 2 during the preprocessing and were characterized by an isotropic pixel size of 40 µm. For the registration a multiresolution approach was used (Section 2.5.2), with rescaling factors 16, 8 and 4. The size of the grid at this stage was not adapted to the different scales: the spacing remained fixed and equal to 1.6 mm. The grid spacing and the minimum rescale of 4 in the multiresolution approach were imposed by the long computational times. Moving to a finer grid with spacing of 0.8 mm and a minimum rescale factor of 2 was leading to an image size of 700×700×100 voxels and 24,000 nodes, corresponding to 70,000 free parameters, giving a computational time of approximately one week on a local powerful desktop PC (2 CPUs: Intel Xeon @ 2.6GHz × 14, 512 GB of RAM).

4.3.2.2 Second image registration approach: low memory Broyden-Fletcher-Goldfarb-Shanno optimizer with ITK library

As will be shown in Section 4.5.4, the convergence of the first protocol showed a strong dependency on the dataset and was therefore discarded. A second protocol was tested, always based on the library ITK. This protocol consisted in using the Low Memory Broyden-Fletcher-

Goldfarb-Shanno (L-BFGS) optimizer to replace the Conjugate Gradient Line Search. This optimizer is used in literature in lung volume registration associated to B-Spline transformation models (an example is Yin et al. [96]), due to its ability to handle the high dimensionality of the parameter space (Equation 2-8). Except from the optimizer, all the parameters used in the procedure were equal to the ones previously described with the CGLS: they represented the best compromise between image quality and computational time. This second approach proved to be more stable with respect to the first protocol, but was not precise enough to describe the displacement of the small blood vessels in the ventral regions, where distortions were introduced, as will be shown in Section 4.5.4.

4.3.2.3 Third image registration approach: gradient descent optimizer with Simple Elastix library

Before implementing a regularization term in the cost function with ITK, to further optimize the second approach and to remove the distortions in the ventral region, the library Simple Elastix was tested. Simple Elastix has some simple regularization terms already implemented. The one tested in this work comes from a physical model: it is the 3D extension of the potential energy accumulated by a thin plate of metal under bending; it is described in Rueckert et al. [90]. This regularization term acts on the second spatial derivatives of the transformation, penalizing the non-affine ones: it can therefore reduce folding. It was added in the cost function to the sum of square difference of the volumes, with a weight of 1 (the ϵ parameter defined in Section 2.5.1); as optimizer the Gradient Descent algorithm was chosen. The transformation model was based on 3D B-Splines as in the previous approaches. To improve the convergence of the registration algorithm a multiresolution approach was utilized, with scaling factors 8, 4 and 2 thus achieving a double resolution with respect to ITK (which utilized the factors 16, 8, and 4). The spacing of the grid, on which the B-Spline approximation was defined, was adapted to the different resolutions starting as 1.6 mm for the scaling factor 8 and 4, to be decreased down to 0.8 mm for the highest resolution. A Gaussian smoothing was used with standard deviation equal to one half of the scaling factor, to improve the convergence at low resolution. This approach was the fastest and the most stable. It was therefore applied to all the volumes, without appreciable variations in the accuracy, proving to be sample independent. An example of result achievable and the importance of the regularization term will be discussed in Section 4.5.4.

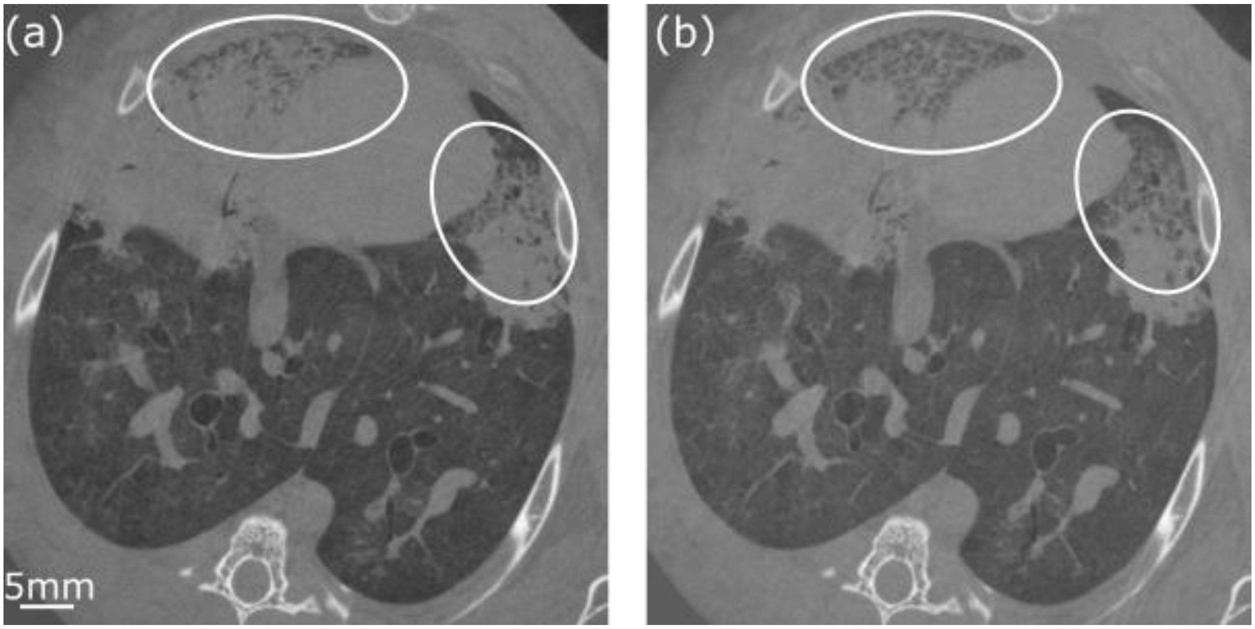

Figure 4-8 Thoracic CT of injured lung showing recruitment between (a) and (b). Dense (or closed) regions are in light grey. A decrease in density, associated to opening of lung units, is observed in the regions highlighted by the white circles.

4.3.3 Quantification of the atelectrauma

As introduced in Chapter 1, atelectrauma is the cyclic opening and closing of lung units, occurring during lung ventilation, especially in injured conditions. An example of opening, or recruitment, is visible in Figure 4-8: two volumes, acquired towards the end of inspiration are shown. Recruitment is visible when comparing the ventral regions of the two slices: dense or closed regions are represented in light gray, while aerated regions are in black or dark gray. When considering the time frame (b) we notice an increase in dark areas in the regions inside the white circles. One way to detect atelectrauma is therefore to realign the volumes and to compare the density of corresponding regions. An increase in density corresponds to closure of airways and alveoli and a decrease to opening. To realign volumes corresponding to different cardiac phases and airway pressures image registration can be used.

4.3.3.1 Elastic registration of lung volumes acquired during mechanical ventilation

When lungs are under mechanical ventilation, their motion significantly increases in complexity with respect to the cardiogenic motion, which was the subject of the previous section. Superimposed to the cardiogenic motion, there is in fact the variation in lung volume, due to inflation and deflation, and a general displacement in the vertical direction, due to the motion of the diaphragm. This creates additional challenges to the image registration procedure. Since the field of view is fixed and limited to 4 mm in the vertical direction, parts of the lung will move in and out of the field of view, thus resulting in missing information during image registration at the boundaries of the volume. Moreover, the lobes slide on each other and on the ribs: this results in a discontinuity in the displacement field to be estimated. In injured conditions a further complication is introduced by the atelectrauma, which introduces non-corresponding structures in the test and in the reference volume (Figure 4-8). By taking these effects into account, it was decided to realign the volumes following the Eulerian approach, introduced in Section 2.5.3. In the Eulerian approach only volumes corresponding to consecutive time frames are registered. If the time interval between consecutive frames is short compared to the period of the ventilatory motion, the difference in lung pressure, lung structures and the vertical displacement are small enough for the registration to converge.

Using the Eulerian approach, it was possible to apply the same algorithm utilized in the case of the apneic oxygenation, i.e. the third approach based on Simple Elastix. The only difference is that an initial affine transformation was applied before the B-spline in order to realign the volumes and to compensate for the vertical translation of the lung. The computational time was 1 hour on a local desktop machine (2 CPUs: Intel Xeon @ 2.3 GHz × 18, 512 GB of RAM).

4.3.3.2 Image analysis: identifying and quantifying atelectrauma

Once two consecutive time frames are realigned, a protocol must be established to define opening and closing of airspaces. As previously discussed, recruitment and derecruitment can be identified comparing the density of realigned volumes. To compare the densities, we decided to define a threshold on the gray level: voxels with an attribute below the threshold were defined as aerated; voxels with attribute above the threshold as non-aerated. The threshold was applied to the reference image and to the transformed moving image. Opening occurs when the status of the voxels changes from non-aerated to aerated, and vice-versa. The threshold was identified empirically from the histogram of the gray levels, since they do not correspond to Hounsfield Units. If we consider the gray level of the air I_A as the mean gray level inside the largest bronchi and the gray level of soft tissue and blood I_B as the mean value inside blood vessels, then the arbitrary threshold I_T corresponding to visually-identified recruitment was an aerated fraction a_f of 45%, where:

$$a_f = \frac{(I_B - I_T)}{(I_B - I_A)}$$

Variations in the mean gray levels of air and blood along the respiratory cycle were smaller than the corresponding standard deviations, therefore the threshold was considered as a constant.

This methodology, based on a pixel by pixel comparison, is affected by two sources of error. The registration doesn't have a one-pixel precision, and therefore the walls of the airways, of the blood vessels and the external walls of the lungs in the reference and in the transformed moving volume won't match perfectly. Since they represent an interface between tissue and air, this mismatch will cause the detection of voxels around these structures as opening and closing. Moreover, isolated voxels having a gray level around the threshold will be classified as opening and closing by the algorithm just due to noise fluctuations. A morphological erosion followed by a dilatation was performed with a 3D kernel of radius 1 in order to reduce the contribution of these two sources of error.

Once a criterium to define recruitment and derecruitment was established, the atelectrauma was quantified by defining the recruitment and derecruitment fractions F_R and F_D. These are respectively equal to the volume detected as opening and closing between the time frames i and i+1 ($V_{R,D}^{i+1}$), normalized to the total lung volume in the field of view at time frame i (V^i):

$$\mathrm{F}_{R,D}^{i} = \frac{V_{R,D}^{i}}{V^{i}}$$

The normalization was adopted to take into account the inflation and deflation during mechanical ventilation and for an inter-rabbit comparison.

Another quantity which was considered was the difference between the recruitment and the derecruitment fractions. This metric is more robust than the individual fractions against mismatches in the image registration. Let's suppose a dense structure is not well realigned: then there will be a dense structure in the reference image superimposed to an aerated structure in the moved image and a dense structure in the moved image superimposed to an aerated structure in the reference one. As a result, the same structure would be counted twice, as recruiting and as de-recruiting. Computing the difference between the recruitment and the derecruitment fraction would remove instead its contribution.

A summary of the acquisition protocols and of the data analysis strategies utilized in this Chapter is presented in

Table *4-2*.

	Apnea	**ECG synchronization**
CT acquisition	Retrospective gating Half acquisition	Retrospective gating Half acquisition
Acquisition Parameters	Time resolution:10 ms Scan duration: 5 min	Time resolution:14 ms Scan duration: 30 min
Pre-processing	Phase retrieval Anisotropic diffusion	Phase retrieval Anisotropic diffusion
Image registration	B-spline transform Gradient Descent Sum Square Difference Bending energy penalty Lagrangian approach	Affine & B-spline transform Gradient Descent Sum Square Difference Bending energy penalty Eulerian approach
Target	Cardiogenic motion	Recruitment Derecruitment

Table 4-2 Summary of the image acquisition and analysis strategies for the two acquisition protocols introduced in Section 4.2.1. Image acquisition and analysis are described in Sections 4.2, 4.3 and subsections within.

4.4 HISTOLOGICAL ANALYSIS: CORRELATING ATELECTRAUMA WITH ALVEOLAR DAMAGE AND INFLAMMATION

In order to correlate the biological damage and the inflammation in the lung parenchyma with the atelectrauma detected in *in-vivo* dynamic 3D microscopy, histological analysis of the rabbit lung was performed. The preparation of the histological sections was described in Section 4.2.6. For the analysis two main strategies were investigated: (i) qualitative description of the injury and (ii) cell counting, to visualize neutrophil infiltration, an index of inflammation. To obtain a quantitative description of the inflammation, immunofluorescence was also attempted. The following molecules were targeted: Interleukin 6, Interleukin 8, Neutrophil (defensin 5), RAGE, found to be expressed in VILI (Section 1.2.2). The staining was not performed by our group and failed in being specific, as it will be shown in Section 4.5.7.3: examples of nonspecific staining will be presented, but the staining protocols tested won’t be described in detail, due to the lack of meaningful results.

4.4.1 Qualitative evaluation of the histology: assessment of the injury

For each lung and for each rabbit, one histologic section was chosen, yielding a total of ten samples. For each sample ten regions of interest (ROI), with size of $800 \times 800\ \mu m^2$ were chosen based on the dynamic CT: where possible, five regions of interest were chosen where lung infiltrates or recruitment and derecruitment were visible and five regions where the lung looked normally aerated during the whole respiratory cycle. It was however not always possible to select 5 regions of interest for each of these two categories, due to the different spatial extent of the injury. It is important to underline that a one-to-one correspondence between CT and histology couldn’t be established, due to (i) the morphological changes occurring postmortem and during the fixation procedure (shrinkage) and (ii) due to the difficulties in finding the same plane in the CT and in the histology. Blood vessels and airways were used as landmarks to identify corresponding regions with the best accuracy achievable. As a result, we can’t identify the regions were the atelectrauma was occurring with high precision and we can’t differentiate between atelectrauma and the overdistension occurring at the edges of atelectatic regions (stress concentrators). This lack of resolution is mitigated in part by the fact that inflammation is not confined to the region where it was originated but spreads to the neighboring areas.

The 100 regions of interest were extracted from the ten corresponding microphotographies, randomized and saved in different files. The file name assigned to the images was a progressive number from 1 to 100 and didn’t contain any information on the microphotography of origin or on the condition of the ROI (injured or normal according to the *in-vivo* CT). The files were then sent to a pathologist of the University Hospital in Grenoble (CHUGA) for the evaluation.

During the qualitative evaluation, the 100 regions of interest were assigned a score from 1 to 4, corresponding to no, mild, moderate and severe injury, similar to Tsuchida et al. [40]. The qualitative score was based on a morphological analysis of the sample. The main parameters taken into account by the pathologist, blinded to the sample condition, were: (i) neutrophil infiltration, (ii) alveolar wall disruption and (iii) formation of hyaline membranes. We remind that these parameters characterize VILI in histological analysis, as discussed in Section 1.2.2.

4.4.2 Quantitative assessment of cellular infiltration

An objective evaluation of neutrophil infiltration was obtained on the 100 regions of interests utilized for the qualitative analysis, using a cell counting procedure based on the software ImageJ (https://imagej.nih.gov/). The cell counting procedure was targeting the cell nuclei, the histological components stained by the hematoxylin. The cell counting procedure consists of the following steps:

1. Gray scale conversion and thresholding: this procedure allows to select nuclei thanks to the dark color staining of the hematoxylin.
2. Morphological closing: to correct for imperfections in the segmented nuclei, closing residual holes.
3. Watershed transform. This step allows to divide nuclei that appeared as connected in the segmentation, due to spatial proximity or to an overlap caused by the 2D projection of a 3D slice.
4. Particle counting: This step is based on a standard routine in ImageJ. It’s a connected component analysis with a thresholding on the circularity and on the size of the volumes, which was used to discard some of the most elongated epithelial type I cells and for noise rejection.

The number of nuclei counted was successively normalized for the tissue length, obtaining a linear cell density. The tissue fraction changes in every region of interest, due to the alveolar structure and depending on the presence of small airways and blood vessels. A python script based on the package scikit-image [120] was written to estimate the tissue length for the normalization:

1. Tissue segmentation based on a watershed approach.

2. Removal of small holes in the segmentation and of isolated neutrophils and macrophages using connected component analysis.
3. Tissue thickness estimation: based on successive morphological opening with kernel of increasing radius. The surface associated to a specific thickness was obtained.
4. Tissue length estimation: obtained from the previous point by dividing the surface by the corresponding thickness.

4.4.3 Statistical analysis

In order to evaluate the correlation between the atelectrauma and the lung injury observed in the qualitative histological analysis, the 100 regions of interest previously selected were classified as “injured” or “non-injured” based on the *in-vivo* CT and successively based on the qualitative score assigned by the pathologist. In the *in-vivo* CT, a region of interest was considered *injured* if densities or atelectrauma were present; *non-injured* if the region was normally aerated. Using the qualitative evaluation instead, a score of 1 was considered as *non-injured* and a score from 2 to 4 as *injured*; the scores from 2 to 4 were summed up due to the lack of statistics for the highest scores, as will be described in Section 4.5.7.1. A 2 × 2 contingency table was built using these two classifications and a Fisher test was applied to evaluate the correlation between the two classifications [121]. A significance level of 5% was used. To perform the Fisher test the software R was used (version 3.5.2, https://www.r-project.org/).

To study the correlation between neutrophil infiltration and atelectrauma the 100 ROIs were divided in “injured” and “non-injured” based on the *in-vivo* CT according to the aforementioned criteria. Two distributions of linear cell densities, computed with the procedure in Section 4.4.2, were obtained. A Wilcoxon rank-sum test [122] was applied to the two populations of linear cell densities (“injured” and “non-injured”) under the null hypothesis that they had equal distributions. A significance level of 5% was chosen. The Wilcoxon test was performed with the software R.

4.5 RESULTS

4.5.1 Stability of the lung parenchymal motion

In Section 4.2 two acquisition protocols for dynamic 3D lung microscopy, based on retrospective gating were presented. The need for a periodic motion was addressed implementing (i) the apneic oxygenation; (ii) a synchronization between mechanical ventilation and heartbeat. In this section the stability of the periodic motion will be presented focusing on ECG and tracheal pressure.

4.5.1.1 Stability of the parenchyma during apnea

An example of the pressure stability reached with the apneic oxygenation implemented in this work is visible in Figure 4-9. It refers to a scan acquired at baseline with a constant pressure of 5 cmH_2O, but it is representative of all the scans acquired during this project at this pressure. The heart rate variability during apneic oxygenation is instead shown in Figure 4-10 and Figure 4-11. Comparing the two figures it is evident that the variability of the heart cycle is animal dependent: in this project was always lower than 15%.

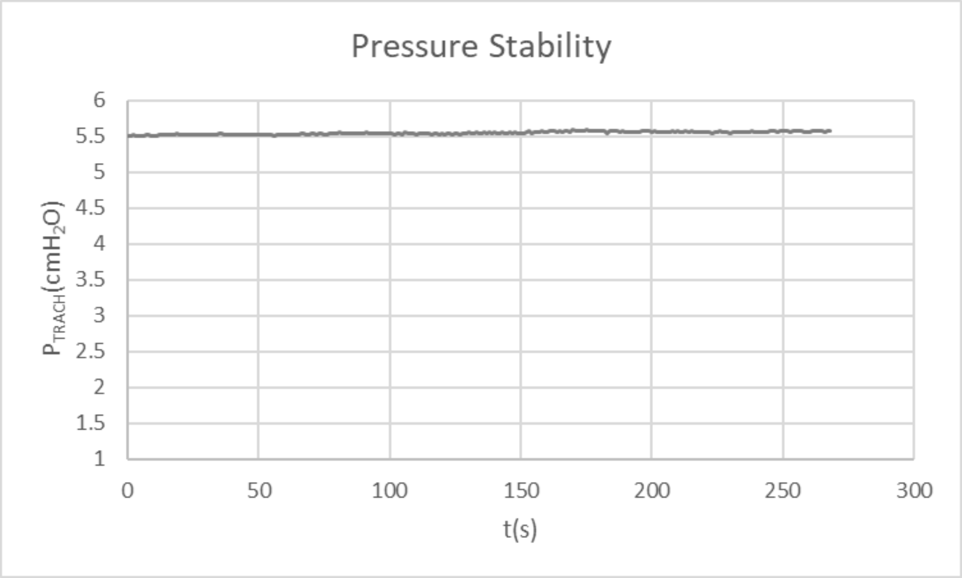

Figure 4-9 Example of pressure stability achieved with the apneic oxygenation.

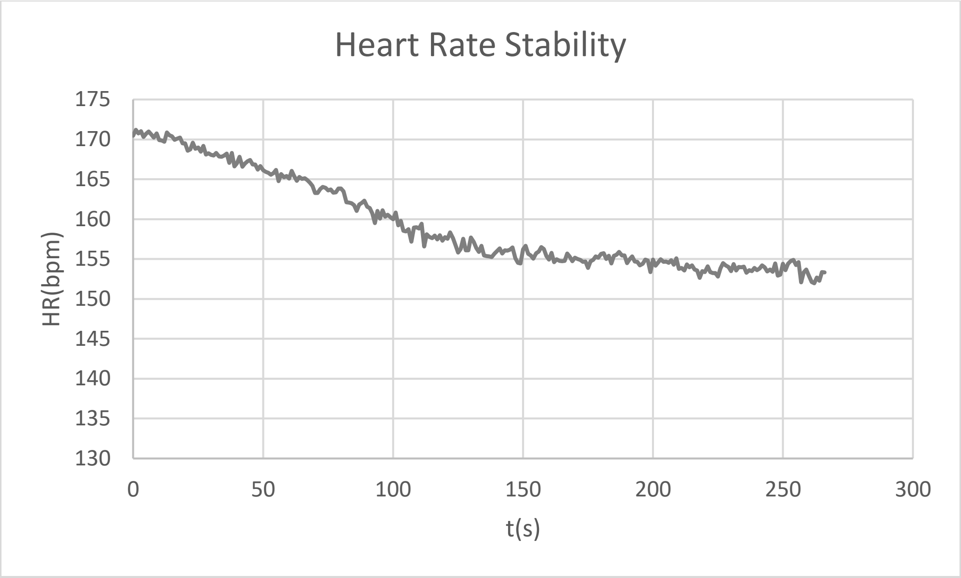

Figure 4-10 Example of heart rate variation during apneic oxygenation. The variation corresponds to 15% in 5 minutes. Scan acquired at baseline.

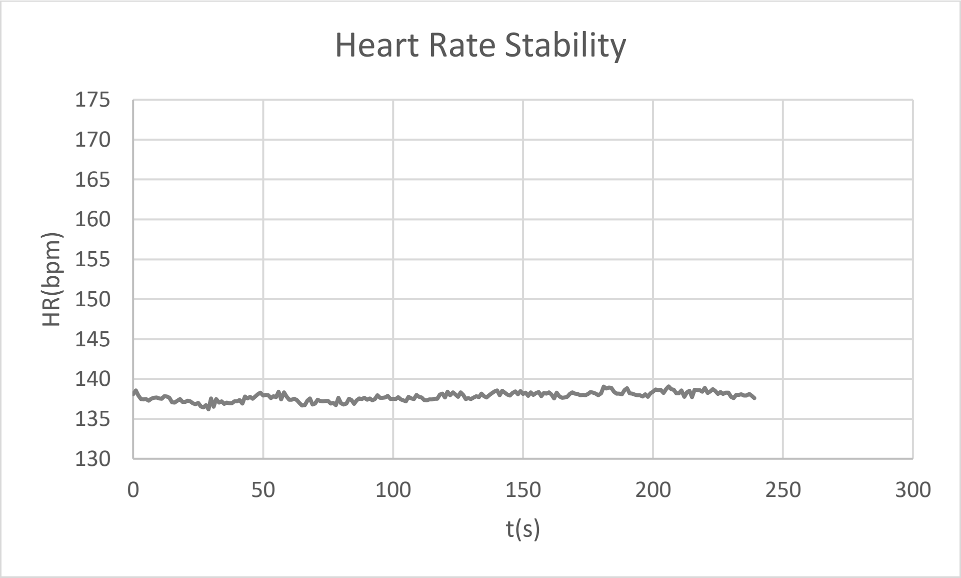

Figure 4-11 Example of heart rate variation during apneic oxygenation. The heart rate was stable along 5 minutes. Scan acquired after injury.

4.5.1.2 Stability of the heart rate during mechanical ventilation

In the scan with mechanical ventilation, the synchronization between mechanical ventilator and heartbeat is based on ECG triggering, as explained in Section 4.2.1.2 and 4.2.3. This approach relies on the heart rate stability which in turns assures the periodicity of the ventilation. Since the inspiration time is fixed, a variation in the heart rate would modify the pressure at which a specific heart phase is acquired during different respiratory cycles. In order to control the periodicity of the lung motion, the distribution of the lung pressures at which each heart phase was acquired, was computed. The uncertainty in the pressure, defined as the standard deviation of the obtained distribution, was on average below 5%. The case in which the uncertainty reached a maximum (9%) is shown in Figure 4-12, obtained at the beginning of the expiration, where the slope of the tracheal pressure reaches a maximum.

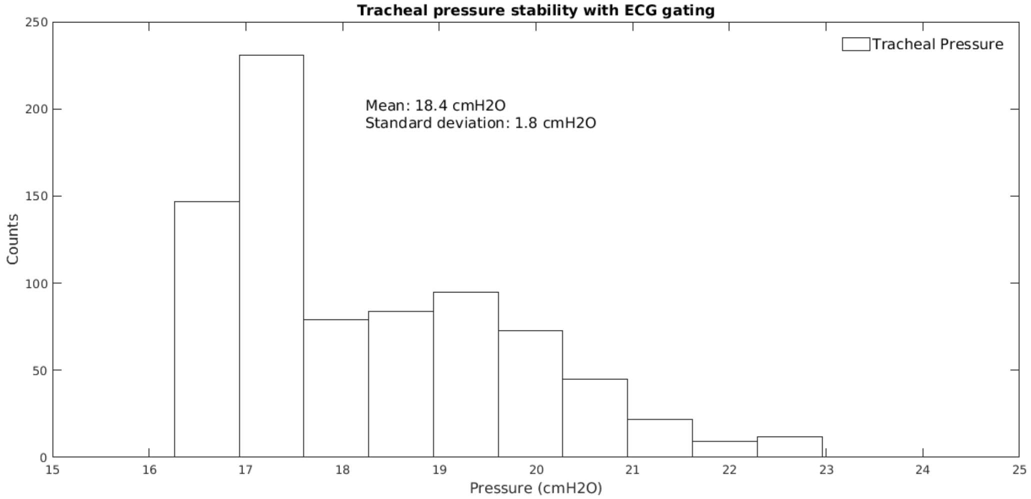

Figure 4-12 Example of the distribution of the tracheal pressures at which a single heart phase was acquired. The case reported is the one with highest standard deviation, corresponding to a relative uncertainty of 9%, obtained at the beginning of expiration, where the slope of the pressure curve reaches a maximum.

4.5.2 Image quality

The image quality achieved with the acquisition protocol under apnea proposed in Section 4.2.1.1 and 4.2.3 is shown in Figure 4-13 (a)-(c). These images were acquired during the development and the optimization of the technique, therefore prior to the experimental phase described in this Chapter, where the VILI model was introduced. The images (a) and (b) were acquired *in-vivo* with the apneic oxygenation at a constant airway pressure of 10 cmH_2O. Image (a) was reconstructed without cardiac gating, by randomly selecting 1000 equally spaced projections: motion artefacts and blurring are visible in the ventral region around the heart. Image (b) was reconstructed with the cardiac gating described in Section 4.2.7, using the wavelet QRS identification: we notice that small airways and vessels are visible in the ventral region, and that the edge of the heart is sharper with respect to (a). Streak artefacts are visible, mainly in the dense and homogeneous regions such as the heart and the fat issue, due to the low the number of projections obtained after the selection of the phase (600). The last image (c) was acquired *post-mortem* keeping the same airway pressure (10 cmH_2O) and is shown as a reference. In the *post-mortem* image, it was not possible to select the same level as in the previous images, due to the fast changes that occur in the lungs post-mortem. The quality of the apneic oxygenation can be noticed looking at the ribs and at the outer surface of the lungs in (a) and (b): all the structures are well resolved, showing a good stability in the pressure and the absence of movements and contractions possibly due to the long apnea and the radiation dose delivered. The periodicity of the parenchymal motion can be appreciated looking at small structures in (b), such as the fissures between the lobes, which disappear in the ungated acquisition (a), thus confirming the stable hemodynamic conditions obtainable through the apneic oxygenation.

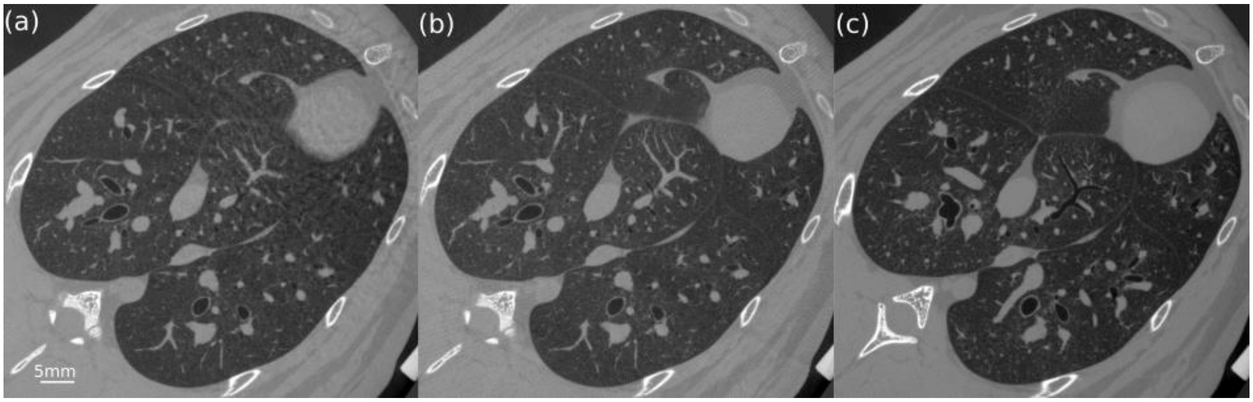

Figure 4-13 Comparison between thoracic CT acquired: (a) in-vivo in apnea without heart gating (1000 projections); (b) in-vivo in apnea with retrospective gating (600 projections); (c) post-mortem (2000 projections). The quality of the gating is visible comparing the ventral region of (a), and (b). The smaller number of projections in (b) results in streak artefacts.

In a more advanced experimental phase, when the VILI model was imaged, it was not always possible to obtain the same image quality just described, as visible in Figure 4-14. In fact the image quality achieved in this case is lower with respect to the one previously shown (Figure 4-13): motion artefacts are present in the left side of the image, corresponding to the right lung. The origin of these artefacts is still unknown. The main hypothesis is related with an instability of the setup. To investigate this topic, an analysis on the projections was performed. The similarity between neighboring projections was computed using the mutual information based on entropy estimates from k-nearest neighbor distances, developed by Kraskov et al. [123]. In this analysis, a projection is chosen as a reference and is compared to all the projections belonging to the following heart cycle. The one which maximizes the mutual information, considered as the most similar, is chosen as the new reference and the procedure is reiterated, until the last heart cycle is reached. A new reference projection is chosen periodically to reduce the effect of the rotation on the image similarity. The choice of using one reference projection per heart cycle, instead of using consecutive projections, was due to the fact that extra information can be extracted. Since each projection corresponds to a cardiac phase, this approach provides information on the ability of the similarity index to identify the same phase in the following heart cycle. This would be useful for a phase selection independent from the ECG analysis. This fine structure was however not used for the following analysis.

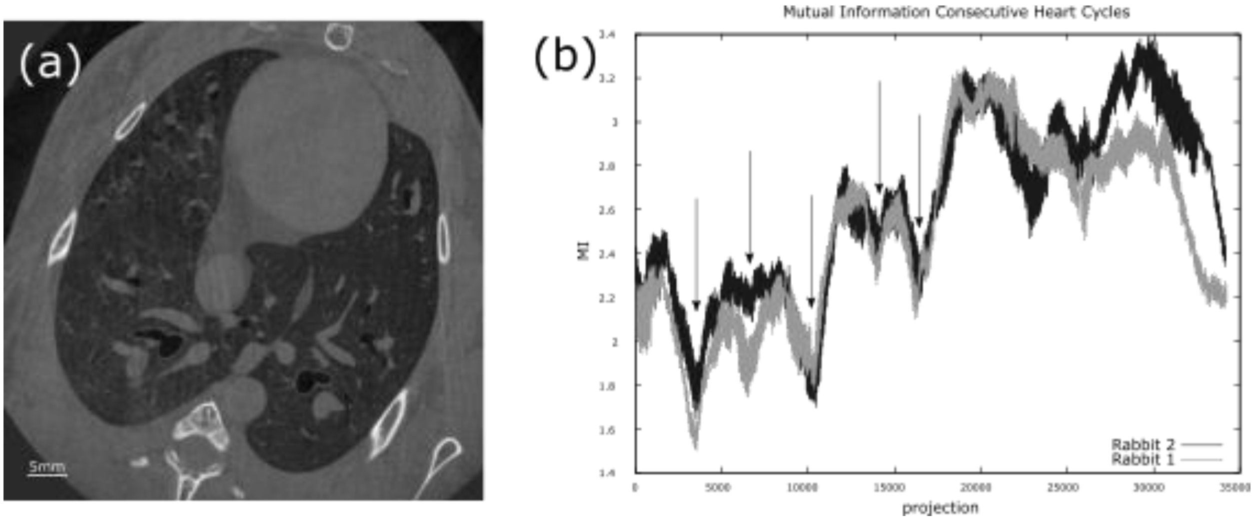

Figure 4-14 (a) Thoracic CT acquired in-vivo in apnea. On the left side (right lung) motion artefacts are visible, mainly in the ventral region. In (b) the mutual information between neighboring projections for two rabbits. Minima at corresponding angles (black arrows) may be due to a mechanical problem, such as a wobbling of the setup.

The results are shown in Figure 4-14 (b), where the mutual information is plotted against the projection number for two rabbits (Rabbit 1 and Rabbit 2). We notice that the mutual information is lower in the first half of the acquisition and that minima are reached approximately at the same projection number for the two rabbits. Since the starting position of the rotation was not modified in between the two samples, and since the speed of rotation was the same, the number of projection corresponds to the same angle of rotation. Since the animals were different, we think that the cause of the drop in similarity was mechanical in nature, probably a wobbling during the first 180 degrees. The absence of the wobbling in the scan shown in Figure 4-13 is due to the fact that the tomographic setup was not fixed and the tower of translation motors had to be mounted at the beginning of each experiment.

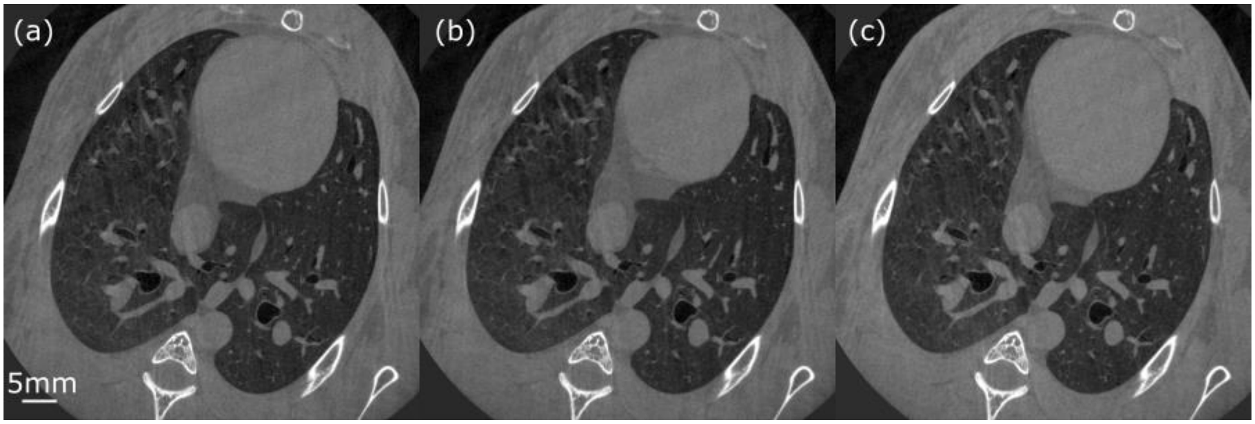

Figure 4-15 Temporal sequence of dynamic CT in apneic oxygenation and pre-injury for rabbit 2. (a) R peak, diastolic phase; (b) 175 ms from R peak, maximum heart contraction; (c) 350 ms from R peak, diastolic phase.

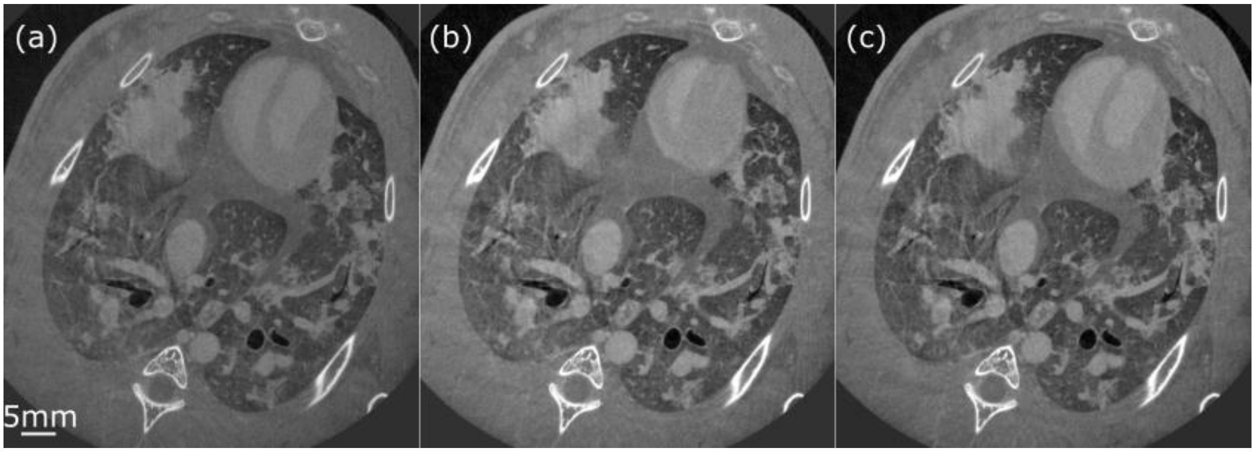

Figure 4-16 Temporal sequence of dynamic CT in apneic oxygenation and post-injury for rabbit 2. (a) R peak, diastolic phase; (b) 200 ms from R peak, maximum heart contraction; (c) 350 ms from R peak, diastolic phase.

Figure 4-15 and Figure 4-16 show an example of time sequence of dynamic CT with apneic oxygenation for Rabbit 2 in healthy and injured conditions. Notice the increased contrast in injured conditions due to the presence of iodine, which highlights for example the heart ventricles and the blood vessels.

The motion artefacts visible in the right lung in the scans in apnea can be as well visualized in the dynamic CT with mechanical ventilation synchronized with the heartbeat. An example of the effect of the gating for this technique is visible in Figure 4-17. Image (a) was reconstructed selecting randomly 1000 equally spaced projections. Image (b) was reconstructed with the cardiac gating described in 4.2.7. To be noted: the increase in quality in both the ventral and the dorsal regions in (b) compared to (a).

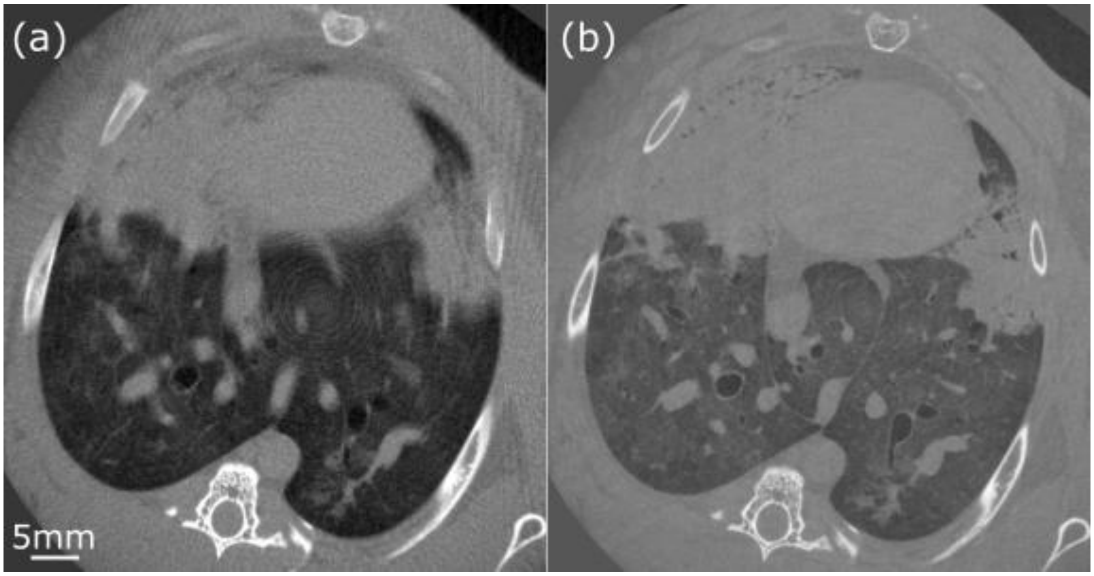

Figure 4-17 (a) Reconstruction of the dynamic CT without ECG gating. (b) Reconstruction with ECG gating at beginning of inspiration and in systolic phase.

An example of time sequence for the mechanical ventilation is visible in Figure 4-18, where three frames are shown, corresponding to the beginning of inspiration (PEEP 5cmH_2O), to the peak tracheal pressure (25 cmH_2O) and to the end of expiration. This scan was acquired prior to the iodine injection, therefore it is not characterized by the same contrast as the apneic oxygenation after injury.

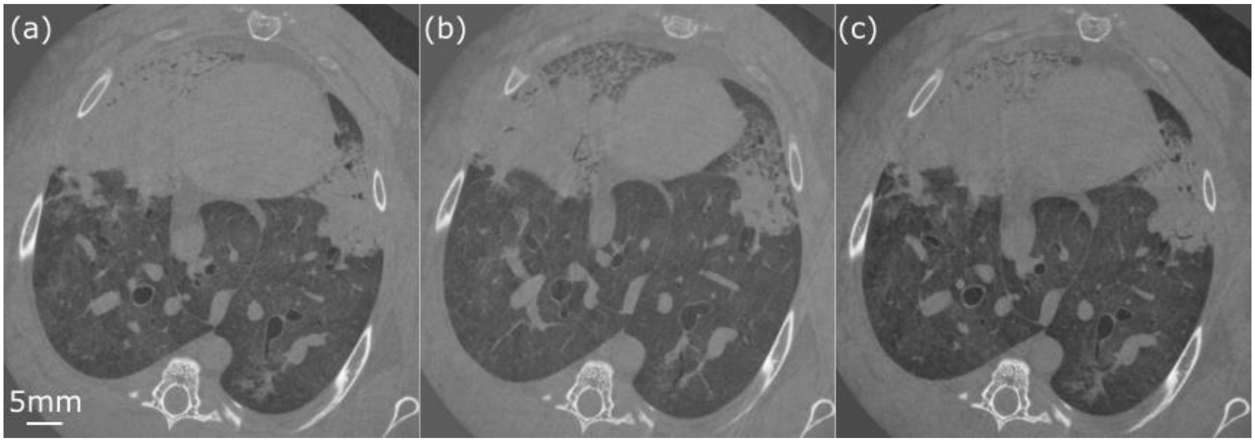

Figure 4-18 Temporal sequence of dynamic CT with mechanical ventilation post-injury for rabbit 1. (a) Beginning of inspiration, diastolic phase (time t=0s); (b) End of inspiration, systolic phase (t=0.75s); (c) End of expiration, systolic phase (t=1.65s).

4.5.3 Lung injury

In Section 4.2.4 the criterion to stop injurious ventilation was defined through the presence of chest infiltrates in the CT and through blood gas analysis. The presence and spatial extent of the chest infiltrates is shown in Section 4.5.6, where a tomographic reconstruction for every rabbit after injury induction is presented. An example was visible in Figure 4-18, in Rabbit-1. In this figure, it is possible to notice that the injury didn't develop homogeneously in the lungs, but it was found to be mainly in the ventral regions; this is valid for all the animals. This could be due to the heterogeneity of the lung itself, as well to the procedure with which the lavage was implemented, i.e. in supine position. In this position the lavage may have removed more surfactant from the dorsal region, causing the following injurious ventilation to go more towards the ventral regions.

In Table 4-3 the $Pa_{O_2}/F_{I_{O_2}}$ ratio during the experiment is summarized, at baseline (BL), at the end of the injurious ventilation (INJURY) and at the end of the experiment (END). To be noticed the peculiar case of rabbit 2, which met the conditions for VILI after the injurious ventilation and which recovered during the last imaging sessions before euthanasia.

$p_{aO_2}/F_{I_{O_2}}$ **(mmhg)**	**BL**	**INJURY**	**END**
Rabbit 1	384	100	84
Rabbit 2	500	107	318
Rabbit 3	508	66	50
Rabbit 4	478	74	40
Rabbit 5	434	41	43

Table 4-3 $p_{aO_2}/F_{I_{O_2}}$ *ratio from the blood gas analysis during the experiment for the 5 rabbits. Values corresponding to three time instants are shown: baseline (BL), end of injurious ventilation (INJURY), end of the experiment (END).*

4.5.4 Optimization of the image registration protocol

In Section 4.3 the challenges introduced by our dataset in elastic image registration were presented. In particular, for the dynamic scan in apnea, three image registration protocols were tested, described from Section 4.3.2.1 to Section 4.3.2.3

4.5.4.1 Registration based on CGLS optimizer

The first approach was based on the library ITK and on the conjugate gradient optimizer. This protocol showed a strong dependency on the dataset, as it can be appreciated in Figure 4-19, and was characterized by a long computational time of about 15 hours on a local powerful machine (2 CPUs: Intel Xeon @ 2.6GHz × 14, 512 GB of RAM) . The slices shown in Figure 4-19 are part of 4D CTs acquired in apnea in healthy conditions. In particular, they represent the systolic phase of the heart transformed to be realigned to the diastolic phase. These phases were chosen to maximize the displacement to be described by the transformation and represent the most challenging case. Images (a) and (b) were obtained with the protocol described in Section 4.3.2.1 including a mask during the registration. The mask is a segmentation of the lung parenchyma: when the mask, a binary image, is applied during the registration, the metric is computed only on voxels included by the mask itself, in this case on voxels belonging to the lung parenchyma. The mask utilized in this work was slightly dilated to include part of the tissue around the lungs: since this structure doesn’t move, it helps regularizing the transform. The mask can be useful to focus only on the structures of interest and could speed up the registration. A perfect result is visible in (a), characterized by a smaller heart volume in the field of view and therefore smaller displacements, while strong deformations along the border of the heart are visible in (b), highlighting the sample dependency of the algorithm and the challenges introduced by larger motions. The artefacts in (b) were reduced when removing the mask (c), however a small deformation remained at the fissure of the left lung (white arrow), one of the regions subject to the largest deformation during the cardiogenic motion.

4.5.4.2 Registration based on the LBFGS optimizer

The second approach was based on the library ITK and the LBFGS optimizer. An example of results with LBFGS is shown in Figure 4-20 (a), where systolic phase realigned to a diastolic phase is shown. The volume is the same as the one presented in Figure 4-19. In (b) an example of checkerboard image, used to visualize the quality of the registration, is visible. As it is possible to see, the main structures were well realigned, and no discontinuities are visible. In particular, the distortion at the level of the fissure, introduced by the first approach and visible in Figure 4-19 (c) was removed. The only mismatch visible in the image is in the ventral region, in the proximity of the heart (Figure 4-20-c). The low spatial resolution, due to a rescale factor of 4 and a coarse grid (1.6 mm of spacing), didn't allow to optimize the small blood vessels in this region, where small mismatches are seen. The final computational time was 2 hours per registration, greatly reduced with respect to the 15 hours of the first approach.

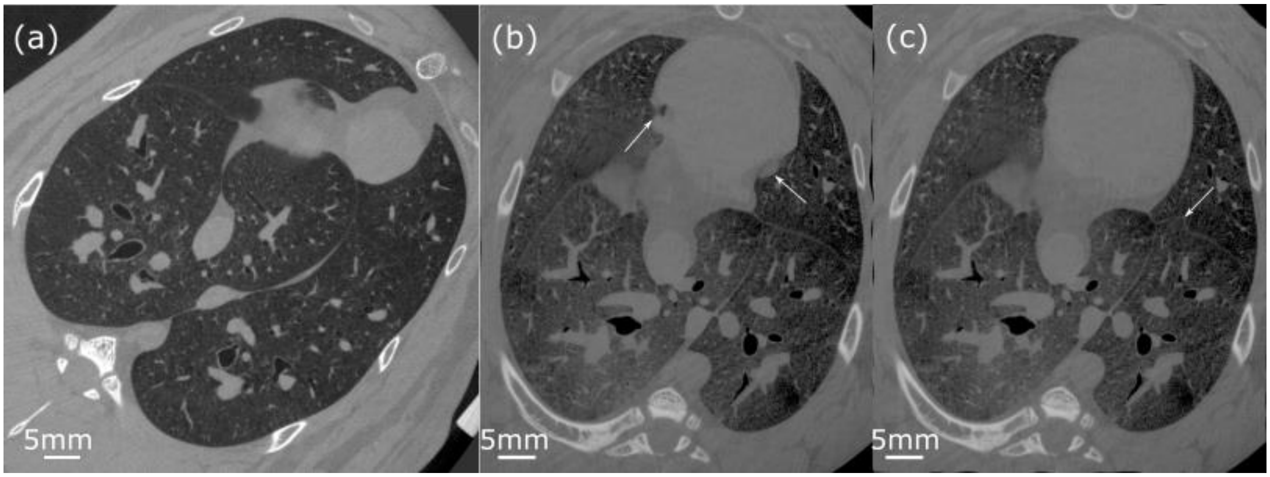

Figure 4-19 Result of the registration with the CGLS optimizer. (a-b) A mask is used to compute the cost function only on the lungs in two different rabbits; (c) same volume as (b), but no mask is used. No artefacts are present in (a), but strong deformations are visible in (b) (white arrows), even if the same algorithm is applied, underlying the sample dependency of the algorithm. Removing the mask (c) solves the main deformations of (b), but errors remain at the level of the fissure (white arrow).

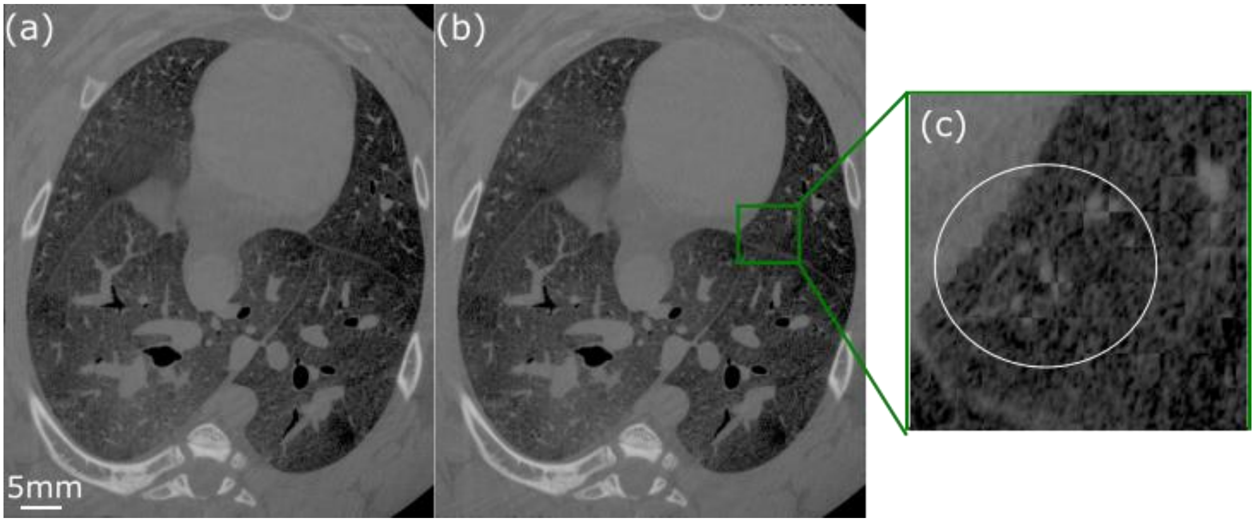

Figure 4-20 (a) Example of result of the registration with LBFGS optimizer. (b) Corresponding checkerboard image: few mismatches are visible, confirming the good quality of the registration. The main artefacts are present in the left lung near the heart: a zoom is shown in (c), with a circle around the mismatch between small blood vessels.

4.5.4.3 Registration based on gradient descent optimizer

The third approach was based on the library Simple Elastix and a Gradient Descent optimizer. Figure 4-21 (b) shows an example of registration obtained with this approach: it represents a systolic phase realigned to a diastolic phase. The quality is visually better than the corresponding ITK registrations presented in the two previous paragraphs, since the artefacts at the edge of the heart were removed. The computational time was reduced from 2 hours to 30 min per registration with a higher resolution compared to the ITK optimizers (minimum rescaling factor from 4 to 2 and grid size from 1.6 mm to 0.8 mm). Figure 4-21 (a) shows moreover the importance of the regularization term in the cost function for our dataset: when not used, folding is created, as indicated by the arrows.

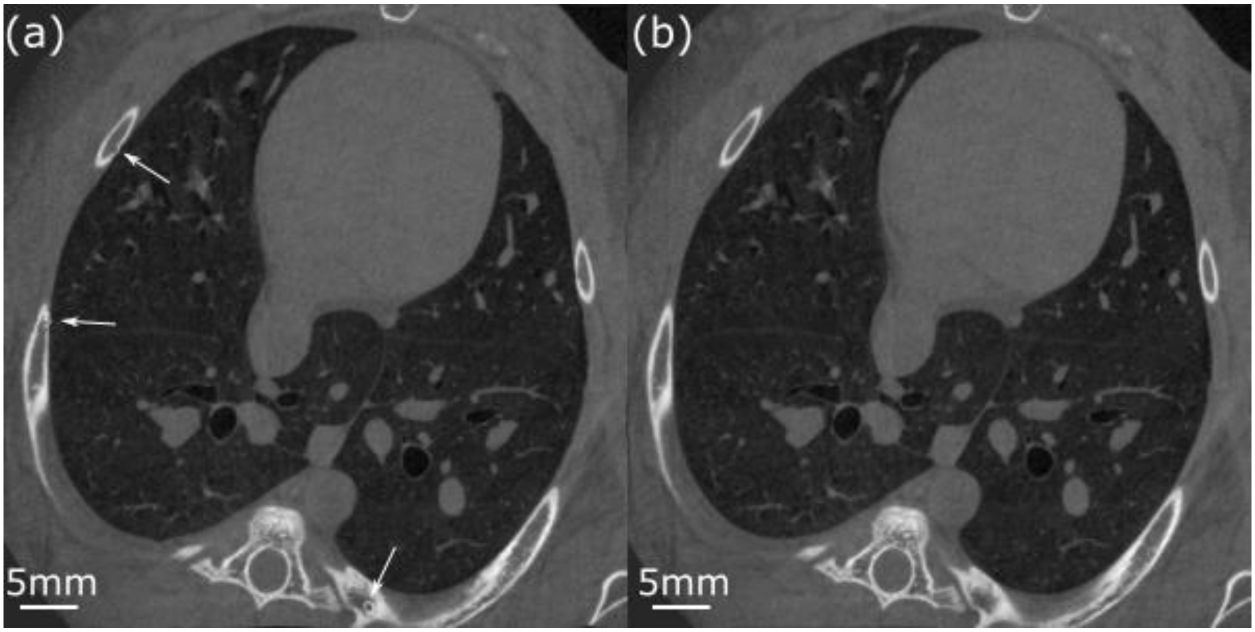

Figure 4-21 Result of image registration with Simple Elastix without (a) and with (b) the bending energy penalty term (Section 4.3.2.3). Distortions are introduced without the penalty term (white arrow).

4.5.5 Quantification of the cardiogenic motion

For each dynamic scan with apneic oxygenation, image registration was used to compare phases which were equally spaced along the cardiac cycle to a fixed reference frame corresponding to the diastolic phase (QRS complex). For this analysis one phase every 25 ms was reconstructed as stated in Section 4.2.7.2. The displacement vector field and the determinant of the Jacobian matrix at each voxel were computed: these fields refer to the rebinned volume and have therefore a voxel size of 40 µm. Due to the fact that part of the lung parenchyma goes out of the field of view during the cardiogenic motion, these maps could be considered reliable in a volume smaller than the one reconstructed, in particular in the vertical direction: approximately 3 mm out of the 4 mm available were used for the analysis. Due to the artefacts present in the right lung (Section 4.5.2), only the results relative to the left lung were considered.

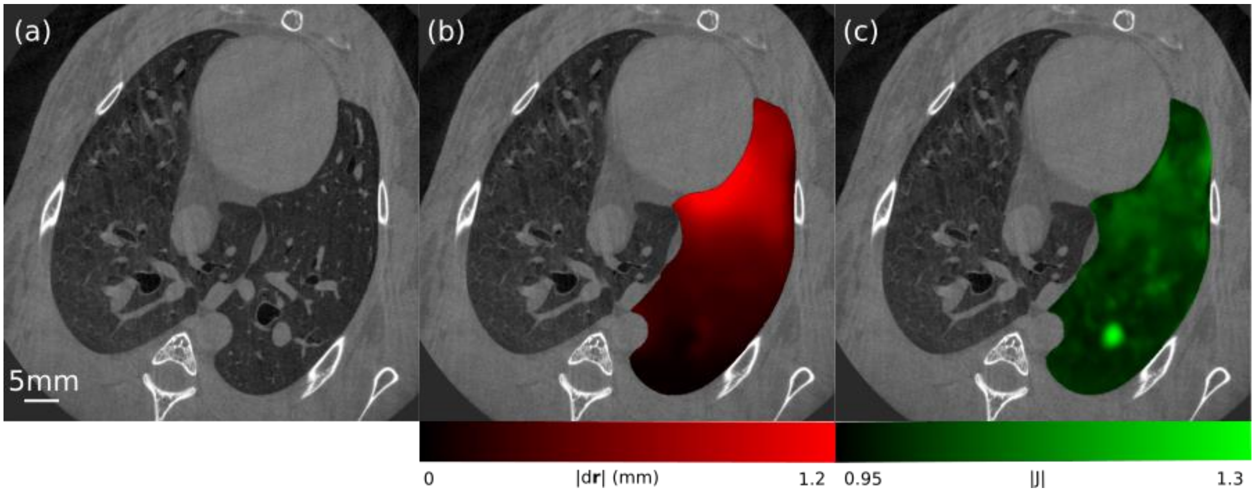

*Figure 4-22 (a) Dynamic CT acquired with apneic oxygenation in healthy conditions. (b) Maximum modulus of the displacement field (|d***r***|) along the cardiac cycle with respect to the diastolic phase. (c) Maximum expansion with respect the diastolic phase along the cardiac cycle, expressed by the determinant of the Jacobian (|J|). The analysis is restricted to the left lung due to the presence of artefacts in the right lung. The segmentation of the left lung was performed manually.*

The maximum of the modulus of the displacement field and the maximum of the determinant of the Jacobian during the cardiogenic motion, with respect to the diastolic phase, are shown in Figure 4-22 and in Figure 4-23 for Rabbit 2; they refer to healthy and injured conditions, respectively. In the specific case reported in the figures, the modulus of the displacement field reaches approximately 1 mm during the systolic phase next to the heart, but the absolute values depend on the gravitational level considered and on the strength of the heartbeat.

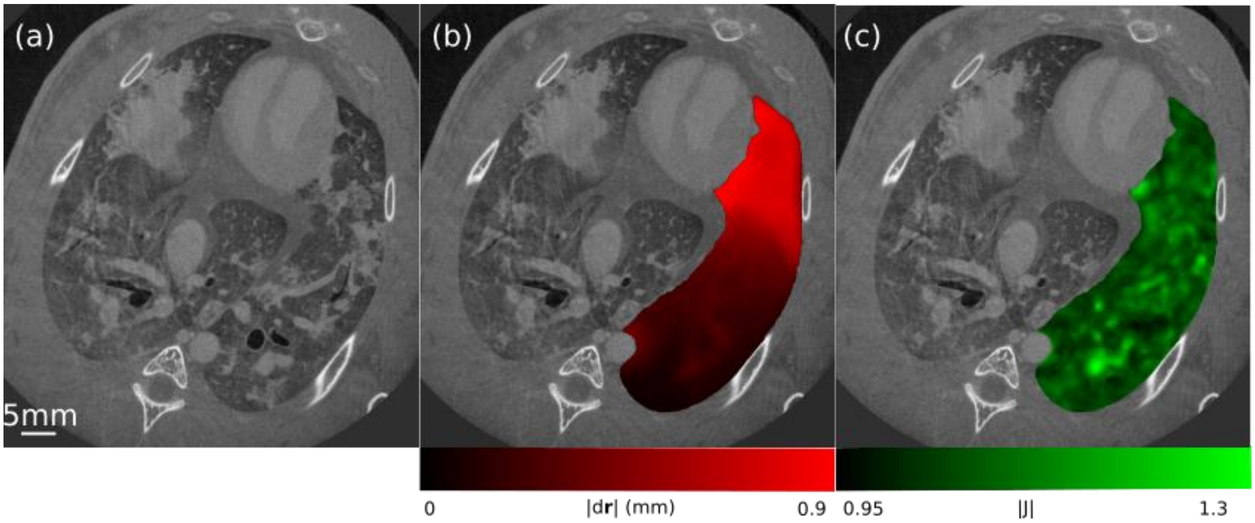

Figure 4-23 (a) Dynamic CT acquired with apneic oxygenation in injured conditions. (b) Maximum modulus of the displacement field ($|d\mathbf{r}|$*) along the cardiac cycle with respect to the diastolic phase. (c) Maximum expansion with respect the diastolic phase along the cardiac cycle, expressed by the determinant of the Jacobian (*$|J|$*). The analysis is restricted to the left lung due to the presence of artefacts in the right lung.*

The highest displacement is mainly localized in the ventral lobe; minimal motion is visible at the periphery of the lung in the dorsal region. The Jacobian is instead heterogeneous: the expansion dependent on the heartbeat, is not localized in the ventral lobe as the displacement, but occurs with the same magnitude in every lung region. The main blood vessels are highlighted, due to their pulsatility: here the Jacobian attains its maximum, equal in this case to an expansion of 30%.

The modulus of the displacement as a function of time in three regions of interest at different distances from the heart and in injured conditions is shown in Figure 4-24. It was computed as the mean value and standard deviation of the displacement modulus in a region of interest of size $(2.7 \times 2.3 \times 1.4\ )\ \mathrm{mm}^3$. The decrease in the amplitude of the motion as a function of the distance from the heart can be appreciated.

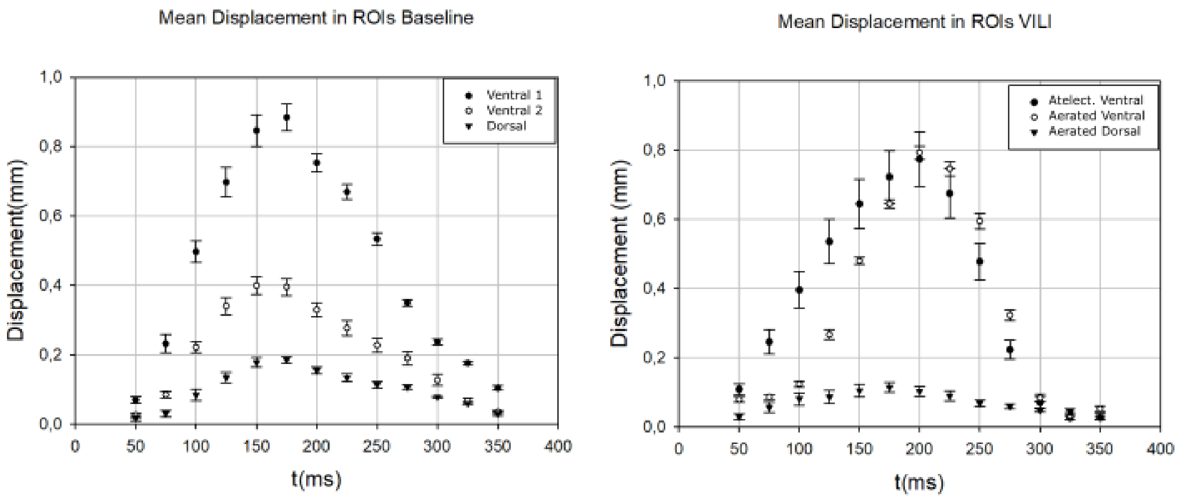

Figure 4-24 Modulus of the displacement field as a function of time in healthy and injured conditions for Rabbit 2. The displacement is an average value in ROIs at different distances from the heart. It was sampled using a time step of 25 ms during the whole duration of the cardiac cycle (approximately 350 ms).

4.5.6 Quantification of the atelectrauma

In Section 4.3.3.2, the procedure utilized to identify and quantify the atelectrauma was described. It was claimed that two sources of error were present, which were mitigated by a morphological erosion and dilatation: (i) the registration doesn't have a precision of one voxel; (ii) voxels with gray level around the threshold may be identified as opening/closing just due to noise fluctuations. To visualize the effect of these sources of error, and to justify the application of the erosion, we performed a connected component analysis on the volumes identified as recruiting and derecruiting before the application of the erosion, and we plotted the size of the volumes as a function of their mean gray level, obtaining the scatterplot in Figure 4-25. An intense peak is visible around the threshold for sizes of the order of 1 or 2 voxels, as expected.

The results of the detection of recruitment and derecruitment are shown from Figure 4-26 to Figure 4-31. They refer to the five rabbits 1-5 and to the baseline one. For the analysis 10 to 15 frames were reconstructed per rabbit, chosen to have a temporal distance of approximately 150 ms in between two of them as explained in Section 4.2.7.2.

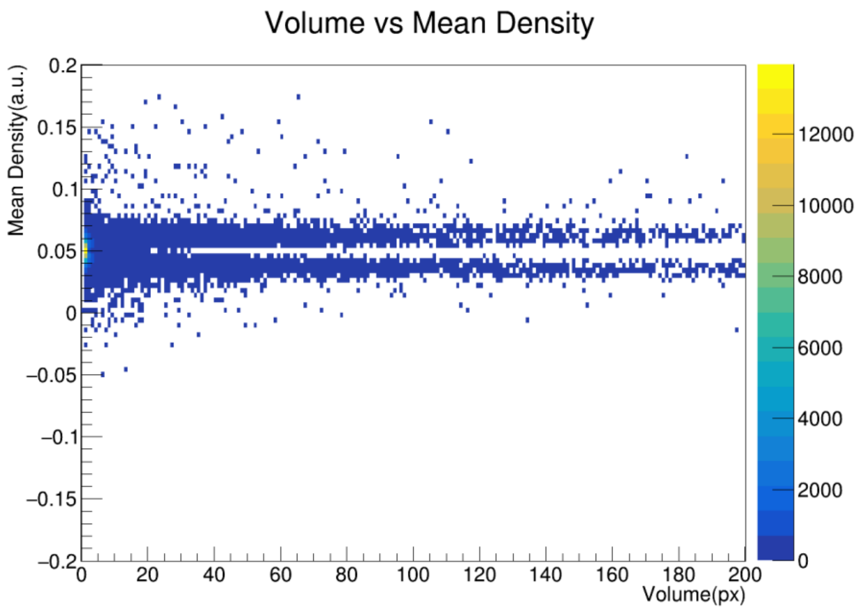

Figure 4-25 Size and initial mean density of the volumes identified as opening or closing, obtained through connected component analysis. The graph is a zoom at small volumes to highlight the peak around the threshold density (0.05). This corresponds to all the voxels with value around the threshold, for which a simple fluctuation caused the detection.

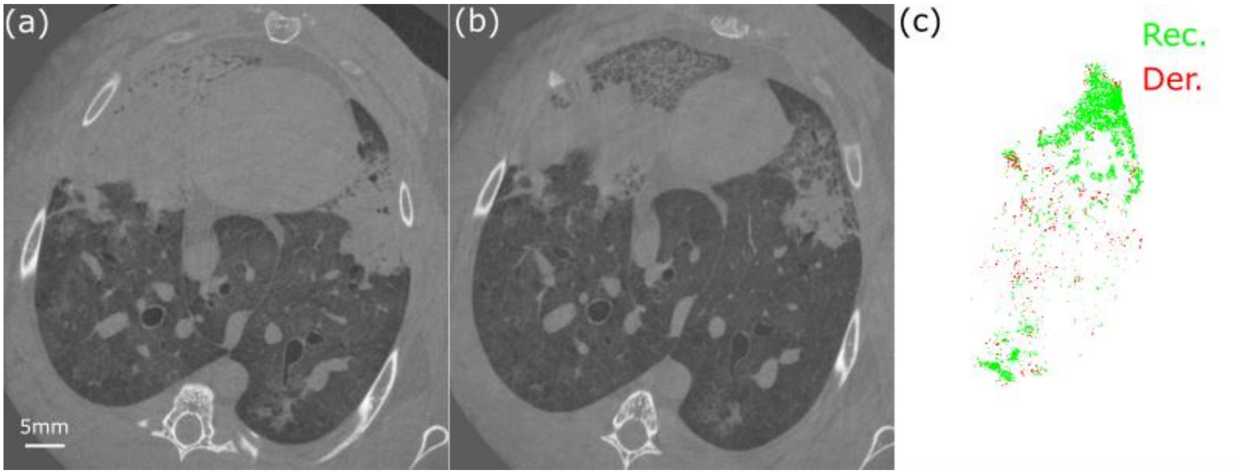

Figure 4-26 In-vivo CT of Rabbit-1 at minimum pressure at the beginning of inspiration (a) and at maximum pressure at the end of the inspiration (b). In (c) a 2D projection of the 3D rendering of the recruitment (Rec., green) and derecruitment (Der., red) as identified by the algorithm. (c) represents the time instant, during the respiratory cycle, where maximum recruitment was observed. Since Rec. and Der. are computed comparing consecutive time frames, no cumulative information is present from the beginning of inspiration.

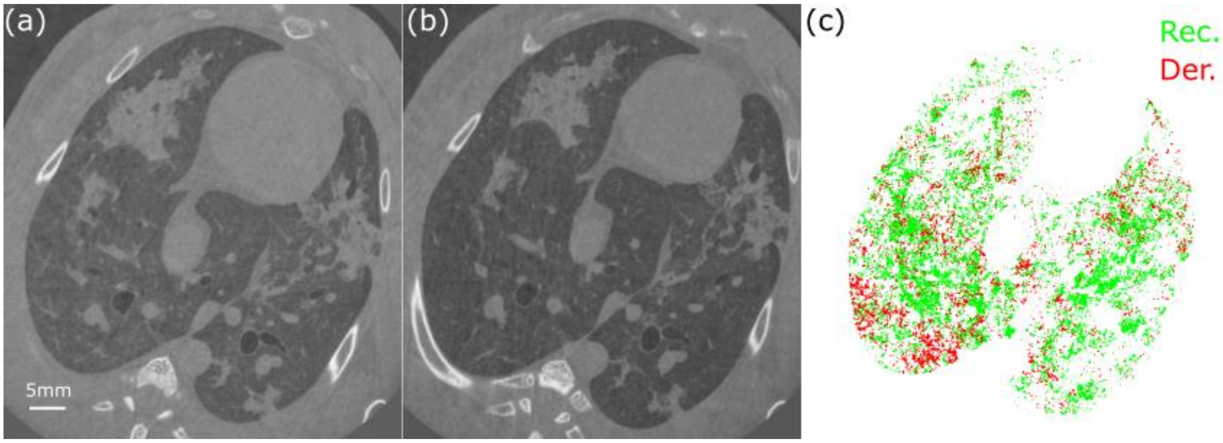

Figure 4-27 In-vivo CT of Rabbit-2 at minimum pressure at the beginning of inspiration (a) and at maximum pressure at the end of the inspiration (b). In (c) a 2D projection of the 3D rendering of the recruitment (Rec, green) and derecruitment (Der., red) as identified by the algorithm. (c) represents the time instant, during the respiratory cycle, where maximum recruitment was observed. Since Rec. and Der. are computed comparing consecutive time frames, no cumulative information is present from the beginning of inspiration.

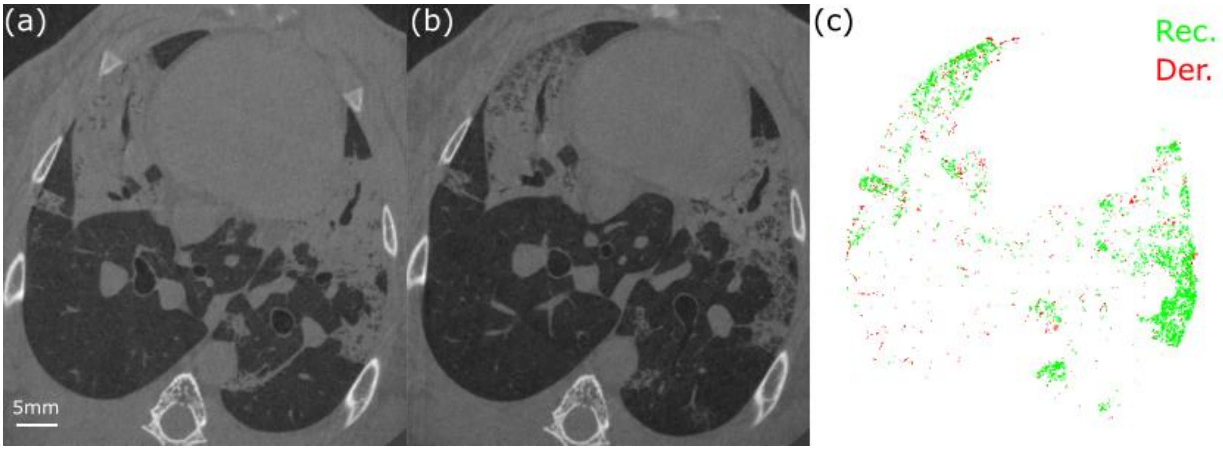

Figure 4-28 In-vivo CT of Rabbit-3 at minimum pressure at the beginning of inspiration (a) and at maximum pressure at the end of the inspiration (b). In (c) a 2D projection of the 3D rendering of the recruitment (Rec., green) and derecruitment (Der., red) as identified by the algorithm. (c) represents the time instant, during the respiratory cycle, where maximum recruitment was observed. Since Rec. and Der. are computed comparing consecutive time frames, no cumulative information is present from the beginning of inspiration.

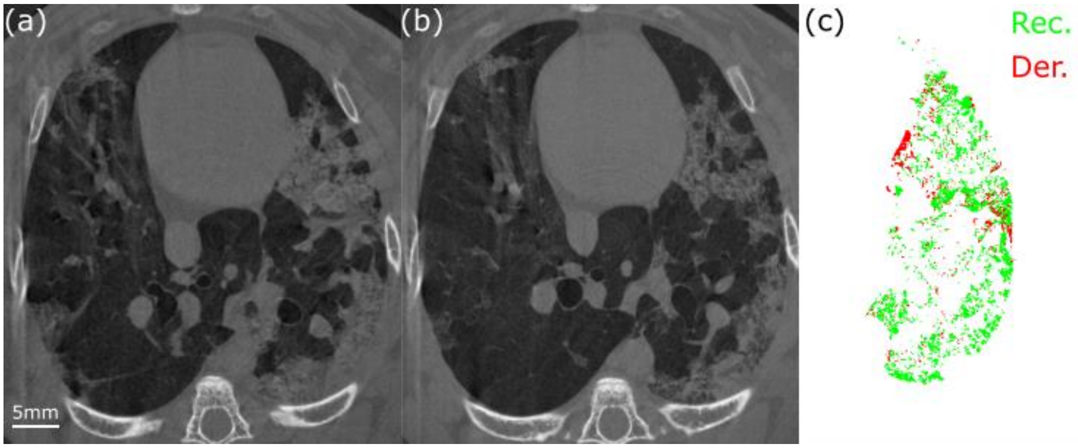

Figure 4-29 In-vivo CT of Rabbit-4 at minimum pressure at the beginning of inspiration (a) and at maximum pressure at the end of the inspiration (b). In (c) a 2D projection of the 3D rendering of the recruitment (Rec., green) and derecruitment (Der., red) as identified by the algorithm. (c) represents the time instant, during the respiratory cycle, where maximum recruitment was observed. Since Rec. and Der. are computed comparing consecutive time frames, no cumulative information is present from the beginning of inspiration.

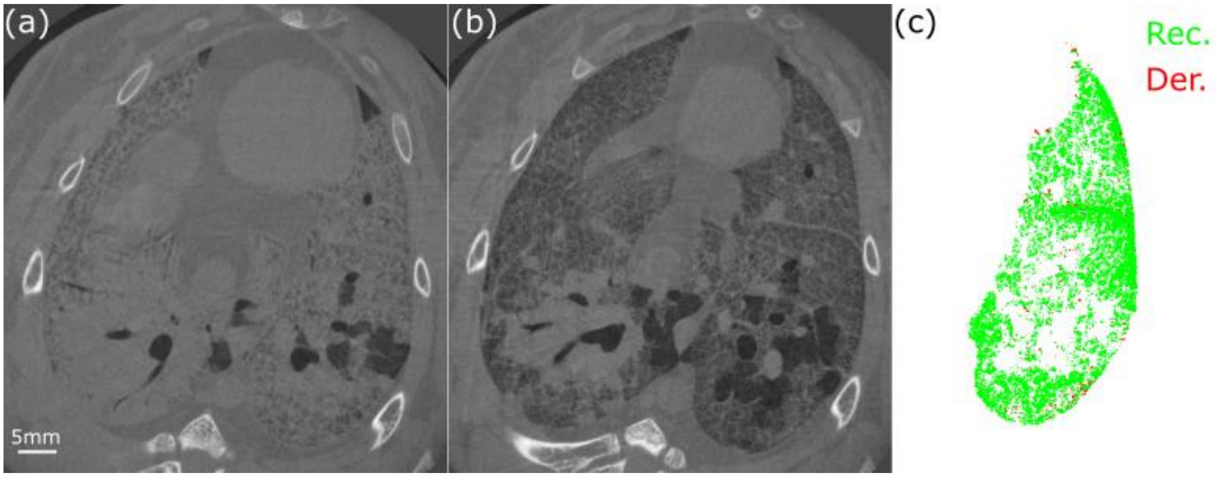

Figure 4-30 In-vivo CT of rabbit5 at minimum pressure at the beginning of inspiration (a) and at maximum pressure at the end of the inspiration (b). In (c) a 2D projection of the 3D rendering of the recruitment (Rec., green) and derecruitment (Der., red) as identified by the algorithm. (c) represents the time instant, during the respiratory cycle, where maximum recruitment was observed. Since Rec. and Der. are computed comparing consecutive time frames, no cumulative information is present from the beginning of inspiration.

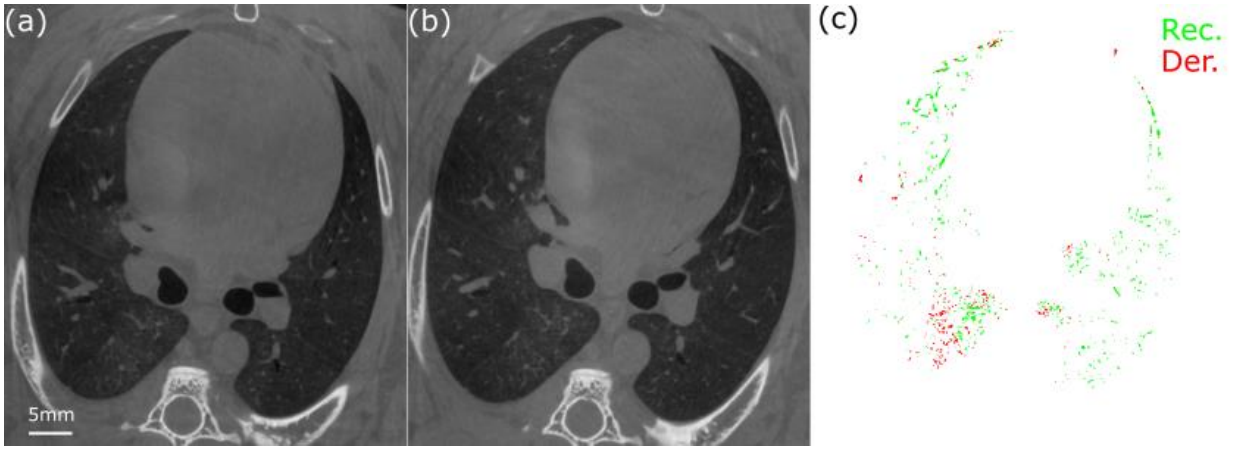

Figure 4-31 In-vivo CT of the control rabbit at minimum pressure at the beginning of inspiration (a) and at maximum pressure at the end of the inspiration (b). In (c) a 2D projection of the 3D rendering of the recruitment (Rec., green) and derecruitment (Der., red) as identified by the algorithm. (c) represents the time instant, during the respiratory cycle, where maximum recruitment was observed. Since Rec. and Der. are computed comparing consecutive time frames, no cumulative information is present from the beginning of inspiration.

The image on the left in each figure (a) represents the lungs at the beginning of inspiration, in diastolic phase. This phase coincides with the QRS peak of the measured ECG. The central figure (b) is the phase, among the reconstructed ones, associated to the highest pressure, usually at the end of inspiration; only for Rabbit-4 it corresponded to the beginning of expiration. These phases were chosen because they represent respectively a highly derecruited and highly recruited volume. The third image (c), is a projection of the 3-D rendering of the recruitment and derecruitment identified by the algorithm on the plane of the images (a) and (b). A recruitment – derecruitment map was computed for every pair of consecutive frames, including a comparison of the last and the first frame to close the cycle, and the map shown in Panel (c) is the one with maximum recruitment fraction. Since the detection was based on the comparison between consecutive frames, this map does not contain cumulative information on the recruitment occurring from the beginning of the inspiration, but only on the recruitment occurring in between the two time frames compared. Either one or both lungs were analyzed for each animal: the right lung had to be discarded in Rabbit-1 and Rabbit-5 due to the presence of the diaphragm and of the stomach in the field of view, and in Rabbit-4 due to the strong motion artefacts, as already discussed in Section 4.5.2. As in the case of the cardiogenic motion, a volume narrower than 4 mm in height could be analyzed, since some lung regions move in and out of the field of view, an effect increased with respect to the cardiogenic motion by the vertical translation of the lung during inflation (see Section 4.3.3.1). The figures show a good agreement between the recruitment detection and the atelectatic regions except for Rabbit-2, where a diffuse recruitment is observed. It is not possible to say with the data at our disposal if this phenomenon was induced by an effective diffuse atelectrauma or by a higher noise in the image.

As a comparison, in Figure 4-32, the recruitment and derecruitment fractions are shown as a function of time; the related tracheal pressure curve is superimposed. Each fraction, comparing the frames at time t_i and t_{i+1}, is shown at the time $(t_i+t_{i+1})/2$, so that the recruitment between time 0 ms and 150 ms is superimposed to the tracheal pressure at time 75 ms, and so on. By observing Rabbit-2 we notice that the maximum of the recruitment occurs at the beginning of the inspiration, it decreases with the inspiration and increases again at the end of expiration. The increase towards the end of the expiratory cycle is likely linked to a corresponding increase in the noise of the image, due to a similar trend in the baseline of the derecruitment. The first peak is centered at a tracheal pressure of ~10 cmH_2O. A peak in the recruitment fraction at the beginning of inspiration, at a similar tracheal pressure, is present also in Rabbit-4 and Rabbit-5.

In Rabbits-1,- 3 and -5, a local maximum in the recruitment fraction was observed towards the end of inspiration, corresponding to a tracheal pressure of ~20 cmH_2O.

The derecruitment shows a main peak at the beginning of expiration for Rabbits-1,-3,-4 and -5; the same rabbits present a peak in the recruitment at high pressure. One difference between recruitment and derecruitment is that the slope of the tracheal pressure curve is higher during expiration: even if the time interval is constant and equal to 150 ms, the difference in pressure between consecutive frames is higher at the beginning of expiration than during inspiration. For this reason, it is difficult to give a value for the tracheal pressure at which the maximum derecruitment occurs. A maximum in the derecruitment is visible at low pressure values for Rabbit-2 and Rabbit-5 (P_{TRACH}~8 cmH_2O); Rabbit-4 doesn't show a peak at low pressure, but its respiratory cycle is shorter with respect to the other animals, and a time interval of 150 ms may not be sufficient to discriminate two peaks.

It is finally important to underline that the control rabbit shows only small fluctuations in both the recruitment and derecruitment curves, compatible or smaller than the baseline of the recruitment and derecruitment curves of the injured rabbits.

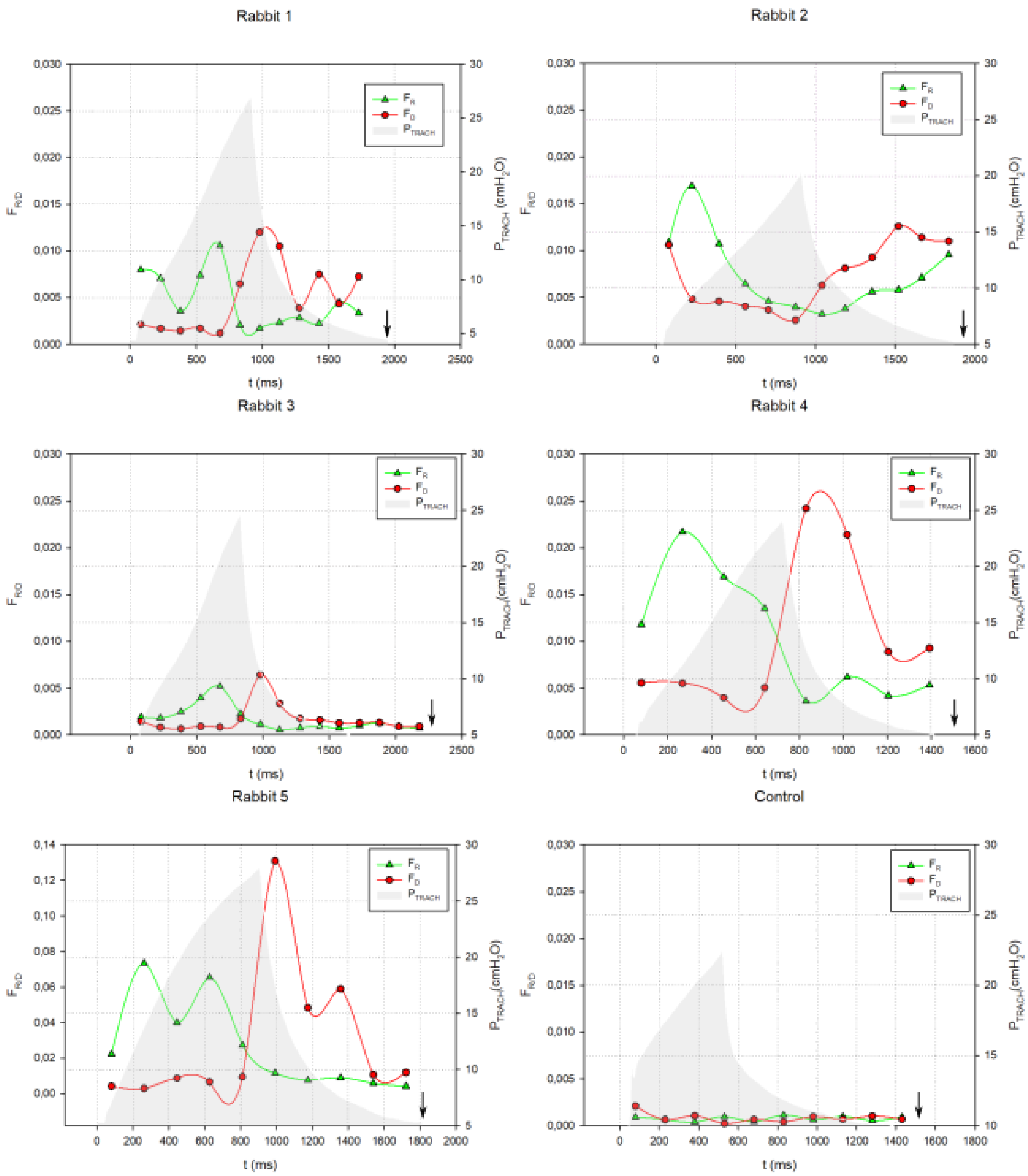

Figure 4-32 Graphs representing the recruitment (F_R) and derecruitment (F_D) fraction as a function of time for all the rabbits. The tracheal pressure curve is shown as a reference: end of expiration is marked by a black arrow. Rabbit-5, having a different injury model is represented as last graph, with a different scale for the recruitment and derecruitment fraction.

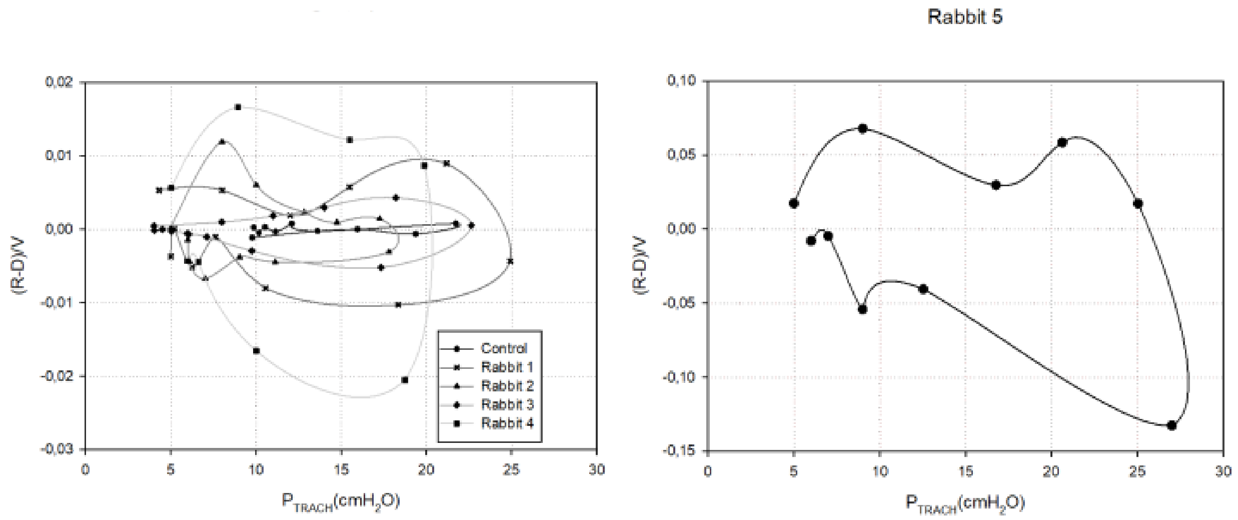

Figure 4-33 Difference between the recruitment and derecruitment fraction for all the rabbits (a) and for Rabbit-5 (b). Notice the prevalence of recruitment during inspiration and the prevalence of derecruitment during expiration, absent only in the control rabbit.

In Figure 4-33 the difference between the recruitment and the derecruitment fraction is shown, to take into account possible increase in the baseline of the curves due to an increase in the noise or to a lower quality of the image registration, resulting in mismatches between structures. As expected, there is a systematic excess of recruitment with respect to derecruitment in all the injured rabbits during inflation, with an excess of derecruitment during expiration. Random fluctuations are visible for the baseline rabbit. Rabbit-5 is shown separately, since the different experimental protocol in the lavage caused a wider distribution of atelectasis.

4.5.7 Histology: qualitative evaluation and cell counting

To study the correlation between atelectrauma and inflammation, regions of interest were chosen in the histology, corresponding to areas where the atelectrauma or densities were visible in the dynamic CT, as explained in section 4.4.1. An example of how the regions were selected is given in Figure 4-34. A dynamic CT is shown, with the HES stained histology corresponding to the lung at each side. In the example shown, the atelectrauma is mostly confined in the ventral lobes. The 20 regions of interest chosen for the two lungs of Rabbit-3 are visible in the figure and were drawn using a color code representing the qualitative evaluation of the pathologist, in this case from mild to severe. We notice in this example a stronger inflammation in the ventral lobes, compatible with what observed in the CT.

4.5.7.1 Correlation between atelectrauma and injury

To assess the correlation between the atelectrauma visible in the *in-vivo* CT and the biological damage identified by the pathologist, a Fisher test was performed, as discussed in Section 4.4.3. The null hypothesis of non-correlated variables was rejected with a p-value of 0.007. The positive correlation proves a higher probability of injury in regions with atelectasis and atelectrauma. The full contingency table, representing the evaluation of the pathologist and the classification based on the *in-vivo* CT is represented in Table 4-4. In this contingency table the lack of statistics at the highest qualitative scores, namely 3 and 4 is visible: this is the reason why it was reduced to a 2×2 contingency table for the Fisher test, as described in Section 4.4.3. The average qualitative score per lung is given instead in Table 4-5.

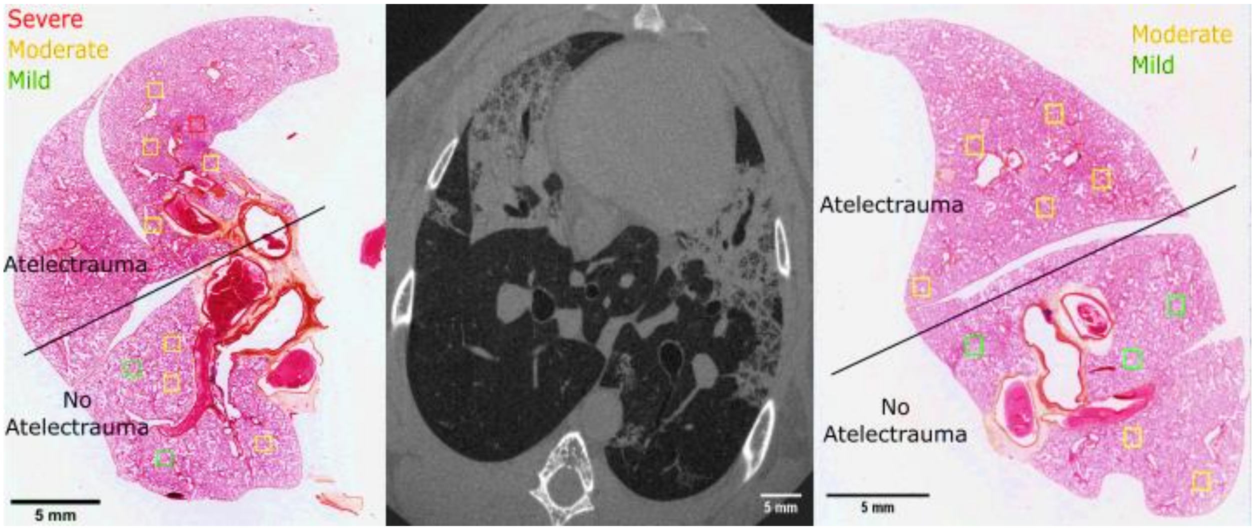

Figure 4-34 HES staining of the lung tissue and corresponding in-vivo CT. On the HES images the regions of interest chosen for the qualitative evaluation are shown, using a color coding representing the score given by the pathologist. The regions of interest were chosen in areas showing atelectrauma in the CT and in areas not showing it, to correlate atelectrauma and injury.

	1(No Injury)	2(Mild Injury)	3(Moderate Injury)	4(Severe Injury)
Injury (CT)	13	24	15	1
No Injury (CT)	24	18	5	0

Table 4-4 Contingency table representing the qualitative score (1 no injury, 2 mild injury, 3 moderate injury, 4 severe injury) vs the classification based on the in-vivo CT. For the Fisher test the qualitative scores from 2 to 4 were added to increase the statistics.

	Mean Score Left	Mean Score Right	Final $\boldsymbol{Pa_{O_2}/F_{IO_2}}$(mmHg)
Rabbit-1	2.1	1.8	86
Rabbit-2	1.0	1.0	320
Rabbit-3	2.7	2.9	50
Rabbit-4	1.8	1.1	40
Rabbit-5	2.0	1.8	43

Table 4-5 Mean qualitative score associated to each lung and $P_{aO_2}/F_{I_{O2}}$ at the end of the experiment (see Table 4-3). The mean score is calculated over the 10 regions of interest chosen per lung in the HES stained slices.

4.5.7.2 Correlation between atelectrauma and cellular infiltration

To correlate the atelectrauma with the neutrophil infiltration, a Wilcoxon rank-sum test was applied to the distributions of linear cell densities relative to the ROIs chosen where atelectrauma was visible or absent in the CT, as explained in Section 4.4.2. It showed that the two distributions are significantly different, with a p-value of 0.04. A higher mean value is obtained for the “injured” regions, showing neutrophil and macrophage infiltrations. A boxplot representing the three quartiles of the distributions is shown in Figure 4-35.

4.5.7.3 Assessment of lung injury using immuno-fluorescence

A quantitative analysis based on UV immuno-fluorescence was attempted. The results for the case of the defensin 5, labeling neutrophils (stained in red under fluorescence), are shown in Figure 4-36. The first image (a) is a region of interest considered as non-injured by the pathologist; the second one (b) is one of the most injured according to same criterion. It is possible to see that all the histological components were stained, therefore any quantitative or qualitative analysis was hindered. Unspecific staining was obtained for all the antibodies tested on the samples.

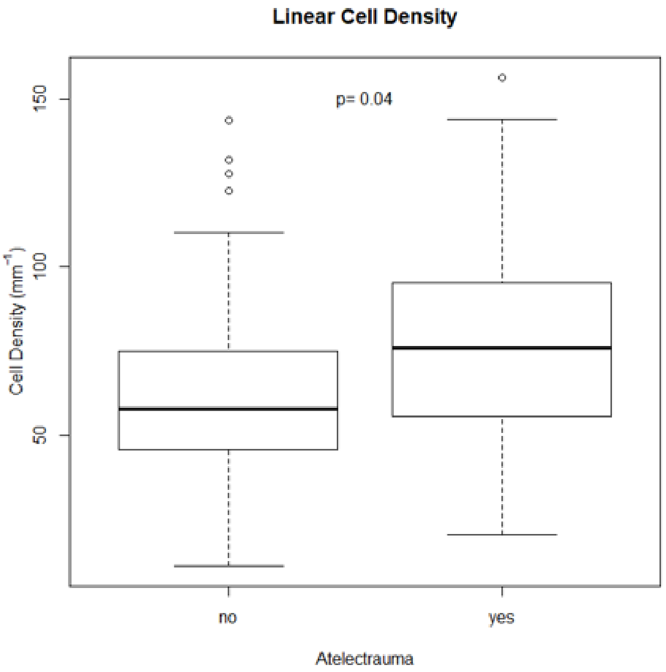

Figure 4-35 Linear Cell Density. Cell counts per unit tissue length, comparing ROIs with (yes) and without (no) atelectrauma. Cell counts are greater in atelectatic regions with p=0.04 following the Wilcoxon rank-sum test.

4.6 DISCUSSION

Two acquisition protocols for *in-vivo* dynamic 3D microscopy were developed, capable of fully resolving the motion of the lung parenchyma in two conditions: (i) constant airway pressure (apnea) and (ii) mechanical ventilation synchronized with the heartbeat.

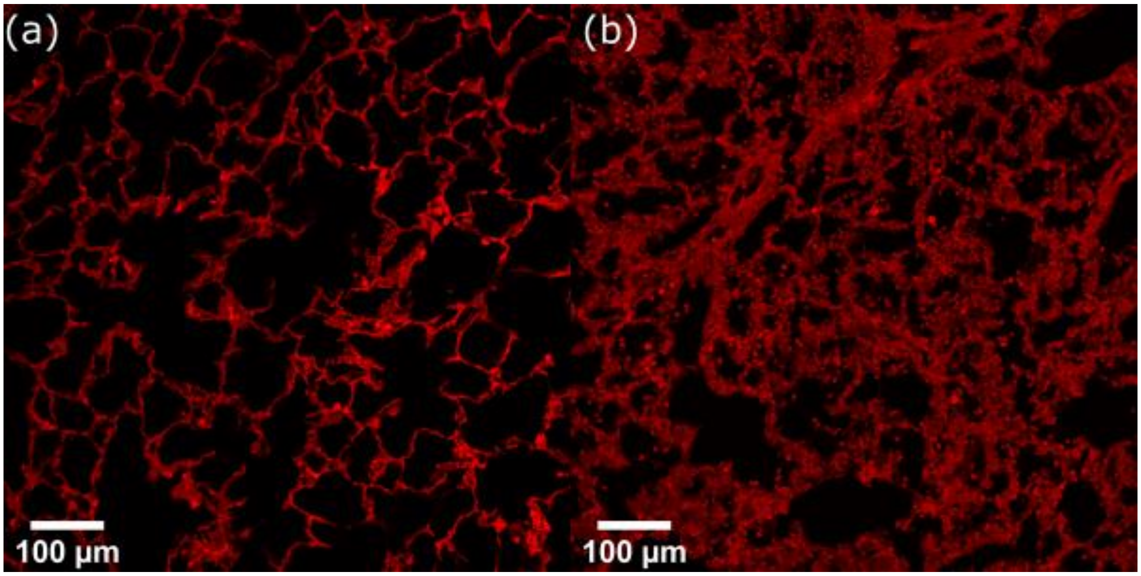

Figure 4-36 Example of staining with defensin 5, targeting neutrophils, for immunofluorescence. In (a) a region considered healthy by the pathologist from rabbit 2; in (b) an injured region from rabbit 3. The staining was not specific and no further quantification of neutrophil infiltration was possible.

The two acquisition protocols proposed are based on the assumption of a periodic motion of the lung parenchyma. A good approximation of periodic motion was obtained in apnea using apneic oxygenation, which allows to maintain a constant pressure in the lungs and stable hemodynamic conditions for several minutes, in the limits shown in Section 4.5.1.1, where a maximum variation in the heart rate of 15% was observed over 5 minutes. When introducing mechanical ventilation instead, a synchronization between the heartbeat and the mechanical ventilator was implemented, in order to have the two sources of parenchymal motion in phase at every breath.

The first protocol allowed to describe quantitatively the cardiogenic motion; the second to visualize and quantify atelectrauma dynamically during a whole breath in a rabbit model of VILI and to correlate it to alveolar damage and neutrophil recruitment.

4.6.1 Comparison to state-of-the-art *in-vivo* dynamic 3D microscopy

The state of the art of *in-vivo* dynamic 3D microscopy was reviewed in Section 2.4.2. With respect to the existing techniques, the pixel size we achieved (22.6 µm, Section 4.2.2) is comparable with the pixel size obtained by Dubsky et al. [10], [83], i.e. 20-15 µm.

The acquisition protocol proposed in this chapter based on apneic oxygenation, allows to study the cardiogenic motion as the technique developed by Dubsky et al. [83] in mice. The main differences with respect to Dubsky et al. [83] are:

- the animal model: a rabbit in this work, mouse in Dubsky;
- the injury model: VILI was introduced in our work, while in the literature only healthy animals were analyzed;
- the ventilation strategy: in our technique the scan is acquired during a single long apnea, while in Dubsky during successive expiratory pauses (Section 2.4.2). Our scan is therefore shorter since, with successive expiratory pauses, the heartbeats occurring during inspiration must be discarded.

Based on our experience and on all the preliminary tests done and shown in Section 4.5.2 and 4.5.6, we can instead conclude that the acquisition protocol based on the synchronization between the heartbeat and the mechanical ventilator is the only existing technique capable of resolving the combined lung motion due to inflation/deflation and heart contraction/expansion.

The only other 3D microscopy technique applied to an *in-vivo* model of VILI is the work by Broche et al. [14], developed at the ESRF within our research team. Unlike the work by Broche et al. [14], based on successive respiratory pauses and without cardiac gating, our acquisition protocol with mechanical ventilation allowed to study the lung parenchyma in dynamic conditions. In order to obtain dynamic conditions, a retrospective gating had to be introduced, thus increasing the acquisition time from the 20 seconds of Broche et al. [14] to 5 minutes (Section 4.2.5). The spatial resolution was however increased from 45 µm to 20 µm. It is important to underline that this increase in spatial resolution and a compensation of motion artefacts could be achieved only at the expense of the short-term information obtained by Broche, who could repeat one scan every 90s visualizing short term recruitment/derecruitment [14]. In our technique a respiratory cycle is reconstructed averaging 1000 ventilator periods (Section 4.2.5): non periodic, short term changes in the lung parenchyma cannot be resolved and result in motion artefacts in the image.

4.6.2 Technical limitations

The main experimental limitation in the implementation of both the acquisition protocols proposed, is the reduced field of view of the detector during image acquisition in the vertical direction: 4 mm, compared to the 57.9 mm of the horizontal direction (Section 4.2.2). Reducing the number of rows read out by the detector was necessary to achieve the high frame rate required by the scan, i.e. 130 fps (Section 4.2.5). This was imposed by: (i) the specific detector used (PCO Edge 5.5); (ii) the maximum speed with which the data could be transferred and saved to the ESRF servers (approximately 130MB/s). A solution overcoming the limitations of our detection system was adopted at the Swiss Light Source: a detector for high speed acquisition was developed at the Paul Scherrer Institute, allowing sustained data acquisition with a frame rate up to 8 GB/s [124], based on the PCO DMax chip and on a dedicated server for data readout. A higher frame rate is now achievable at the ID17 beamline, thanks to an optimized data saving procedure: with the same field of view a frame rate of 500 fps can be obtained, as will be discussed in Chapter 5.

A further limitation concerns the dose delivered to the sample. As discussed in Section 4.2.5, the frame rates required by the two imaging protocols (90fps and 130fps) didn't allow to use the beam shutters available at the biomedical beamline of the ESRF, thus obliging a constant irradiation of the sample. The maximum entrance air kerma found in this work was approximately 200 Gy. This value can be reduced by a factor two due to the fact that the CT was acquired in half acquisition mode and, except for a small volume, each region of the lung was directly irradiated only for one half of the acquisition, obtaining 100 Gy. This dose is comparable to the doses delivered in a full radiotherapy treatment (60 Gy), therefore radiation damages are expected. No significant morphological abnormalities, due to radiation damage, were however identified in the lungs and in histologic sections after the experiment, in agreement with what observed by Lovric et al.[13] at a dose of 90 Gy; immediate radiation damage in soft tissues was reported at doses of the order of 1.5 kGy [71]. Since the animals were sacrificed a few hours after the first dynamic scan, longer term effects of the radiation were not evaluated.

Differently from clinical CT scanners, in synchrotron facilities animals can be mainly studied in upright position. This configuration is different from the one utilized in intensive care units, where patients are ventilated in supine or prone position.

4.6.3 Limitations of the image analysis technique

Concerning the image analysis, for the study of the cardiogenic motion and the quantification of the recruitment/derecruitment, elastic image registration based on a B-spline basis expansion of the transformation was used (Sections 4.3.2 and 4.3.3.1). The main difficulties encountered with this approach were the limited field of view discussed in the previous section, as well as the high deformations to be described with respect to the pixel size.

B-spline based transformations were adequate to describe the cardiogenic motion, but different transformation classes (see Section 2.5.1) could be tested or developed, based on continuum mechanics or on biomechanical models of the lungs, to better describe the parenchymal deformation; the same comment can be extended to the regularization terms. Existing libraries, i.e. ITK and Simple Elastix, were used due to the limited amount of time, but new libraries, optimized for image registration of 3D lung microscopy, could be developed. In the case of the cardiogenic motion, where the displacement field as a function of time is required, a 4D registration technique (Section 2.5.2) would be preferable, due to a smoother estimate of the vector field in the time variable. The implementation of the 4D registration in Elastix was tested, but lacking regularization terms, didn’t provide satisfactory results.

In the case of the mechanical ventilation applied to the VILI model instead, the opening and closing of lung units adds a further degree of complexity, in which the presence of non-corresponding structures has to be taken into account. Image registration was used to realign volumes reconstructed at consecutive time frames, in order to identify recruitment and derecruitment based on a voxel by voxel comparison of the lung parenchymal density (see Section 4.3.3). When considering a voxel by voxel comparison, we can’t claim that we can identify with a precision of a few voxels where the opening and closing actually occurred, due to the impossibility of finding a one-to-one correspondence between opening and closing structures during image registration. We can claim however that there is a higher probability of finding a change in status around the region where atelectrauma is occurring.

4.6.4 Cardiogenic motion of the lung parenchyma

Elastic image registration applied to the acquisition protocol in apnea, allowed to determine the displacement vector field of the lung parenchyma as a function of time along the cardiac cycle in healthy and injured conditions. One possible application is the study of the mechanical properties of the lungs in healthy and injured conditions. Heartbeat, vessel pulsatility and muscular activity have been used, for example, to estimate the elastic properties of biological tissues with ultrasounds, a technique called Passive Elastography. The principle behind it is to identify the low-speed shear waves originated by the cardiac pulsations (or breathing) and to estimate the velocity of propagation, proportional to the Young's modulus of the tissue [125]. This can be achieved knowing the displacement field as a function of time. Evaluating the mechanical properties, known to be heterogeneous in the lungs, and correlating them to the development of VILI could be a future development and application of this technique.

The evaluation of a further analysis based on passive elastography is foreseen: what should be estimated, when detecting the shear waves, is the contamination between phases of the parenchymal motion, due to the non-perfect periodicity of the heartbeat (Section 4.5.1) and the unknown relation between the ECG and the heart contraction, coupled to the uncertainties raised by the QRS detection algorithm. A small difference in phase could be introduced in between heart cycles, producing a phase mix in the reconstruction. Artefacts could moreover be introduced by non-periodic components of the cardiogenic motion. The long apnea under pure oxygen is known to induce atelectasis [126].

4.6.5 Quantification of atelectrauma

When applied to the mechanical ventilation, image registration allowed to realign consecutive frames of the motion and to obtain a quantitative estimate of the recruitment and derecruitment as a function of time, by a voxel by voxel comparison of the density of the lung parenchyma (Section 4.3.3). As expected, an excess of recruitment over derecruitment was found during inspiration and an excess of derecruitment over recruitment during expiration (Section 4.5.6). However, a high background signal was identified, due to the low signal to noise ratio in the images and to the non-perfect image registration, which was not precise at the level of a single pixel, introducing artefacts mainly at the edges of blood vessels and large airways (Section 4.3.3.2and 4.5.6). This noise was reduced with a morphological opening, removing all the smallest volumes identified as recruited or derecruited.

The curves representing the recruitment and derecruitment fractions as a function of time (Section 4.5.6) show heterogeneity in the tracheal pressure at which different airways open and close, in a single animal and in between animals. Peculiar, in our dataset, is the case of Rabbit -5, for which two main peaks in the recruitment were identified during inflation, centered at~10 cmH_2O and~20 cmH_2O, and two peaks of derecruitment were identified during deflation, at~15 cmH_2O and~8 cmH_2O.

The complexity of the pressure and time dependency of recruitment and derecruitment can be interpreted considering mathematical models of airway opening and closing present in the literature, for example in the works by Broche, Bates and Smith [14], [53], [127]. In these models a closed lung unit reopens, with a finite speed, once the pressure in the subtending airway increases above a critical opening pressure and closes once the pressure goes below a critical closing pressure. A critical opening and closing pressure and a critical opening and closing speed, is assigned to each airway following a user defined statistical distribution. In this theoretical framework, the rate of recruitment and derecruitment present in our data would depend therefore on the tracheal pressure, on the distribution of the critical opening and closing pressures of the airways (Section 1.2.2), on the finite speed of opening and closing and on their distribution. Values of opening and closing found in the aforementioned publications for the acini are 5 cmH_2O for a healthy lung and 10 cmH_2O to 18 cmH_2O in injured lungs, not far from the values observed. A direct comparison is however difficult since, unlike the previous works which consider deep slow inflations [53], [127], our approach considers a normal respiratory rate.

Figure 4-26 Figure 4-32 show the coexistence of recruitment and derecruitment during the whole respiratory cycle. The presence of recruitment during expiration could be interpreted, in the framework of the aforementioned mechanical model, considering the finite opening speed of the airspaces: opening could have started during inspiration, to be completed and detected during expiration. The mechanical interdependence of the alveoli modifies moreover dynamically the opening and closing pressure of small airways and alveoli. Coexistence of recruitment and derecruitment was early observed by Broche and reproduced introducing mechanical interdependence in a mathematical model of airway opening and closure [14]. Due to the noise in the image reconstruction and to the limitations in the detection of airway opening and closure discussed in Section 4.6.3, it was however not possible to visualize dynamically the recruitment and de-recruitment of a given airway. No conclusions can be drawn therefore at this resolution on the airway opening/closing mechanisms or speed.

Local variations in pressure between neighboring lung regions could induce interregional airflows through airways, an effect known as *pendelluft,* or through collateral channels, an effect known as *collateral ventilation*. The latter is in particular well documented in rabbits. These phenomena were not directly observed in our dataset but, if periodic, would contribute to the presence of alternating recruitment and derecruitment of neighboring airspaces.

A final remark concerning the results is that, even if PEEP is applied in clinics to reduce atelectrauma, the maximum derecruitment was observed (Section 4.5.6) at high pressures, greater than 10 cmH_2O, implying that even moderate to high PEEP levels may not completely avoid atelctrauma.

4.6.6 Correlation between atelectrauma and histological analysis

Atelectrauma was positively correlated with alveolar damage and neutrophil infiltration (Section 4.5.7) in our injury model based on whole lung saline lavage and injurious ventilation. Our results demonstrate for the first time, that atelectrauma at the microscopic length scale is associated with increased cellular infiltration, a hallmark of inflammation. Alveolar damage was studied with a blinded qualitative evaluation of a pathologist, taking into account alveolar disruption, neutrophil infiltration and hyaline membranes. A positive correlation was found between the alveolar damage and the presence of atelectrauma in the dynamic CT (Section 4.5.7.1). Automatic cell counting based on HES stained slices (Section 4.5.7.2) allowed instead to demonstrate that in our model neutrophil infiltration is spatially correlated with atelectrauma.

Further studies based on immunofluorescence were attempted, to identify IL-6, IL8, Def5, RAGE (Section 4.5.7.3). These studied did not produce meaningful results, due to the difficulties encountered in obtaining a specific staining. Only a few antibodies are available on the market to mark rabbit tissue. The injury model introduced moreover is an early model of VILI. The animals are imaged and sacrificed shortly after the development of the injury: a short time is available for the consolidation of the injury and of the inflammatory response. The injury was mostly evaluated by the pathologist as mild.

4.6.7 Future perspectives

The acquisition protocols developed in this Chapter allowed to: (i) visualize the dynamics of the lung parenchyma during mechanical ventilation; (ii) spatially correlate histological analysis to lung micromechanics. In this work dynamic 3D microscopy was utilized to study atelectrauma, without focusing on overdistension and volutrauma. Developing a protocol to detect overdistension, based on the distribution of the gray levels or on the regional volume variation provided by the image registration, would therefore yield complementary information to the results presented in this Chapter (Section 4.5.6). The presence of overdistention is suggested by the concavity of the pressure-time curve in Figure 4-32. In a work by Ranieri et al [128], a positive concavity was associated to overdistension and is visible in Figure 4-32 towards the end of inspiration; a negative concavity was associated to recruitment and a linear pressure-time curve to normal inflation. The relationship between concavity and overdistension (stress index) was found however by Ranieri et al. during inflation with constant air flux, a condition not met in our study.

A possible development in the correlation between lung micromechanics and histological analysis is instead the study of the collagen microstructure. It is known that VILI produces, when consolidated, lung fibrosis. An attempt of studying alterations in the collagen microstructure through Fourier Transform Infrared Spectroscopy (FTIR) is currently under evaluation.

An analysis of the airway diameter as a function of time during the breathing cycle in a rabbit model of VILI is moreover ongoing, extending a recent work by Broche et al. [129], based on the comparison between successive respiratory pauses.

A further development of the technique towards higher resolution was achieved and will be the topic of the next chapter. This technique will allow to study the dynamics of the lung parenchyma at the alveolar scale during mechanical ventilation, possibly giving the first direct experimental observation of the alveolar deformation during a breathing cycle.

5 IN-VIVO DYNAMIC 3D MICROSCOPY: TOWARDS THE ALVEOLAR SCALE

5.1 INTRODUCTION

The dynamic CT technique described in Chapter 4, allowed to estimate the cyclic recruitment and derecruitment of lung units *in-vivo*, in an early stage of VILI, and to describe quantitatively the cardiogenic motion of the lung parenchyma. The main limitation of the technique was the pixel size (Section 4.2.2), which didn't allow to study the lung deformation at the alveolar scale. As discussed in Chapter 1, one of the main limitations in the study of VILI is the absence of a direct visualization *in-vivo* of the alveolar deformation during mechanical ventilation. An *in-vivo* imaging technique, capable of resolving single alveoli in dynamic conditions in a VILI model, would provide information on the mechanical strain of alveolar walls during the breathing cycle and on the mechanisms through which recruitment/derecruitment occurs [129]. In a healthy animal model, it would allow to address open questions in physiology, for example the mechanism of lung acinar inflation and deflation, which could occur through alveolar recruitment and derecruitment [130] or through an increase in the diameter of the alveolar ducts and alveoli [131].

In Chapter 2 (Section 2.1) it was discussed how X-ray CT is presently the only experimental technique which can achieve a spatial resolution sufficient to study the lung parenchyma *in-vivo* at the level of terminal airways and alveoli. As already introduced in Chapter 1, the thickness of the alveolar walls, considering the blood gas barrier and the size of the capillaries, is of the order of 10 µm, therefore a pixel size lower than 3 µm should be used. Due to the challenges of *in-vivo* lung CT, reviewed in Section 2.3.2 (periodicity of the lung motion, high X-ray flux required, radiation dose constraints), this resolution was successfully applied in imaging an *in-vivo* mouse model only by Lovric et al. [13] at the Swiss Light Source (SLS, Paul Scherrer Institute, Switzerland); this achievement was made at the expense however of dynamic information: only one cardiac phase was acquired and reconstructed per scan at a constant airway pressure.

The goal of this project was to develop a CT technique, capable of resolving the motion of the lung parenchyma at the alveolar scale, while preserving the dynamic information. Several experiments were initially performed to develop this technique using a 3 µm pixel size. Even though further efforts will be needed to achieve high quality images using the aforementioned resolution, tomographic images were acquired in a healthy rat model using a pixel size of 6 µm. To our knowledge this is the first time that such a resolution is obtained *in-vivo* in a dynamic scan. Even if this resolution is insufficient to study the alveolar walls, terminal airways and acini can be clearly distinguished and their deformation during the respiratory cycle is under evaluation.

In this Chapter, the main approaches leading to the development of the technique will be presented, trying to analyze the main experimental limitations which have so far hindered the development of an *in-vivo* dynamic CT technique at higher spatial resolutions.

5.2 PROSPECTIVE GATING WITH MONOCHROMATIC RADIATION

The first approach used to develop a high resolution *in-vivo* dynamic CT was based on prospective heart gating (Section 2.3.1), applied to a healthy rabbit model and using a detector pixel size of 3 µm. To reduce the complexity of the project, it was initially decided to acquire a CT at a single heart phase and at constant tracheal pressure. The aim of the project was therefore to reconstruct a single volume free from motion artefacts, in which alveoli could be distinguished: we believed this was a necessary condition before targeting dynamic information. Among the advantages of prospective over retrospective gating, as discussed in Section 2.3.1, two should be emphasized: (i) the higher time resolution, determined by the integration time of a single projection, and (ii) the dose efficiency: the low acquisition rate (3 Hz in a rabbit model, considering one projection per heart cycle) allowed the use of X-ray shutters, avoiding unnecessary exposure of the sample in between projections.

5.2.1 Prospective gating: ct acquisition scheme

The approach proposed in this section was based on a "step and shoot" CT scan. In this image acquisition modality, projections are acquired only when the sample is stationary. The rotation is not continuous and is performed after each projection is acquired. This method is preferred to the one based on continuous rotation when the deterioration of the spatial resolution, due to the rotation of the sample during the integration time, has to be avoided. The logic behind our approach was to perform a CT scan in "step and shoot" modality, imposing the additional condition that projections could be acquired only during an expiratory pause (at PEEP) and synchronized with the ECG.

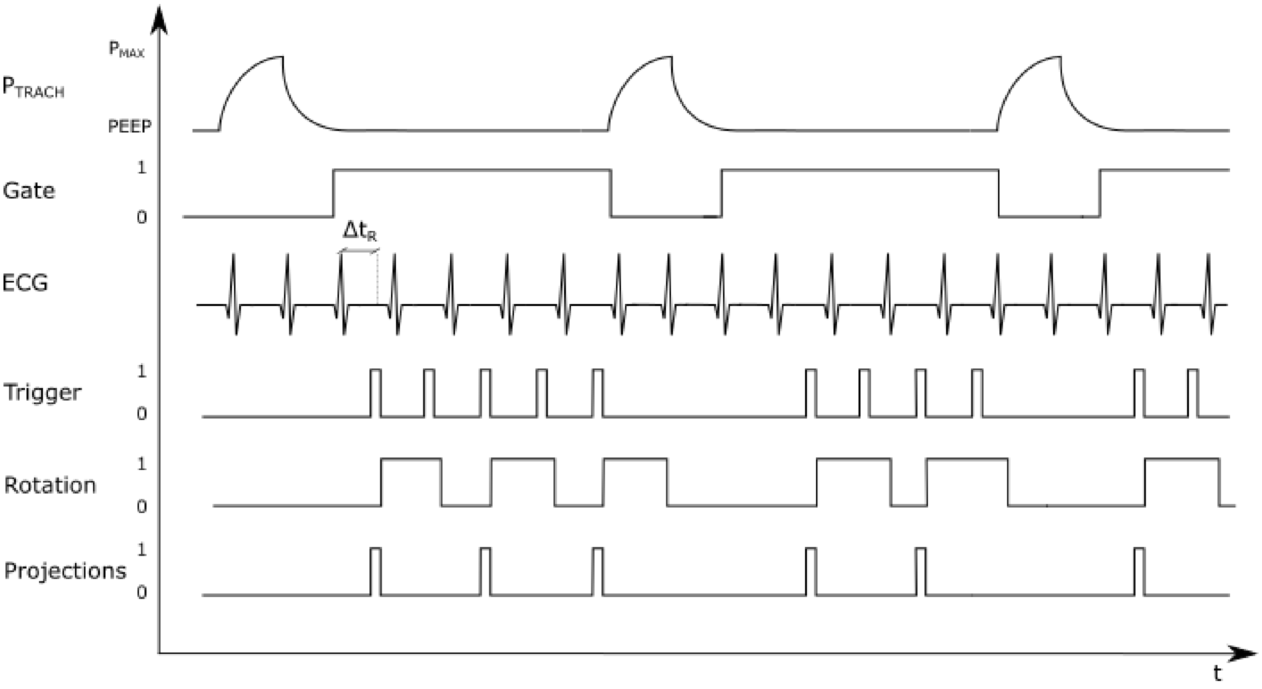

Figure 5-1 General scheme of the acquisition with prospective gating. Projections are acquired during a respiratory pause at the end of expiration. When P_{TRACH} *is equal to the PEEP level, the logic Gate signal is raised (from 0 to 1), thus enabling the polling on the ECG. At every R peak detected, a trigger is generated, with a user chosen delay* Δt_R*.The trigger is sent to the detector if and only if the sample is stationary (Rotation = 0), according to the rules of the "step and shoot" CT modality, and a projection is then acquired.*

To implement this additional condition, the scheme represented in Figure 5-1 was adopted. A gate signal was raised to the logical value of 1, when the tracheal pressure reached the PEEP and was lowered to a logical value of 0 at the beginning of the following inspiration. Every QRS complex occurring when the gate level was 1 generated a trigger with a user defined delay from the R peak (Δt_R), which allowed to select the phase of the heart cycle. A trigger generated by a QRS complex was sent to the detector if and only if the sample was stationary, triggering the acquisition of a projection, and the successive rotation of the sample. Not all the heart beats corresponded therefore to a projection.

Successive respiratory pauses were preferred to a single long apnea to obtain the most stable hemodynamic conditions. Using this scheme, several parameters may affect the quality of the scan:

- **Ventilator**: important factors are the duration of the expiratory pause, the lung pressure stability and the PEEP level. The pressure stability during the expiratory pause depends in general on its duration and on the properties of the mechanical ventilator.
- **Heart**: One of the most important parameters is $\Delta t_R,$ which selects the heart phase. The best image quality is expected when the cardiogenic motion of the lung parenchyma is small. This condition occurs at the end of the cardiac cycle during the diastolic phase, as shown in Section 4.5.5. Other parameters potentially affecting the quality of the scan are the heart rate and its stability, the latter being influenced by the duration of the expiratory pause.
- **Detector**: the integration time per projection determines the time resolution of the acquisition protocol.
- **Region of interest**: the cardiogenic motion is weaker in the dorsal and peripheral lung regions, as shown in section 4.5.5, and depends on the gravitational level.

5.2.2 Prospective gating: experimental setup

The technique described in the previous paragraph was implemented and tested in the experimental hutch of the satellite building (EH2, Section 3.2.1 and 3.2.3) on five New Zealand white adult rabbits. Propagation based phase contrast imaging was used, setting the propagation distance to 1.5 m. The PCO camera was utilized, coupled to a 350 µm thick YAG scintillator and an optics giving an effective pixel size of 3.06 µm. The camera was operated in global shutter mode (Section 3.3.1), to maximize the signal to noise ratio, with the largest field of view available (2560 × 2160 pixel). Fast X-ray shutters were synchronized with the camera, to avoid unnecessary irradiation of the sample in between projections. A monochromatic beam of 55 keV was selected using the double Laue monochromator. X-ray dosimetry was not performed at this initial stage of the project: since monochromatic radiation was used and the X-ray shutters were synchronized with the acquisition, the possibility of immediate radiation damage was excluded.

The physiological instrumentation was described in Section 3.3.4. Both the custom-made mechanical ventilator and the Flexivent were used during the data acquisition. The Flexivent allows to obtain a higher pressure stability but a shorter expiratory pause duration with respect to the second ventilator. The electronics interfacing detector, mechanical ventilator, ECG recording system and rotation stage was not developed during this Thesis work. For this reason, only the implemented logic was described in Figure 5-1.

5.2.3 Prospective gating: animal preparation

The animals were anesthetized by intramuscular injection of Ketamine (15 mg/kg) (Ketamine 1000, Virbac, France) and Xylazine (5 mg/kg) (Paxman, Virbach, France). A 24-G catheter (Venflon, BD, Franklin Lakes, New Jersey, USA) was placed in the marginal ear vein. Anesthesia was maintained by infusion of Ketamine (30 – 60 mg/kg/h) (Ketamine 1000, Virbac, France) and Xylazine (3 – 6 mg/kg/h) (Paxman, Virbach, France). The animal was tracheostomized and a 3.5-F polyethylene catheter was inserted in the trachea (Portex, Smiths Medical, Minneapolis, Minnesota, USA). A 24-G catheter was placed in the central ear artery, to monitor blood pressure. After surgery the animal was immobilized in a custom-made plastic holder, placed in the experimental hutch, and mechanical ventilation was initiated. After verifying the depth of anesthesia based on the corneal reflex, muscle relaxation was induced by infusion of atracurium (0.6mg/kg/h) to avoid motion and suppress spontaneous breathing. At the end of the experiment the animal was euthanized by IV injection of pentobarbital sodium (220 mg/kg).

5.2.4 Prospective gating: experimental protocol

Successive tomographic scans were performed, following the acquisition scheme presented in section 5.2.1. In each scan, one of the following parameters was modified: (i) Δt_R; (ii) PEEP; (iii) the duration of the expiratory pause. Several PEEP levels were used, ranging from 0 cmH_2O to 12 cmH_2O; the duration of the expiratory pause was varied from 1.5 s to 5 s; Δt_R was selected from 0 ms to the duration of the heart cycle (300 ms to 400 ms on average). 1000 equally spaced projections were acquired per scan: the duration of the scan, depending on the apnea and on the heart rate, was approximately 20 minutes. The integration time per projection was set to 10 ms, as a compromise between time resolution and signal intensity. On average 500 counts per pixel were obtained at 10 ms integration time, equal to five times the integrated electronic noise, and low with respect to the 16 bit dynamic range of the detector (see section 3.3.1).

In order to check the impact on image quality of successive respiratory pauses and long scans, one shorter dynamic scan with apneic oxygenation (Section 4.2.1.1) was acquired, while keeping the same experimental conditions described above. An integration time of 10 ms was therefore used, coupled to a frame rate of 100 fps. The dynamic scan was acquired over a single 180^o rotation, at a constant tracheal pressure of 10 cmH_2O and had a total duration of 4 minutes.

5.2.5 Prospective gating: results

Despite the different parameters tested, concerning the PEEP value, the duration of the expiratory pause and the delay from the R wave (section 5.2.4), a CT free from motion artefacts, in which alveoli were visible, couldn’t be obtained with the prospective triggering. An example of CT reconstruction is visible in Figure 5-2 (a): some of the largest structures, for example blood vessels and a lung fissure, are visible, even if blurred; alveoli however cannot be distinguished. This image was acquired using the Flexivent set to a PEEP of 6 cmH_2O and at a delay of 245 ms from the R wave. An expiratory pause of 1 s was utilized, following an inspiratory time of 0.3 s and an expiratory time of 0.7 s, resulting in a respiratory rate of 30 breaths per minute. This reconstruction is representative of the image quality with all tested parameters. Figure 5-2 (b) represents a *post-mortem* CT acquired at a PEEP of 12 cmH_2O. In this reconstruction alveoli can be distinguished mainly due to the presence of edema, which appears rapidly post-mortem. The results of the dynamic scan with apneic oxygenation is shown in Figure 5-2(c). It was reconstructed in diastolic phase, at the end of the cardiac cycle. As in (a), alveoli are not visible and blood vessels are blurred.

5.2.6 Prospective gating: discussion

Several factors were identified, which could have hindered the visualization of the alveoli in the image reconstruction. These include lung tissue stability, animal model and maximum time resolution achievable.

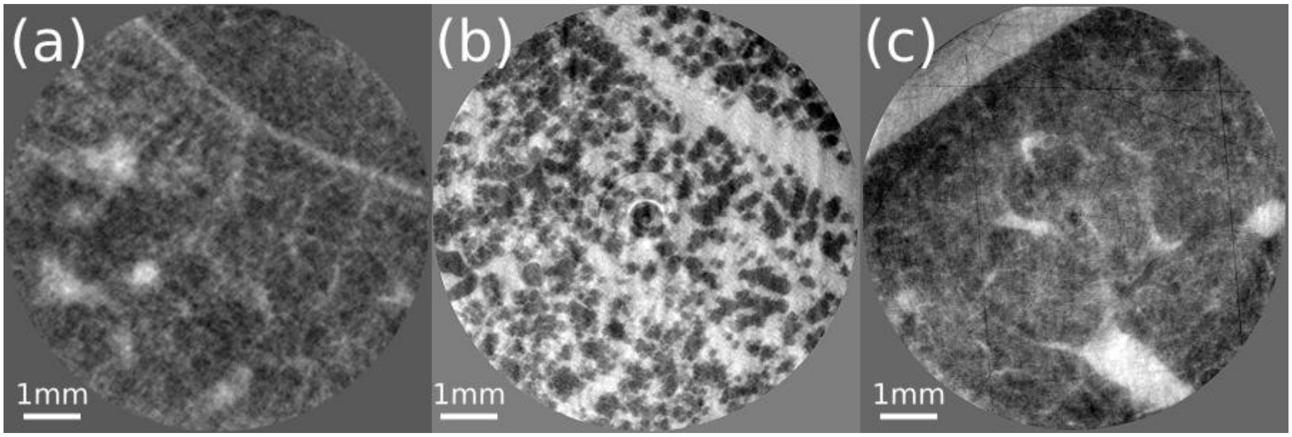

Figure 5-2 Example of rabbit's lung CTs acquired with monochromatic radiation (55 keV) and with the 3 µm optics. (a) CT acquired in-vivo with prospective triggering and successive respiratory pauses. (b) CT acquired post-mortem at a pressure of 12 cmH_2O. (c) CT acquired with the dynamic technique described in Chapter 4 and apneic oxygenation. (a) and (b) were acquired using the same rabbit. Despite the optimization protocol described in this section, alveoli can't be visualized in the in-vivo images.

Concerning the lung stability, the main limitation is the long acquisition time: as previously stated the duration of the scan was of approximately 20 minutes and involved consecutive lung inflations and deflations. In order to test shorter scans, the dynamic scan with apneic oxygenation, described in Chapter 4, was applied: the advantage of this approach is that it was similar to the successful acquisition protocol proposed by Lovric et al [13] in a mouse model, which was based on a single long apnea. The image quality was however not improved with respect to the prospective triggered acquisitions, and the alveolar motion was still not resolved. The fact that two different ventilation strategies, one of which was shown to be successful in a mouse model, produced a similar image quality, suggests that the main limitations of the study may have been the animal model and the time resolution achieved.

The rabbit animal model is different from the animal models previously used in high resolution lung CT, i.e. mice and newborn rats. The challenges introduced by a larger animal model such as the rabbit may be the higher absolute variation in lung volume and the higher parenchymal displacement induced by the heart motion. If the motion is greater in amplitude, alveolar structures may not return exactly to their initial position after each inspiration or heartbeat at a 3 µm precision.

The low time resolution was related to the flux available in the second experimental hutch of ID17 at 55 keV: an integration time lower than 10 ms could not be applied (too low flux rate, determining too noisy images), while an integration time lower than 3 ms would have been needed, according to the data of Lovric et al. [70].

It is finally important to notice that, even if alveoli can be distinguished in the CT acquired *post-mortem* (Figure 5-2(b)), the reconstruction is characterized by a high level of noise. A partial degradation in image quality could be due to motion artefacts, which are present even post-mortem due to the slow physiological changes occurring after death. The optical system and the choice of scintillator should be moreover optimized.

To increase the radiation flux and remove the constraints on the integration time, imaging in pink beam (polychromatic radiation) was performed. The animal model was moreover modified, moving from New Zealand Rabbit to the smaller adult OFA rat model.

5.3 PINK BEAM IMAGING

A tomographic setup for performing imaging with pink beam was developed during the first year of this Thesis, as described in Mittone et al [106]. This setup is located in the first experimental hutch (EH1) of the beamline and was described in Section 3.2.2. It was developed specifically for high resolution applications (pixel size <3 µm), in order to overcome the flux limitations of the monochromatic imaging setup (EH2), as discussed in the previous section. These limitations were due to the fact that the ID17 beamline (OH2 and EH2) was originally designed for low resolution imaging applications (pixel size >350 µm) [104]. Since the aim of the project was to perform *in-vivo* tomography with a pixel size of 3 µm, the pink beam imaging setup was tested for *in-vivo* applications in a rat model. The particularity of this setup is that the X-ray flux is more than three orders of magnitude larger than in the monochromatic setup, possibly inducing immediate radiation damage. An X-ray shutter synchronized with the camera and with the ECG of the animal was not available in the first experimental hutch (EH1); in order to minimize the exposure time and therefore the dose delivered to the sample, the fastest scan available at the beamline was tested: the dynamic scan with apneic oxygenation.

5.3.1 Pink beam imaging: experimental setup and dosimetry

In-vivo lung imaging with pink beam was performed in the first experimental hutch EH1 (see Section 3.2.2), on a rat model. The detector used was the PCO coupled to a 50 µm LuAG scintillator and to an optics giving a pixel size of 3.5 µm. The sample to detector distance was set to 2 m. The wiggler's gap was set to 68 mm for w150 and to 200 mm for w125. The following filters were utilized: 1.15 mm of Carbon, 1.52 mm of Aluminum and 0.69 mm of Copper.

The implementation of the apneic oxygenation used the same experimental setup described in Section 4.2.3. For baseline ventilation, the Flexivent ventilator was utilized.

Dosimetry was performed using a PinPoint ionization chamber TW31014 (PTW, Freiburg, Germany), associated to a UNIDOS Webline TW10022 electrometer (PTW, Freiburg, Germany). Camera and Electrometer were calibrated and certified by PTW-Freiburg. Due to the laminar beam, the ionization chamber was not fully irradiated during the measurement. The scanning technique developed by Prezado et al. [114] was therefore used. With the aforementioned wiggler's opening and filters, and an electron beam current of 200 mA the measured entrance dose rate at the sample position was ~ 1.5 kGy/s.

5.3.2 Pink beam imaging: animal preparation

The pink beam imaging setup was tested on three OFA rats (Weight = 400 ± 20 g). The animals were anesthetized using isofluorane 4% (Isoflo, Zoetis, France), followed by intraperitoneal injection of Ketamine (10 mg/kg) (Ketamine 1000, Virbac, France) and Xylazine (5 mg/kg) (Paxman, Virbach, France). The animals were tracheostomized and a 14G catheter was inserted in the trachea. After the surgery, the animals were immobilized in a Plexiglas tube. The animals were then taken to the experimental hutch and mechanical ventilation was initiated. Anesthesia was maintained by inhaled Isofluorane 1.5% (Isoflo, Zoetis, France) administered throughout the experiment. After insuring adequate depth of anesthesia based on the response to manual paw compression, atracurium (0.6 mg/kg/h) was administered to avoid spontaneous motion and repeated every hour. When imaging was not performed, the rats were ventilated using a peak pressure limited to 30 cmH_2O, and a V_T of 10 ml/kg. A respiratory rate of 90 breaths per minute was set, with inspiratory-expiratory time ratio of 1:2.

5.3.3 Pink beam imaging: experimental protocol

For pink beam imaging, the acquisition protocol of the dynamic scan with apneic oxygenation described in Section 4.2.1.1 was partially modified. CT was acquired over 180º, thus avoiding the half-tomography approach: this choice allows to divide the number of required projections, and therefore of required ECG cycles by a factor of 2 with respect to half-tomography, once the angular sampling is fixed. The acquisition time of the scan and the total dose delivered to the sample are accordingly reduced.

Two integration times were tested: 4 ms and 2 ms; the interval between two consecutive projections was respectively of 6 ms and 4 ms. The maximum frame rate was therefore 250 fps, associated to a field of view of 2560 × 201 pixels (Horizontal × Vertical). This frame rate was twice the maximum frame rate achieved when scanning at 20 µm pixel size, thanks to an optimized data transfer procedure to the servers developed by the Beamline Control Unit of the ESRF. The angular speed of the rotation was computed, given the heart period, to acquire approximately 750 heart cycles per tomography. In an anesthetized rat a total scan duration of 3.5 to 4 minutes was required.

During the tests, 1 to 3 dynamic scans were acquired per rat. The number of scans was depending on the survival of the animal: the rat was dying due to the radiation dose during the last scan or a few minutes after it. Several tracheal pressures were tested, ranging from 7 to 14 cmH_2O, in order to modify the lung compliance and therefore the parenchymal displacement induced by the cardiac activity and to assess acinar deformation. Different regions of interest were moreover chosen, above and below the heart. Direct irradiation of the heart at this dose rate caused in fact systematically the death of the animal during the scan. To select the region of interest, a fast CT was acquired in apnea, at the same pressure foreseen for the dynamic scan, but without heart gating. The average duration of this fast CT, which will be referred to as *scout CT*, was of 15 s, non-negligible when compared to the dose rate; the number of projections acquired was 1000 with an integration time of 15 ms.

5.3.4 Pink beam imaging: results

An example of CT images obtained with the dynamic CT acquisition coupled to pink beam imaging is shown in Figure 5-3 (b). Strong motion artefacts are visible. A large airway and the rib, the latter expected to be stationary at a stable pressure, are affected as well. Similar motion artefacts were visible in all the dynamic scans performed, independently from the integration time and the tracheal pressure, and did not correspond to variations in the tracheal pressure recorded during the CT acquisition. Figure 5-3 (a) and (c) show instead two fast scout CTs acquired respectively before and after the dynamic scan shown in (b), without varying the sample position: the region of interest irradiated was in this case at the apex of the lung. These two fast CTs were acquired in apnea without heart gating. Motion artefacts are small. In Figure 5-3 (a) in particular, small airways are visible thanks to the fact that the cardiogenic motion of the lung parenchyma induced in the apex of the lung, far from the heart, was weak.

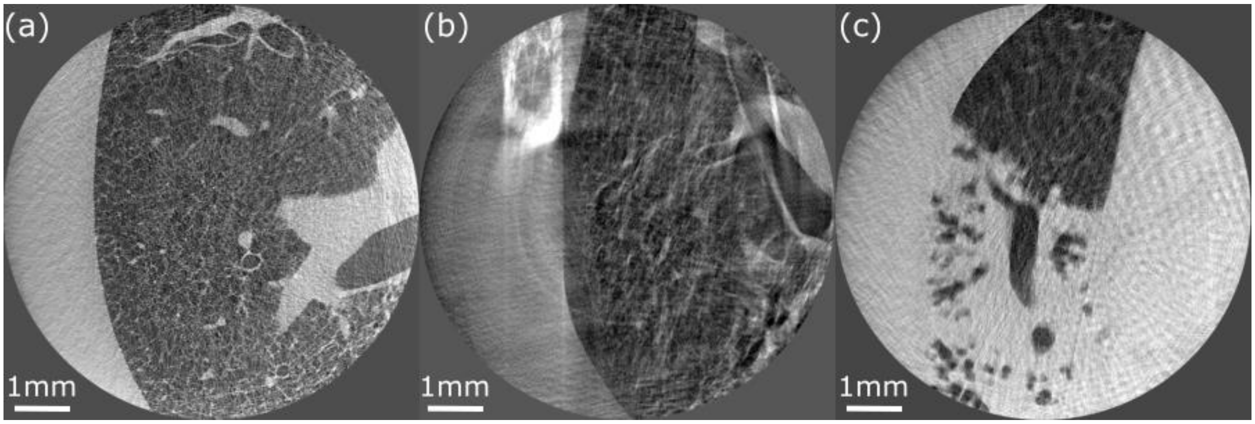

Figure 5-3 (a) Scout CT (see Section 5.3.3) acquired in-vivo without gating, used to identify a ROI for the gated acquisition. (b) Dynamic CT acquired in apnea (c) Scout CT acquired in-vivo on the same position as (a) and (b) after the dynamic acquisition. The strong motion artefacts in (b) and the difference between (a) and (c) show the radiation damage and the sample motion induced during the dynamic scan. All the images were acquired with a constant tracheal pressure of 14 cmH_2O.

5.3.5 Pink beam imaging: discussion

The higher image quality of the ungated (scout) scans compared to the heart-gated scan could be due to two reasons: (i) the lung instability during the 4 minutes apneic oxygenation, and (ii) the effects of the radiation dose delivered to the sample. The predominant source of motion artefacts in pink beam imaging was most likely the second, i.e. the tissue deformation induced by the radiation dose. An entrance dose of 370 kGy was in fact delivered during a 4 minutes scan. Comparing Figure 5-3 (a) to Figure 5-3 (c), acquired as previously stated on the same level, it is in fact possible to notice the appearance of edema after the dynamic scan, indicative of radiation-induced lung injury. The time interval between the dynamic scan and the following scout scan was 10 minutes. A histological examination of each one of the three rats was performed after imaging and confirmed radiation damage, visible already on the outer surface of the lung where the beam was impinging. Considering the cumulative dose of all the dynamic scans and the scout CTs performed in one animal, the minimum radiation dose delivered to an animal was 1 MGy

In conclusion, the pink beam imaging setup is not compatible with *in-vivo* applications. Post-mortem applications were tested and will be the subject of the next paragraph. The image quality of Figure 5-3 (a) however, with small airways visible without synchronization, suggests that the adult rat is a good model for high resolution *in-vivo* lung imaging. A new attempt was therefore made using monochromatic radiation, in order to reduce the dose, and decreasing the pixel size to 11 and 6 µm, in order to overcome the flux limitations found in Section 5.2.

5.3.6 Pink Beam Imaging: Post-Mortem Applications

Even if the pink beam imaging was not compatible with *in-vivo* high-resolution imaging applications, it is interesting to add a short appendix to this section on the image quality achievable *post-mortem.*

Two samples were imaged during the commissioning phase of the pink beam imaging setup: a rat lung, in-situ, and a human lung sample embedded in paraffin. The rat lung was acquired with a pixel size of 3 µm. The animal was prepared with the surgical procedure described in section 5.3.2. The experimental setup is the one described in section 5.3.1. A CT was acquired, with 2000 projections and an integration time of 8 ms. The global acquisition time was 28 s. The result of the image reconstruction is shown in Figure 5-4. The CT was reconstructed applying the Paganin's filter (Section 2.2.3). No further pre-processing or post-processing was performed. The visibility of the alveoli is here increased by the presence of edema in the alveolar space due to the radiation damages of the *in-vivo* scans, as well to the natural postmortem changes of the lung.

The second sample imaged was a human lung sample embedded in paraffin. The sample was prepared by a pathologist at the University Hospital in Grenoble, and cut into a $20 \times 20 \times 20\ \text{mm}^3$ block. It was acquired in half-tomography approach with 3000 projections and 200 ms of integration time per projection. The spectrum of the incident beam was peaked at 40 keV. The

PCO was coupled to the 0.7 µm optics, with 1.2 m of sample to detector distance. The result is shown in Figure 5-5 (a). Figure 5-5 (b) represents a microphotography of an HES-stained healthy human lung tissue, provided by the Grenoble University Hospital. From the comparison we notice the quasi-histological level of detail visible in the pink beam CT image.

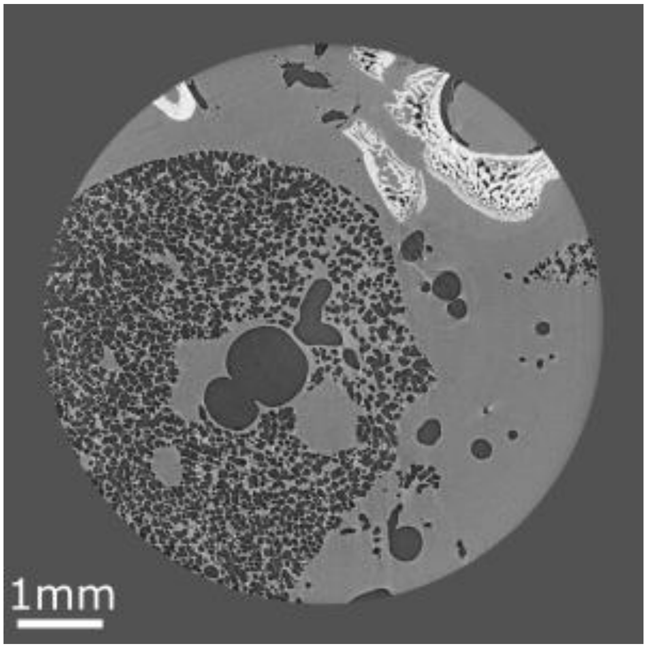

Figure 5-4 CT of rat lung acquired with a pixel size of 3 µm post-mortem. Edema is visible inside the lungs, due to the post-mortem acquisition and to the radiation damage. Motion artefacts are visible in the image due to the slow collapse of the lungs post-mortem. No pressure was applied to keep the lungs inflated.

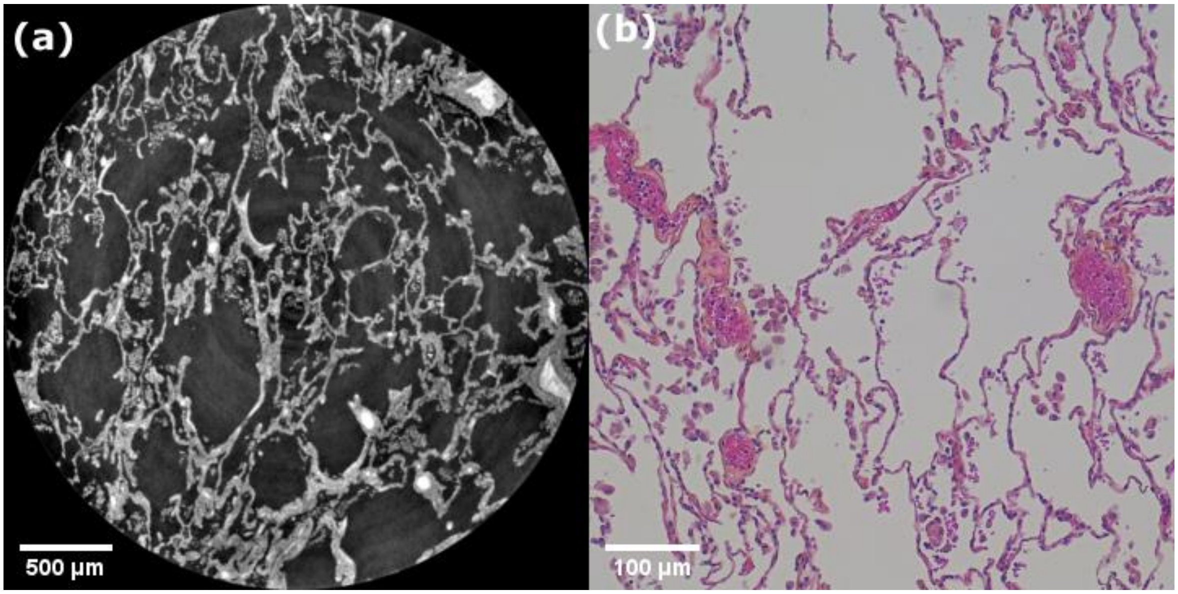

Figure 5-5(a) High resolution CT of a paraffin embedded human lung tissue acquired at 0.7 µm pixel size. (b) Comparison with a microphotography of an histological section (HE staining) of a healthy human lung tissue. Blood vessels, alveolar walls, red blood cells and alveolar macrophages inside the alveolar spaces are visible in the CT, highlighting the histological quality obtained with this imaging setup.

Among the structures clearly visible in the CT there are blood vessels, the capillaries lining the alveoli and red blood cells and alveolar macrophages inside the alveolar spaces.

5.4 MONOCHROMATIC RADIATION IMAGING AT 11 µM AND 6 µM PIXEL SIZE

The low flux available with monochromatic radiation, and the high radiation dose rate with the pink beam imaging setup, incompatible with *in-vivo* imaging, led to the conclusion that *in-vivo* imaging with a pixel size of 3 µm couldn't be achieved at the current status of ID17 in animal models such as an adult rat or a rabbit. The last approach used in this Thesis work was based therefore on monochromatic radiation, relaxing the requirement on spatial resolution. In particular, the two intermediate pixel sizes available at the beamline were tested: 11 µm and 6 µm. The rat model was preferred to the rabbit model, due to the smaller size and therefore absolute cardiac-induced regional tissue displacement. The lower attenuation compared to a rabbit, allowed to use lower energies, with an increase in the flux available. The retrospective gated dynamic CT techniques developed during this Thesis work allow to obtain dynamic information and were the most used acquisition techniques in the laboratory at the time of this study. For this reason, they were preferred to the prospective gating approach described in section 5.2.1.

5.4.1 11 µm and 6 µm pixel size imaging: experimental setup

The two retrospective gated techniques described in Section 4.2.1 were tested in a rat model in the satellite building of ID17, in particular with the setups available in the two hutches OH2 and EH2. The tomography was acquired using the paleostage (Section 3.3.3). Two spatial resolutions were tested; the PCO was coupled to a 2:1 and a 1:1 optics giving a pixel size of 11.34 µm and 6.29 µm, respectively. The scintillator used for the scans was a 250 µm LuAG. The sample to detector distance was set to 11 m for the 11 µm optics and reduced to 4.5 m for the 6 µm optics to satisfy the criteria imposed by propagation-based phase contrast imaging coupled to the single distance phase retrieval algorithm (section 2.2.3). Since the paleostage has a fixed position, the detector camera was moved along the beam propagation when switching resolution. After some preliminary tests (not shown), it was decided to use monochromatic radiation at 40 keV, selected with the double Laue monochromator. This energy was the best compromise between the contrast maximization (highest at lower energies), the flux available (higher in the range 30-50 keV for the used monochromator) and the sample transmission (higher at higher energies).

A description of the mechanical ventilator and of the implementation of the retrospective gating can be found in section 3.3.4 and 4.2.3.

5.4.2 11 µm and 6 µm pixel size imaging: animal preparation

Imaging was performed in OFA rats. The surgery and animal handling were the same as those utilized in the pink beam imaging approach (section 5.3.2).

5.4.3 11µm and 6µm pixel size imaging: experimental protocol

The dynamic scans with apneic oxygenation and with mechanical ventilation were described in Section 4.2.1.

As in the case of the pink beam imaging, and despite the lower radiation dose expected with monochromatic radiation, the half tomography acquisition was avoided. In this study, we were not interested in acquiring the whole lung in the horizontal plane, but in maximizing the image quality for a given radiation dose. Once the number of projections, and therefore the dose is fixed, a twofold higher angular sampling is obtained by avoiding half-tomography, acquiring therefore the CT over a 180 ° sample rotation. The camera frame rate was set to 250 fps for the 11 µm pixel size and to 500 fps for the 6 µm pixel size. The integration time per projection was 2 ms, independently from the spatial resolution. The camera was set in rolling shutter mode, with a field of view of 2560 × 201 (Horizontal × Vertical) pixels equal to (29.0 × 2.3) mm^2 at 11 µm and to (16.1×1.3) mm^2 at 6 µm.

Images were acquired under apneic oxygenation at two different pressure levels: 5 cmH_2O and 12 cmH_2O. When triggered by the ECG, the mechanical ventilation was set to an inspiratory time of 350 ms, and an expiratory time varying, according to the heart rate, between 0.5 ms and 0.6 ms. A PEEP of 5 cmH_2O was set, with peak inspiratory pressure of 12 cmH_2O.

5.4.4 11 µm and 6 µm pixel size imaging: preliminary results

These experiments were performed for the first time at the end of this Thesis work and just before the long shutdown of the ESRF accelerator. In this paragraph, only preliminary results will be therefore presented. In Figure 5-6 an example of dynamic CT acquired with the 11 µm optics is shown. Image (a) and (b) represent a reconstruction of the dynamic scan with apneic oxygenation, without and with heart gating respectively. Image (a) was reconstructed from 1000 equally spaced projections; figure (b) was reconstructed after selecting the 1000 projections with the ECG analysis based on the heart phase, as presented in section 4.2.7. We notice an increased visibility in (b) with respect to (a) of the terminal airways especially in the ventral and cardiac lobes, where the cardiogenic motion was strongest. Imaging was successful in the OFA rat model at 11 µm even with the dynamic scan during mechanical ventilation, as shown in Figure 5-6 (c). In this specific case, motion artefacts were not perfectly compensated in the right lung (on the left in the image): the fissure at the border with the cardiac lobe is for example discontinuous, in the point shown by the white arrow.

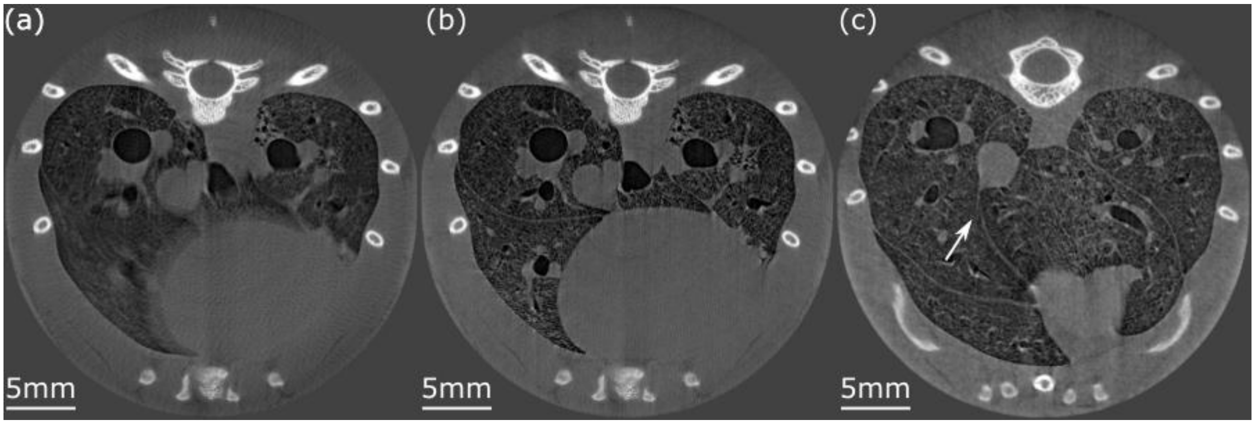

Figure 5-6 Dynamic CT acquired in-vivo in a rat model with an effective pixel size of 11 µm. (a) Dynamic CT acquired in apnea (PEEP 5cmH_2O) and reconstructed without gating. (b) Dynamic CT acquired in apnea (PEEP 5cmH_2O) and reconstructed during the diastolic phase. (c) Dynamic CT acquired during mechanical ventilation and reconstructed at the beginning of inspiration and on the QRS complex; a discontinuity in the lung fissure is visible (white arrow).

Figure 5-7 represent an example of results obtained with the 6 µm optics. As in the previous case, panels (a) and (b) were reconstructed from the dynamic scan with apneic oxygenation, respectively without and with the cardiac gating. Figure 5-7 (b) was reconstructed with a delay of 0 ms from the detected R peak and precedes the systole. The alveolar structure is clearly visible, both in the heart proximity and at towards the thoracic cavity. The largest structures, including the heart, large airways and blood vessels are reconstructed without motion artefacts, which would cause their edges to be discontinuous. Some motion artefacts are visible however in Figure 5-7 (c), relative to the dynamic scan with mechanical ventilation; they occur mainly at the level of the large airways in the lower left part of the image. Despite these motion artefacts, the alveolar structure of the lung parenchyma is still visible, proving the stability of the parenchymal motion during the synchronized cardiac and respiratory motion in a rat model.

5.4.5 11 µm and 6 µm pixel size imaging: discussion

The dynamic 3D microscopy acquisition protocols introduced in this Thesis work, developed in rabbit with a pixel size of 20 µm, were successfully extended to 11 µm and 6 µm pixel size in an adult rat model. We succeeded therefore in acquiring a dynamic CT *in-vivo* with a spatial resolution allowing to visualize the alveolar structure. To our knowledge this is the first time this resolution is achieved *in-vivo*, preserving both the structural and dynamic information.

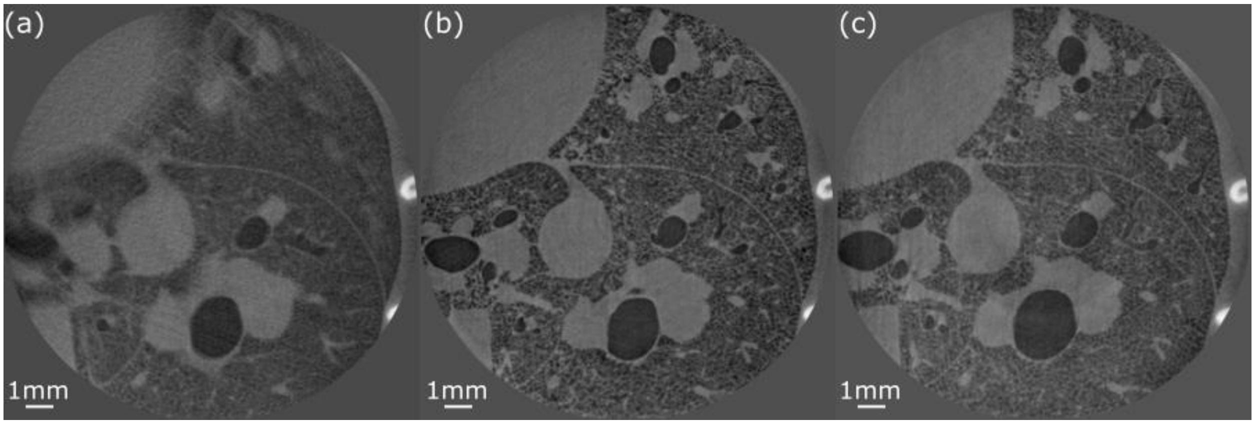

Figure 5-7 Dynamic CT acquired in-vivo with an effective pixel size of 6 µm. (a) Dynamic CT acquired in apnea (PEEP 5cmH_2O) and reconstructed without gating. (b) Dynamic CT acquired in apnea (PEEP 5cmH_2O) and reconstructed with heart gating on the recorder QRS complex. (c) Dynamic CT acquired during mechanical ventilation and reconstructed with heart gating at the beginning of inspiration and on the QRS complex.

In large scale synchrotron facilities, a lower pixel size of 3 µm was achieved *in-vivo* by Lovric et al. at the SLS. Compared to our study, a prospective heart triggering approach was used in a healthy mouse model coupled to a single long respiratory pause. In that study, the diastolic phase at the end of the cardiac cycle was targeted. Since this technique is based on a respiratory pause (constant airway pressure), information on the alveolar kinematics can be retrieved only by quasi-static inflation and deflation, i.e. by successive scans acquired at increasing or decreasing airway pressures. Information on the cardiogenic motion is lost.

As reported in Section 2.4.2, the only other tomographic technique allowing to obtain dynamic information on the lung mechanics *in-vivo* at high resolution (15 µm) was developed by Dubsky et al. at Spring-8 [83]. This approach was based on retrospective cardiac gating and allowed to study the cardiogenic motion of the lung parenchyma and the cardiogenic airflow in a mouse model. Compared to our approach, a synchronization between mechanical ventilation and heart motion was not achieved, therefore the cardiogenic motion was reconstructed only at the end of expiration, when the lung motion due to the mechanical ventilation was minimized. The spatial resolution was moreover lower.

Compared to the existing techniques our acquisition protocols represent therefore an innovative investigative tool pushing the resolution of dynamic *in-vivo* CT down to 6 µm, allowing to describe alveolar structures, as well as preserving dynamic information. Not only the cardiogenic motion can be studied at the alveolar scale, but also the more complex parenchymal deformation caused simultaneously by the cardiac activity and the mechanical ventilator can be assessed.

In a healthy rat model, the dynamic scan with mechanical ventilation will allow for example to study the mechanism through which lung alveoli inflate and deflate. A consensus has not yet been reached on whether the lung increases its volume through alveolar recruitment or through an increase in the size of the alveolar ducts [130], [131]. In order to study this open question, acini need to be segmented and tracked along the respiratory cycle: the feasibility of this analysis is currently under evaluation. Restricting the study to the cardiogenic motion, alveolar deformation and the presence of atelectrauma next to the heart, due to the cardiac activity, could be investigated. Another application of the techniques at this high spatial resolution could be the study of the parenchymal mechanics at the alveolar scale in a rat model of VILI. This analysis could provide information on the alveolar changes occurring in an early stage of VILI and would provide additional insight on the recruitment-derecruitment mechanisms and the critical pressures at which they occur.

One of the prerequisites to the study of the lung mechanics at the alveolar scale is the possibility to segment and track single acini or acinar clusters. The main challenge is related to the low signal to noise ratio generated by under-sampling artefacts, due to the low number of projections, and by the short integration time per projection. Residual motion artefacts, due to non-periodic lung motions may moreover influence the shape and the connectivity of the alveolar septa. Motion artefacts are more likely to affect the dynamic scan with mechanical ventilation, due to the longer acquisition times with respect to apneic oxygenation.

In addition to the low signal to noise ratio, a further limitation of the technique consists in the small field of view in the vertical direction: several alveoli move in and out of the field of view during lung inflation and deflation, hindering alveolar tracking. The limitation in the field of view is due to the maximum data transfer speed to the ESRF servers and is therefore purely technical. Alveolar tracking is moreover currently based on image registration techniques, which may fail at high resolution due to the large displacements relative to the pixel size (Section 2.5.1 and 4.3.3.1).

A further limitation to be taken into account at this spatial resolution is the rolling shutter mode of the camera. This acquisition mode is necessary to acquire frames at the frequency required

(500 fps) but introduces a delay of 1 ms between the outer rows and the central ones. 1 ms is not negligible with respect to the time resolution (4 ms) and may cause distortions when imaging moving samples. The theoretical time resolution of 4 ms, determined as the reciprocal of the acquisition frequency plus the integration time per projection (Section 2.3.1), is however reduced by the uncertainties introduced by the ECG phase selection (see Section 4.2.7.1 for reference) and by the non-perfect periodicity of the heart rate: each heart cycle has in fact a slightly different duration.

Unlike the 6 µm optics, the lower resolution scans presented in this section and acquired using a pixel size of 11 µm, do not provide information at the alveolar level, but have the advantage of a large field of view, allowing to image a complete transversal section of a rat lung in a single scan. This method was developed to progressively reduce the pixel size below the 20 µm value described in Chapter 4. The applications at this resolution are the same as those presented for the 20 µm optics. The main improvements, with respect to Chapter 4, cover not only the spatial resolution, but also the time resolution of the scan, increased by a factor of two thanks to the improvement in the data transfer to the ESRF server, which allowed to acquire at 250 fps.

5.5 CONCLUSIONS

In this Chapter three different approaches to develop a dynamic CT technique capable of resolving the *in-vivo* alveolar motion due to cardiogenic oscillations and breathing were presented. The first approach was based on a prospective heart gating, on successive respiratory pauses and was applied to a rabbit model using a detector pixel size of 3 µm. The second and the third approaches were instead based on a rat model and on the dynamic techniques introduced in Chapter 4. These were different in the spectrum and in the optics utilized: polychromatic radiation and 3 µm pixel size for the first and monochromatic radiation and 11 µm or 6 µm pixel size for the second. If we exclude the acquisition protocol utilizing an 11 µm pixel size, in which the alveolar structure could not be resolved, the one based on a 6 µm pixel size was the only successful approach. There are three main factors that could have determined the success of this acquisition protocol: dose rate, time resolution achievable and animal model. Understanding their individual role and contribution to the image quality will be of fundamental importance when trying to develop a dynamic CT technique at a pixel size lower than 6 µm.

Monochromatic imaging at 6 µm showed the stability of the parenchymal motion in an adult rat model in both the acquisition protocols proposed, based on apneic oxygenation and mechanical ventilation. The instabilities observed on the same animal model and with the same ventilatory strategies with polychromatic radiation (Section 5.3.4), suggest that the pink beam imaging approach may have failed due to the effects of dose, which was modifying the lung structure during the acquisition of the scan. Damages to the collagen, protein determining many of the mechanical properties of the lung tissue, have previously been reported in bones at doses of approximately 35 kGy [132]. This dose was lower than the one delivered during the pink beam imaging. Direct irradiation of the heart in pink beam imaging caused moreover the death of a rat in less than 4 minutes. Pushing forwards the limit of spatial resolution in *in-vivo* scans, will correspond to an increase in the dose delivered to the sample, and in the probability of obtaining artefacts due to radiation damage.

It is still not clear however, if the animal model or the time resolution caused the failure of the first approach, based on monochromatic radiation and prospective triggering (Section 5.2.6) in rabbit. The role of the animal model could be further investigated by applying the 6 µm imaging technique in rabbit.

Further improving the spatial resolution at ID17, with the limitations in monochromatic flux, could be achieved in the current status only by increasing the integration time per projection with respect to the 6 µm optics. This would reduce the time resolution and degrade the image quality. An optimization of the beamline instrumentation would otherwise be required. An optimization of the double Laue monochromator, in order to increase its reflectivity in the energy range of interest (40 keV to 60 keV), could be for example evaluated. On the other hand, an optimization of the indirect conversion X-ray detection system of the beamline should be studied (scintillators, magnifying optics, detector) in order to maximize the detection efficiency of the X-rays transmitted by the sample.

GENERAL CONCLUSIONS

In this work an acquisition protocol for *in-vivo* dynamic phase-contrast 3D microscopy was developed, which was based on the synchronization between the heart and the mechanical ventilation. **Based on our experience this is the only existing 3D microscopy acquisition protocol capable of resolving the combined lung motion due to breathing and heart contraction/expansion with an effective pixel size smaller than 50 µm.**

This protocol was initially implemented using an effective pixel size of 20 µm and was applied to a rabbit model of VILI, allowing to visualize and quantify the atelectrauma. To quantify the opening and closing of the airspaces, volumes corresponding to different time frames along the respiratory cycle had to be realigned using elastic image registration. The optimization of the elastic image registration protocol was the main challenge to be overcome in the data analysis. On one hand, the lung parenchyma displacement to be described was large compared to the pixel size, making the algorithm prone to introduce distortions and folding in the estimated displacement field; on the other hand, the atelectrauma introduced non-corresponding structures in the volume to be realigned.

Following the optimization of the elastic image registration technique, atelectrauma was quantified as a function of time during a tidal breath. Previous studies of the time dependence of recruitment and derecruitment of the airspaces during the respiratory cycle were based on deep inflation maneuvers [53], [127]. **In our approach, atelectrauma was observed and quantified in dynamic conditions and with a physiological respiratory rate, therefore closer to the clinical conditions in ventilated ARDS patients**.

Heterogeneity was identified in the tracheal pressures at which single airways were recruited and derecruited, both within and in between animals. This finding is compatible with the dynamic nature of the atelectrauma, in which recruitment and derecruitment are determined by the distribution of critical opening and closing pressures, by the finite opening and closing speed of terminal airways and acini and by the complex mechanical interactions between neighboring lung units [14]. Drecruitment was moreover found to occur even at relatively high pressures, suggesting that even moderate PEEP (>10 cmH_2O) could not be sufficient to avoid atelectrauma.

The acquisition protocol proposed allowed to evaluate the correlation between atelectrauma and alveolar damage and between atelectrauma and cellular recruitment in the lung tissue in our injury model. **A positive spatial correlation was observed, confirming the hypothetic role of atelectrauma in lung inflammation in an early stage of VILI.** Further evidence based on pro-inflammatory cytokines would be required but could not be obtained during this work due to the difficulties encountered in staining rabbit lung tissues.

The acquisition protocol introduced in this work was further developed utilizing a pixel size of 6 µm in a rat model. **We succeeded therefore in performing for the first time *in-vivo* dynamic 3D microscopy, visualizing the alveolar structure of the lung parenchyma and preserving the dynamic information.** This technique, applied to a healthy lung, could allow to visualize *in-vivo* the alveolar deformation induced by cardiac contractions and mechanical ventilation.

Three challenges had to be overcome to increase the spatial resolution to 6 µm: (i) the stability of the lung parenchymal motion, connected to the ventilation strategy used and to the animal model; (ii) the high time resolution required, which determines high acquisition- and therefore high data-transfer rates; (iii) the high radiation dose delivered to the sample, which could cause immediate tissue damage and deformation during the acquisition.

The methods developed in the course of this Thesis and their applications could be further explored and developed, utilizing both the effective pixel sizes: 20 µm and 6 µm.

The possibility offered by our experimental protocol, associated to an effective pixel size of 20 µm, to spatially correlate the biological damage to atelectrauma, will allow further characterization of the injury to the lung tissue matrix. On one hand, additional trials on immunohistochemistry are currently being performed to obtain a successful staining of the pro-inflammatory cytokines. The optimization of the histological tissue staining with antibodies anti IL-8 and RAGE, which have been unsuccessful so far, is still ongoing in collaboration with the pathologist from the Grenoble University Hospital. On the other hand, the feasibility of studying the alteration of the collagen microstructure and matrix induced in our injury model by the mechanical ventilation is presently under evaluation. For this purpose, the possibility to visualize collagen and procollagen with Fourier Transform Infrared Spectroscopy is under study, in an ad-hoc established collaboration with Ganesh Sockalingum from the University of Reims

The acquisition protocol at the highest spatial resolution would instead allow a direct visualization of the mechanisms governing lung inflation and deflation at the alveolar scale, which is nowadays still missing. It would have an important impact in the field of lung physiology with possible applications to the mathematical modelling of lung mechanics and fluid dynamics. Extending the image registration protocol developed in this Thesis for the 20 µm pixel size scan, in order to study the deformation of the lung parenchyma with a 6 µm pixel size, is a task carried out within our group.

The study of a rat model of VILI at the alveolar scale could be a future application of the acquisition protocol utilizing the 6 µm pixel size optics. This study could provide the missing insight on the alveolar changes occurring in an early stage of the injury. The instability of the injured lung will represent the main challenge to be overcome during the image acquisition.

Additional developments are however necessary to further increase the spatial resolution of our acquisition protocol, to better visualize the alveoli and the alveolar walls reaching the 3 µm pixel size achieved so far *in-vivo* only in static conditions [13]. The main challenges in achieving this important result are the inhomogeneous nature of the lung parenchymal motion and the realization of a protocol reducing the deposited radiation dose, in order to avoid immediate radiation damage.

REFERENCES

[1] D. Ashbaugh, D. Boyd Bigelow, T. Petty, and B. Levine, “Acute Respiratory Distress In Adults,” *Lancet*, vol. 290, no. 7511, pp. 319–323, 1967.

[2] V. M. Ranieri *et al.*, “Acute respiratory distress syndrome: The Berlin definition,” *JAMA - J. Am. Med. Assoc.*, 2012.

[3] G. Bellani *et al.*, “Epidemiology, patterns of care, and mortality for patients with acute respiratory distress syndrome in intensive care units in 50 countries,” *JAMA - J. Am. Med. Assoc.*, 2016.

[4] G. Bellani, J. G. Laffey, T. Pham, and E. Fan, “The LUNG SAFE study: A presentation of the prevalence of ARDS according to the Berlin Definition!,” *Critical Care*. 2016.

[5] A. S. Slutsky and V. M. Ranieri, “Ventilator-Induced Lung Injury,” *N. Engl. J. Med.*, vol. 369, no. 22, pp. 2126–2136, Nov. 2013.

[6] J. H. T. Bates and B. J. Smith, “Ventilator-induced lung injury and lung mechanics,” *Ann. Transl. Med. Publ. Ahead Print*, 2018.

[7] Acute Respiratory Distress Syndrome Network *et al.*, “Ventilation with lower tidal volumes as compared with traditional tidal volumes for acute lung injury and the acute respiratory distress syndrome.,” *N. Engl. J. Med.*, 2000.

[8] S. S. Kay, A. M. Bilek, K. C. Dee, and D. P. Gaver, “Pressure gradient, not exposure duration, determines the extent of epithelial cell damage in a model of pulmonary airway reopening,” *J. Appl. Physiol.*, 2004.

[9] H. L. Dailey, L. M. Ricles, H. C. Yalcin, and S. N. Ghadiali, “Image-based finite element modeling of alveolar epithelial cell injury during airway reopening,” *J. Appl. Physiol.*, 2008.

[10] S. Dubsky, S. B. Hooper, K. K. W. Siu, and A. Fouras, “Synchrotron-based dynamic computed tomography of tissue motion for regional lung function measurement,” *J. R.*

Soc. Interface, vol. 9, no. 74, pp. 2213–2224, Sep. 2012.

[11] G. Lovric *et al.*, “Spatial distribution of ventilator induced lung injury at the μm-scale. An in-vivo synchrotron phase-contrast microscopy study in BALB/c mice,” *Am. J. Respir. Crit. Care Med.,* 2018.

[12] M. R. Pinsky, “Recent advances in the clinical application of heart-lung interactions,” *Current Opinion in Critical Care*. 2002.

[13] G. Lovric *et al.*, “Tomographic in vivo microscopy for the study of lung physiology at the alveolar level,” *Sci. Rep.*, 2017.

[14] L. Broche *et al.*, “Dynamic Mechanical Interactions between Neighboring Airspaces Determine Cyclic Opening and Closure in Injured Lung,” *Crit. Care Med.,* 2017.

[15] E. R. Weibel, *The pathway for oxygen: structure and function in the mammalian respiratory system*. 1984.

[16] K. Horsfield, “Diameters, generations, and orders of branches in the bronchial tree,” *J. Appl. Physiol.*, 2017.

[17] H. Kitaoka, R. Takaki, and B. Suki, “A three-dimensional model of the human airway tree,” *J. Appl. Physiol.*, 2017.

[18] Q. Hamid, J. Shannon, and J. Martin, “Histology and gross anatomy of the respiratory tract,” in *Physiologic Basis of Respiratory,* 2005.

[19] M. Rodriguez, S. Bur, A. Favre, and E. R. Weibel, “Pulmonary acinus: Geometry and morphometry of the peripheral airway system in rat and rabbit,” *Am. J. Anat.,* 1987.

[20] J. B. West and A. M. Luke, *West’s Respiratory Physiology - The Essentials*. 2016.

[21] M. Ochs *et al.*, “The Number of Alveoli in the Human Lung,” *Am. J. Respir. Crit. Care Med.,* 2004.

[22] P. S. Hasleton, “The internal surface area of the adult human lung.,” *J. Anat.,* 1972.

[23] E. R. Weibel, “What makes a good lung?,” *Swiss Med. Wkly.*, 2009.

[24] E. R. Weibel, “Fractal geometry: a design principle for living organisms.,” *Am. J.*

Physiol., 1991.

[25] D. M. Hyde *et al.*, “Asthma: A comparison of animal models using stereological methods,” *European Respiratory Review*. 2006.

[26] J. G. Laffey and B. P. Kavanagh, “Insight into acute respiratory distress syndrome: From models to patients,” *American Journal of Respiratory and Critical Care Medicine*. 2017.

[27] S. H. Loring, G. P. Topulos, and R. D. Hubmayr, “Transpulmonary pressure: The importance of precise definitions and limiting assumptions,” *American Journal of Respiratory and Critical Care Medicine*. 2016.

[28] F. Rohrer, “Der Zusammenhang der Atemkräfte und ihre Abhängigkeit vom Dehnungszustand der Atmungsorgane,” *Pflüger’s Arch. für die Gesamte Physiol. des Menschen und der Tiere,* 1916.

[29] J. Mead, “Mechanical Properties of Lungs,” *Physiol. Rev.,* 2017.

[30] W. R. Henderson, L. Chen, M. B. P. Amato, and L. J. Brochard, “Fifty years of research in ARDS: Respiratory mechanics in acute respiratory distress syndrome,” *American Journal of Respiratory and Critical Care Medicine*. 2017.

[31] H. Blasius, “Grenzschichten in Flussigkeiten mit kleiner Reibung,” *Z. Angew. Math. Phys.* 1908.

[32] B. Suki, D. Stamenović, and R. Hubmayr, “Lung parenchymal mechanics,” *Compr. Physiol.,* 2011.

[33] A. Fick, “Ueber Diffusion,” *Ann. Phys.,* 1855.

[34] J. Villar and A. S. Slutsky, “The incidence of the adult respiratory distress syndrome.,” *Am. Rev. Respir. Dis.*, 1989.

[35] G. D. Rubenfeld *et al.*, “Incidence and Outcomes of Acute Lung Injury,” *N. Engl. J. Med.,* vol. 353, no. 16, pp. 1685–1693, Oct. 2005.

[36] A. P. Wheeler and G. R. Bernard, “Acute lung injury and the acute respiratory distress syndrome: a clinical review,” *Lancet,* vol. 369, no. 9572, pp. 1553–1564, 2007.

[37] T. Pham and G. D. Rubenfeld, “Fifty years of research in ards the epidemiology of acute respiratory distress syndrome a 50th birthday review,” *American Journal of Respiratory and Critical Care Medicine*. 2017.

[38] L. Gattinoni, J. J. Marini, A. Pesenti, M. Quintel, J. Mancebo, and L. Brochard, “The ‘baby lung’ became an adult,” *Intensive Care Medicine*. 2016.

[39] A. Vieillard-Baron *et al.*, “Acute cor pulmonale in acute respiratory distress syndrome submitted to protective ventilation: Incidence, clinical implications, and prognosis,” *Crit. Care Med.*, 2001.

[40] S. Tsuchida *et al.*, “Atelectasis causes alveolar injury in nonatelectatic lung regions,” *Am. J. Respir. Crit. Care Med.*, 2006.

[41] D. Dreyfuss, P. Soler, G. Basset, and G. Saumon, “High Inflation Pressure Pulmonary Edema: Respective Effects of High Airway Pressure, High Tidal Volume, and Positive End-expiratory Pressure,” *Am. Rev. Respir. Dis.*, vol. 137, no. 5, pp. 1159–1164, May 1988.

[42] “Higher versus Lower Positive End-Expiratory Pressures in Patients with the Acute Respiratory Distress Syndrome,” *N. Engl. J. Med.*, vol. 351, no. 4, pp. 327–336, Jul. 2004.

[43] M. O. Meade *et al.*, “Ventilation Strategy Using Low Tidal Volumes, Recruitment Maneuvers, and High Positive End-Expiratory Pressure for Acute Lung Injury and Acute Respiratory Distress Syndrome: A Randomized Controlled Trial,” *JAMA*, vol. 299, no. 6, pp. 637–645, Feb. 2008.

[44] A. Mercat *et al.*, “Positive End-Expiratory Pressure Setting in Adults With Acute Lung Injury and Acute Respiratory Distress Syndrome: A Randomized Controlled Trial,” *JAMA*, vol. 299, no. 6, pp. 646–655, Feb. 2008.

[45] M. Briel *et al.*, “Higher vs Lower Positive End-Expiratory Pressure in Patients With Acute Lung Injury and Acute Respiratory Distress Syndrome: Systematic Review and Meta-analysis,” *JAMA*, vol. 303, no. 9, pp. 865–873, Mar. 2010.

[46] W. G. for the A. R. for A. R. D. S. T. (ART) Investigators *et al.*, “Effect of Lung Recruitment and Titrated Positive End-Expiratory Pressure (PEEP) vs Low PEEP on

Mortality in Patients With Acute Respiratory Distress Syndrome: A Randomized Clinical Trial," *JAMA*, vol. 318, no. 14, pp. 1335–1345, Oct. 2017.

[47] J. Mead, T. Takishima, and D. Leith, "Stress distribution in lungs: a model of pulmonary elasticity.," *J. Appl. Physiol.*, 1970.

[48] T. Uchida *et al.*, "Receptor for advanced glycation end-products is a marker of type I cell injury in acute lung injury," *Am. J. Respir. Crit. Care Med.*, 2006.

[49] C. Guérin *et al.*, "Prone Positioning in Severe Acute Respiratory Distress Syndrome," *N. Engl. J. Med.*, vol. 368, no. 23, pp. 2159–2168, May 2013.

[50] A. B. DUBOIS, A. W. BRODY, D. H. LEWIS, and B. F. BURGESS, "Oscillation mechanics of lungs and chest in man," *J. Appl. Physiol.*, 1956.

[51] E. Oostveen *et al.*, "The forced oscillation technique in clinical practice: Methodology, recommendations and future developments," *European Respiratory Journal*. 2003.

[52] L. Gattinoni, A. Pesenti, L. Avalli, F. Rossi, and M. Bombino, "Pressure-volume curve of total respiratory system in acute respiratory failure. Computed tomographic scan study," *Am. Rev. Respir. Dis.*, 1987.

[53] B. J. Smith, K. A. Grant, and J. H. T. Bates, "Linking the development of ventilator-induced injury to mechanical function in the lung," *Ann. Biomed. Eng.*, 2013.

[54] B. Suki, A. L. Barabási, Z. Hantos, F. Peták, and H. E. Stanley, "Avalanches and power-law behaviour in lung inflation," *Nature*, 1994.

[55] L. Pavone, S. Albert, J. DiRocco, L. Gatto, and G. Nieman, "Alveolar instability caused by mechanical ventilation initially damages the nondependent normal lung," *Crit. Care*, 2007.

[56] G. Bellani, M. Amigoni, and A. Pesent, "Positron emission tomography in ARDS: A new look at an old syndrome," *Minerva Anestesiologica*. 2011.

[57] W. W. Moses, "Fundamental limits of spatial resolution in PET," *Nucl. Instruments Methods Phys. Res. Sect. A Accel. Spectrometers, Detect. Assoc. Equip.*, 2011.

[58] A. Bravin, P. Coan, and P. Suortti, "X-ray phase-contrast imaging: from pre-clinical

applications towards clinics.," *Phys. Med. Biol.*, vol. 58, no. 1, pp. R1-35, 2013.

[59] Kak and Slaney, *Principles of Computerized Tomographic Imaging*. 1988.

[60] D. Paganin, *Coherent X-Ray Optics*. 2007.

[61] L. V. Azaroff, *Elements of X-Ray Crystallography*. McGraw-Hill, 1968.

[62] J. C. Gore and S. Leeman, "The reconstruction of objects from incomplete projections," *Phys. Med. Biol.*, 1980.

[63] J. D. Jackson, *Jackson - Classical Electrodynamics*. 1962.

[64] A. Snigirev, I. Snigireva, V. Kohn, S. Kuznetsov, and I. Schelokov, "On the possibilities of x-ray phase contrast microimaging by coherent high-energy synchrotron radiation," *Rev. Sci. Instrum.*, 1995.

[65] J. Keyriläinen, A. Bravin, M. Fernndez, M. Tenhunen, P. Virkkunen, and P. Suortti, "Phase-contrast X-ray imaging of breast," *Acta Radiologica*. 2010.

[66] M. Born and E. Wolf, *Principles of Optics 7th edition*. 1999.

[67] M. R. Teague, "DETERMINISTIC PHASE RETRIEVAL: A GREEN'S FUNCTION SOLUTION.," *J. Opt. Soc. Am.*, 1983.

[68] A. Burvall, U. Lundström, P. A. C. Takman, D. H. Larsson, and H. M. Hertz, "Phase retrieval in X-ray phase-contrast imaging suitable for tomography," *Opt. Express*, 2011.

[69] D. Paganin, S. C. Mayo, T. E. Gureyev, P. R. Miller, and S. W. Wilkins, "Simultaneous phase and amplitude extraction from a single defocused image of a homogeneous object," *J. Microsc.*, vol. 206, no. 1, pp. 33–40, Apr. 2002.

[70] G. Lovric, R. Mokso, C. M. Schlepütz, and M. Stampanoni, "A multi-purpose imaging endstation for high-resolution micrometer-scaled sub-second tomography," *Phys. Medica*, 2016.

[71] R. Boistel, N. Pollet, J. Y. Tinevez, P. Cloetens, and M. Schlenker, "Irradiation damage to frog inner ear during synchrotron radiation tomographic investigation," *J. Electron Spectros. Relat. Phenomena*, 2009.

[72] S. Halliburton *et al.*, “State-of-the-art in CT hardware and scan modes for cardiovascular CT,” *Journal of Cardiovascular Computed Tomography*. 2012.

[73] N. L. Ford *et al.*, “Prospective respiratory-gated micro-CT of free breathing rodents,” *Med. Phys.*, 2005.

[74] N. L. Ford, A. R. Wheatley, D. W. Holdsworth, and M. Drangova, “Optimization of a retrospective technique for respiratory-gated high speed micro-CT of free-breathing rodents.,” *Phys. Med. Biol.*, vol. 52, no. 19, pp. 5749–5769, 2007.

[75] M. Preissner *et al.*, “High resolution propagation-based imaging system for in vivo dynamic computed tomography of lungs in small animals,” *Phys. Med. Biol.*, 2018.

[76] M. J. Kitchen, D. Paganin, R. a Lewis, N. Yagi, K. Uesugi, and S. T. Mudie, “On the origin of speckle in x-ray phase contrast images of lung tissue.,” *Phys. Med. Biol.*, vol. 49, no. 18, pp. 4335–4348, 2004.

[77] M. Saccomano *et al.*, “Synchrotron inline phase contrast µCT enables detailed virtual histology of embedded soft-tissue samples with and without staining,” *J. Synchrotron Radiat.*, 2018.

[78] J. Albers, M. A. Markus, F. Alves, and C. Dullin, “X-ray based virtual histology allows guided sectioning of heavy ion stained murine lungs for histological analysis,” *Sci. Rep.*, 2018.

[79] S. Bayat *et al.*, “Quantitative functional lung imaging with synchroton radiation using inhaled xenon as contrast agent,” *Phys. Med. Biol.*, 2001.

[80] M. J. Kitchen *et al.*, “Dynamic measures of regional lung air volume using phase contrast x-ray imaging,” *Phys. Med. Biol.*, 2008.

[81] M. J. Kitchen *et al.*, “CT dose reduction factors in the thousands using X-ray phase contrast,” *Sci. Rep.*, 2017.

[82] T. Sera *et al.*, “Development of high-resolution 4D in vivo-CT for visualization of cardiac and respiratory deformations of small animals.,” *Phys. Med. Biol.*, vol. 53, no. 16, pp. 4285–4301, 2008.

[83] S. Dubsky, J. Thurgood, A. Fouras, B. R. Thompson, and G. J. Sheard, “Cardiogenic Airflow in the Lung Revealed Using Synchrotron-Based Dynamic Lung Imaging,” *Sci. Rep.*, vol. 8, no. 1, p. 4930, 2018.

[84] G. E. Christensen, J. H. Song, W. Lu, I. El Naqa, and D. A. Low, “Tracking lung tissue motion and expansion/compression with inverse consistent image registration and spirometry,” *Med. Phys.*, vol. 34, no. 6Part1, pp. 2155–2163, Jun. 2007.

[85] J. M. Reinhardt, K. Ding, K. Cao, G. E. Christensen, E. A. Hoffman, and S. V. Bodas, “Registration-based estimates of local lung tissue expansion compared to xenon CT measures of specific ventilation,” *Med. Image Anal.*, 2008.

[86] M. Holden, “A review of geometric transformations for nonrigid body registration,” *IEEE Trans. Med. Imaging*, 2008.

[87] A. Sotiras, C. Davatzikos, and N. Paragios, “Deformable medical image registration: A survey,” *IEEE Trans. Med. Imaging*, 2013.

[88] S. P. Timoshenko and J. N. Goodier, *Theory of Elasticity*. McGraw-Hill, 1970.

[89] L. D. Landau and E. M. Lifshitz, *Fluid mechanics: Course of theoretical physics*. 1987.

[90] D. Rueckert, “Nonrigid registration using free-form deformations: Application to breast mr images,” *IEEE Trans. Med. Imaging*, 1999.

[91] J. Kybic and M. Unser, “Fast parametric elastic image registration,” *IEEE Trans. Image Process.*, 2003.

[92] J. P. W. Pluim, J. B. A. A. Maintz, and M. A. Viergever, “Mutual-information-based registration of medical images: A survey,” *IEEE Transactions on Medical Imaging*. 2003.

[93] M. A. Cauchy, “Méthode générale pour la résolution des systèmes d’équations simultanées,” 1847.

[94] M. R. Hestenes and E. Stiefel, “Methods of conjugate gradients for solving linear systems,” *J. Res. Natl. Bur. Stand. (1934).*, 1952.

[95] D. C. Liu and J. Nocedal, “On the limited memory BFGS method for large scale optimization,” *Math. Program.*, 1989.

[96] Y. Yin, E. A. Hoffman, and C. L. Lin, “Mass preserving nonrigid registration of CT lung images using cubic B-spline,” *Med. Phys.*, 2009.

[97] B. Zhao *et al.*, “Tissue-Volume Preserving Deformable Image Registration for 4DCT Pulmonary Images,” *2016 IEEE Conference on Computer Vision and Pattern Recognition Workshops (CVPRW)*. pp. 481–489, 2016.

[98] J. Kybic, P. Thévenaz, A. Nirkko, and M. Unser, “Unwarping of unidirectionally distorted EPI images,” *IEEE Trans. Med. Imaging,* 2000.

[99] F. R. Elder, A. M. Gurewitsch, R. V. Langmuir, and H. C. Pollock, “Radiation from electrons in a synchrotron [8],” *Physical Review*. 1947.

[100] E. Bräuer-Krisch *et al.*, “New irradiation geometry for microbeam radiation therapy,” *Phys. Med. Biol.,* 2005.

[101] G. E. Barbone *et al.*, “Micro-imaging of Brain Cancer Radiation Therapy Using Phase-contrast Computed Tomography,” *Int. J. Radiat. Oncol. Biol. Phys.,* 2018.

[102] L. Porra *et al.*, “Synchrotron imaging shows effect of ventilator settings on intra breath cyclic changes in pulmonary blood volume,” *Am. J. Respir. Cell Mol. Biol.,* 2017.

[103] A. Horng *et al.*, “Cartilage and Soft Tissue Imaging Using X-rays,” *Invest. Radiol.,* 2014.

[104] H. Elleaume *et al.*, “Instrumentation of the ESRF medical imaging facility,” *Nucl. Instruments Methods Phys. Res. Sect. A Accel. Spectrometers, Detect. Assoc. Equip.*, vol. 428, no. 2, pp. 513–527, 1999.

[105] P. Coan, “Development and application of the analyzer-based imaging technique with hard synchrotron radiation,” 2006.

[106] A. Mittone *et al.*, “Multiscale pink beam microCT imaging at the ESRF-ID17 biomedical beamline.”

[107] H. Requardt, M. Renier, T. Brochard, E. Bräuer-Krisch, A. Bravin, and P. Suortti, “A new gas attenuator system for the ID17 biomedical beamline at the ESRF,” *J. Phys. Conf. Ser.*, vol. 425, no. 2, p. 22002, 2013.

[108] I. Martínez-Rovira, J. Sempau, and Y. Prezado, “Development and commissioning of a

Monte Carlo photon beam model for the forthcoming clinical trials in microbeam radiation therapy,” *Med. Phys.*, 2012.

[109] A. Mittone, I. Manakov, L. Broche, C. Jarnias, P. Coan, and A. Bravin, “Characterization of a sCMOS-based high-resolution imaging system,” *J. Synchrotron Radiat.*, 2017.

[110] P. Suortti and C. Schulze, “Fixed-exit monochromators for high-energy synchrotron radiation.,” *J. Synchrotron Radiat.*, vol. 2, pp. 6–12, 1995.

[111] P. Suortti *et al.*, “Fixed-exit monochromator for computed tomography with synchrotron radiation at energies 18-90 keV,” *J. Synchrotron Radiat.*, 2000.

[112] M. Renier, P. Bernard, W. Van de Vijver, K. Smets, and P. Tafforeau, “A Large Size Sample Stage for High Resolution 2-D and 3-D X-ray Imaging,” in *11th International Conference on Synchrotron Radiation Instrumentation (SRI)*, 2012.

[113] L. Porra *et al.*, “Effect of tidal volume on distribution of ventilation assessed by synchrotron radiation CT in rabbit,” *J. Appl. Physiol.*, 2004.

[114] Y. Prezado *et al.*, “Dosimetry protocol for the forthcoming clinical trials in synchrotron stereotactic radiation therapy (SSRT),” *Med. Phys.*, 2011.

[115] “R wave detection in the ECG.” [Online]. Available: https://fr.mathworks.com/help/wavelet/ug/r-wave-detection-in-the-ecg.html.

[116] A. Mirone, E. Brun, E. Gouillart, P. Tafforeau, and J. Kieffer, “The PyHST2 hybrid distributed code for high speed tomographic reconstruction with iterative reconstruction and a priori knowledge capabilities,” *Nucl. Instruments Methods Phys. Res. Sect. B Beam Interact. with Mater. Atoms*, 2014.

[117] S. Klein, M. Staring, K. Murphy, M. A. Viergever, and J. P. W. Pluim, “Elastix: A Toolbox for Intensity-Based Medical Image Registration,” *IEEE Trans. Med. Imaging*, vol. 29, no. 1, pp. 196–205, 2010.

[118] K. Marstal, F. Berendsen, M. Staring, and S. Klein, “SimpleElastix: A User-Friendly, Multi-lingual Library for Medical Image Registration,” in *IEEE Computer Society Conference on Computer Vision and Pattern Recognition Workshops*, 2016.

[119] P. Perona and J. Malik, “Scale-Space and Edge Detection Using Anisotropic Diffusion,” *IEEE Trans. Pattern Anal. Mach. Intell.*, 1990.

[120] S. Van Der Walt *et al.*, “Scikit-image: Image processing in python,” *PeerJ*, 2014.

[121] R. A. Fisher, *Statistical Method For Research Workers*, 14th ed. Oliver and Boyd, 1970.

[122] F. Wilcoxon, “Individual Comparisons by Ranking Methods,” *Biometrics Bull.*, 1945.

[123] A. Kraskov, H. Stögbauer, and P. Grassberger, “Estimating mutual information,” *Phys. Rev. E - Stat. Physics, Plasmas, Fluids, Relat. Interdiscip. Top.*, 2004.

[124] R. Mokso *et al.*, “GigaFRoST: The gigabit fast readout system for tomography,” *J. Synchrotron Radiat.*, 2017.

[125] T. Gallot, S. Catheline, P. Roux, J. Brum, N. Benech, and C. Negreira, “Passive elastography: Shear-wave tomography from physiological-noise correlation in soft tissues,” *IEEE Trans. Ultrason. Ferroelectr. Freq. Control*, 2011.

[126] A. A. Kolettas *et al.*, “Influence of apneic oxygenation on cardiorespiratory system homeostasis,” *J. Anesth.*, 2014.

[127] J. H. T. Bates and C. G. Irvin, “Time dependence of recruitment and derecruitment in the lung: a theoretical model,” *J. Appl. Physiol.*, 2002.

[128] V. M. Ranieri *et al.*, “Pressure-time curve predicts minimally injurious ventilatory strategy in an isolated rat lung model,” *Anesthesiology*, 2000.

[129] L. Broche *et al.*, “Individual Airway Closure Characterized In Vivo by Phase-Contrast CT Imaging in Injured Rabbit Lung,” *Crit. Care Med.*, 2019.

[130] D. E. Carney *et al.*, “The mechanism of lung volume change during mechanical ventilation,” *Am. J. Respir. Crit. Care Med.*, 1999.

[131] H. Kitaoka, G. F. Nieman, Y. Fujino, D. Carney, J. DiRocco, and I. Kawase, “A 4-dimensional model of the alveolar structure,” *J. Physiol. Sci.*, 2007.

[132] H. D. Barth, E. A. Zimmermann, E. Schaible, S. Y. Tang, T. Alliston, and R. O. Ritchie, “Characterization of the effects of x-ray irradiation on the hierarchical structure and

mechanical properties of human cortical bone," *Biomaterials*, 2011.